Università degli Studi di Pavia
Università della Svizzera Italiana

Mathematical modeling of Human Induced Pluripotent Stem Cell-Derived Cardiomyocytes (hiPSC-CMs): from ionic currents to 3D ventricle models

Ph.D. Thesis

Ph.D.Candidate:
Sofia Botti

Supervisor:
Ch.mo Prof. Luca F. Pavarino

Academic Year 2021/2022

«The heart has its reasons
which reason knows nothing of»

Blaise Pascal

Acknowledgments

The following pages, as with the past three years of my Ph.D. training, are the result of a great crossroads of ideas, collaborations, and meetings. I would like to thank everybody who supported and helped me and to take this opportunity to express my deepest appreciation to them.

First and foremost, I would like to acknowledge my advisor and mentor, Prof. Luca Pavarino. I am truly indebted to him for his scientific expertise, patient guidance and paternal support which have played a fundamental role in my academic growth.

I would also like to thank Prof. Rolf Krause for his tireless enthusiasm: his confidence in sharing knowledge gave birth to a precious collaboration between the University of Pavia and the Università della Svizzera Italiana (USI).

I wish to extend my appreciation to Prof. Stefano Severi and the members of his research group, in particular to Dr. Chiara Bartolucci, without whose help this work would not have been possible.

My special thanks go to Prof. Lucio Barile and Dr. Claudia Altomare for their precious experimental contributions to my projects, for welcoming me in Bellinzona, and for opening their laboratory to my research and curiosity.

I am especially grateful also to Dr. Michelangelo Paci, for his scientific support and helpful suggestions.

I would like to acknowledge Ing. Michele Torre, who shared with me doubts and strategies in approaching research. My deepest gratitude to Prof. Alessandro Reali and Dr. Francesco Pasqualini for their experience, friendly put at our service.

Last but not least, I thank my mother for the unconditional support and the strength of her love and my father for the silent life hidden in a beating heart.

6

Contents

Introduction

Mathematical and numerical modeling in computational electrocardiology are specific research areas developed in the last few decades in order to support experimental physiology. Mathematical models at both cellular and tissue levels provide essential tools aimed at increasing knowledge of electrical and biological phenomena occurring inside cells, through cellular membranes and in cell aggregates. Furthermore, a dynamic approach to biological phenomena could offer evolutionary models with predictive value in many different situations, corresponding to specific reactions or collateral effects of therapies.

A large part of the research field of this Ph.D. thesis concerns mathematical modeling applied to cardiac electrophysiology analysis at a single cell level. This is possible thanks to the development of mathematical descriptions of single cellular components, ionic channels, pumps, exchangers and subcellular compartments. Each of these aspects converges in the mathematical ionic model, that describes the effect of the ionic currents onto the single cell or heart tissue model. **Chapter 1** contains the basic concepts about cardiomyocyte electrophysiology and action potential modelling.
Electrophysiological models of the heart have become very accurate in recent years giving rise to different libraries, that we supported implementing some widely used ionic models.

In the last few years, research in this mathematical field has reached the modeling of human induced stem cells (hiPSCs), briefly described in **Chapter 2**. This field was pioneered by S. Yamanaka, who was awarded the Nobel Prize in 2012 for the discovery of mature cells reprogrammed to become pluripotent. Many studies have been carried out to identify the most advantageous strategies to drive the differentiation towards the desired cell phenotype, thus allowing valuable investigations in basic research and suggesting useful perspectives for regenerative purposes. Differentiation protocols towards the cardiac lineage allow to generate hiPSC-derived Cardiomyocytes (hiPSC-CMs): spontaneous beating cardiomyocytes, expressing the major caridac markers and ion channels and exhibiting the expected responses to cardiac stimuli. In the cardiovascular field, hiPSCs provide a powerful tool to develop reliable *in-vitro* models for drug toxicity screening, even though such cells are molecularly and functionally immature.

hiPSC-CMs show some relevant differences concerning adult myocytes, requiring a new mathematical approach. To fill this gap, some specific computational ionic models have been developed in the last decade, of which an overview is provided in **Chapter 3**. Three different

pedigrees are compared. The forerunner was Michelangelo Paci, who developed a primal model in 2013, creating a new line that improved in 2018 and 2020. Some other models have been published in the last few years by Koivumäki in 2018, and Kernik in 2019.

Furthermore, hiPSC-CMs arise from differentiation protocols, that result in heterogeneous populations of immature CMs consisting predominantly of ventricular-like cells with a small percentage of atrial-like cells and nodal cells. In **Chapter 4** we focused on the innovative approach to push hiPSC-CMs towards more adult cardiac phenotypes: the dynamic clamp technique. Employing this electronic maturation, the chamber-specific action potential phenotype is more pronounced.
Specifically, this thesis is devoted to investigating the dynamic clamp technique in a fully computational set, suggesting that a suitable choice of the injected current can unveil the stem cardiomyocyte phenotype.

A challenging topic in disease understanding and testing is atrial fibrillation modeling. Human induced pluripotent stem cells may offer a platform to develop new strategies and evaluate drugs, but cultures enriched in atrial-like CMs are needed. The only existing atrial-like model was published in 2013 but did not consider any atrial specific current. Furthermore EOC (Ente Ospedaliero Cantonale) focused on cell differentiating and new data and insights are available; thus, we started developing a new computational model for atrial-like hiPSC-CMs, as presented in **Chapter 5**. Firstly we assessed some parameters based on known scaling existing in the literature. Then, we introduced in the existing ventricular-like Paci2020 computational model the *Ultrarapid Delayed Rectifier Current*, the *Small Conductance Calcium Activated Potassium Channel*, and an atrial formulation of the *Inward Rectifier Potassium Current*. A first manual tuning gave a result a baseline, in which different action potential features taken into account already fitted the experimental data.

Finally, in **Chapter 6** we approached the action potential wave propagation on an engineered ventricle, this one being a three-dimensional heart chamber built through pull-spinning fibers of hiPSC-CMs on a rotating ellipsoidal collector. To deal with this problem, we wrote the monodomain equation on a scaffold geometry, dealing with Isogeometric Analysis for the spatial discretization and the geometrical modeling of the scaffold. The conduction velocity was then calibrated in order to reach the experimental speed of the Calcium signal propagation, while the polynomial degree of the isogeometric bases function was set equal to 2 in order to increase the accuracy of the diffusion term on a slab geometry. In this framework, a final simulation of the whole geometry was carried out.

To sum up, we can summarize the main contributions in the following lines. First of all, we implemented two ionic models for adult ventricular cells, namely the first generation model of Hodgkin-Huxley and the second generation model of O'Hara-Rudy. Such models were implemented in a C++ code and embedded in the $Life^X$ library.
As a second contribution we presented the virtual dynamic clamp with the aim of gaining clearer insights into the phenotype detection when considering human induced pluripotent stem cells-derived cardiomyocytes. Our result can assert that dynamic clamp is a promising approach

as it allows to unveil the chamber phenotype when considering a suitable injected I_{K1} current. A further contribution, a novel atrial specific computational model for atrial-like hiPSC-CMs was also developed, in order to fill the gap and perform the behaviour of some specific currents, such as the *Ultrarapid Delayed Rectifier Current* and the *Small Conductance Calcium Activated Potassium Channel.*

Finally, we described a new tool to model an engineered ventricle. A innovative framework was created to this aim, integrating the well-established Monodomain formulation with the innovative isogeometric approach for the spatial discretization and mesh generation.

Chapter 1

Modeling a cardiac cell

1.1 Elements of Cardiac Physiology

The heart is one of the most important organs in the human body. It is the ever-beating muscle in the chest and is literary life-giving, as it is responsible for blood pumping through the vessels by repeated, rhythmic contractions. Its internal organization is build up as a four-chambered pump (see Figure 1.1), located in the thoracic cavity between lungs, divided into two pumps one after the other. The right cardiac cavity pumps blood through the lungs and then back to the heart, while the left cardiac cavity pumps the oxygenated blood through all the body. Electrical activity of the heart is responsible of both mechanical and haemodynamical functions.
The two upper chambers are called atria and they are small cavities with thin walls, while the lower ones are called ventricles and they are larger and much stronger than atria, due to a different muscular organization. Heart can also be divided in right and left heart. The right half of the heart is related to lungs as the right ventricle is connected to the pulmonary artery via the pulmonary valve. Instead, the left heart is related to the whole body and the left ventricle is connected to the aorta through the aortic valve. A specific wall, called septum, separates every part of the heart from another one. The interventricular septum is the thick wall separating the ventricles, while the interatrial septum is between the two upper chambers. Atria and ventricles are separated from each other by the atrioventricular septum. It is convenient to describe the linear flow of the blood through the right side of the heart and then through the left side, but it is very important to realize that both atria and ventricles contract simultaneously.

The heart is a muscle and its structure is composed by three layers: the outer pericardium, the middle myocardium and the inner endocardium. Pericardium is connective and deep adipose tissue, and it protects the heart by external agents, dye to a reduced friction with surrounding structures.
Myocardium is a thick layer, mostly made up of cardiac muscle tissue, organized in planes and richly supplied by blood capillaries, lymph capillaries and nerve fibers. Its contraction pumps blood out of the heart chambers.
The endocardium is made an epithelium with connective tissue and elastic and collagenous fibers. It also contains blood vessels and specialized cardiac muscle fibers known as Purkinje fibers, [20].

13
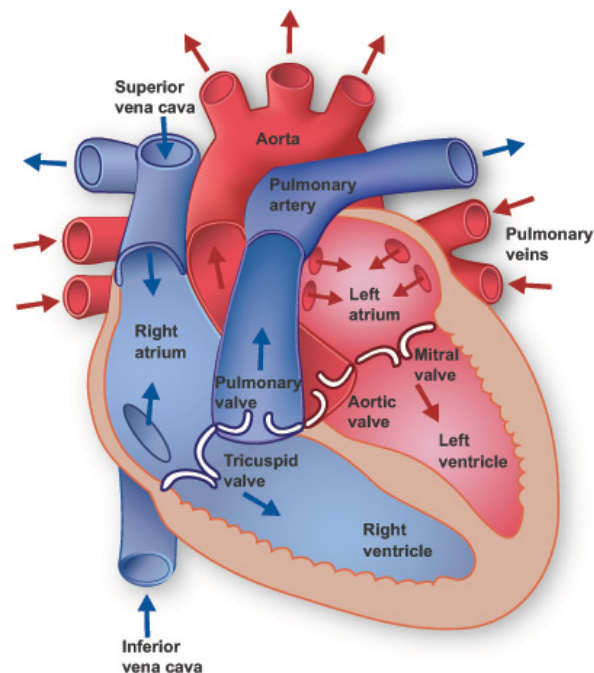
Figure 1.1: Schematic diagram of heart anatomy and cardiac cycle

1.1.1 Cardiac cycle

Cardiac cycle describes the process of relaxation and contraction that occurs when the heart pumps blood through the body. Systole, or contraction, of the heart is stimulated by the electrical activity of heart's natural pacemaker cells. They are activated by a spontaneous depolarization of their membranes beyond a certain threshold for excitation. Diastole is the relaxation that follows the contraction; it represents the period of refilling with circulating blood.

This cardiac cycle is coordinated by the cardiac conduction system, made up of excitable and contractile cells. The peculiar property of being excitable cells allows the action potential to propagate autonomously. The action potential itself causes the contraction, enabling blood pumping.

The electrical activity of the heart starts in a group of cells, known as the sinoatrial node, located just below the superior cava vein, on the right atrium, as describe in Figure 1.2. The cells in the sinoatrial node are autonomous oscillators, and they are able to reach the threshold on their own. The action potential they generate is then propagated through the atria. The impulse passes along junctional fibers of the conduction system, reaching another region of specialized tissue. This is the septum between atria and ventricles, composed by nonexcitable cells, which normally acts as a barrier to action potential conduction.

Conduction through the atrioventricular node is quite slow. When the action potential exits this node, it propagates through a specialized group of fibers called the bundle of His, which is composed by Purkinje fibers. The Purkinje fiber network spreads via tree-like branching into the left and right bundle branches throughout the inner part of the ventricles, ending on

the endocardial surface of the ventricles. As soon as the action potentials emerges from the Purkinje fiber–muscle junctions, it can activate the ventricular muscles and propagate through the ventricular wall outward, reaching the epicardial surface.
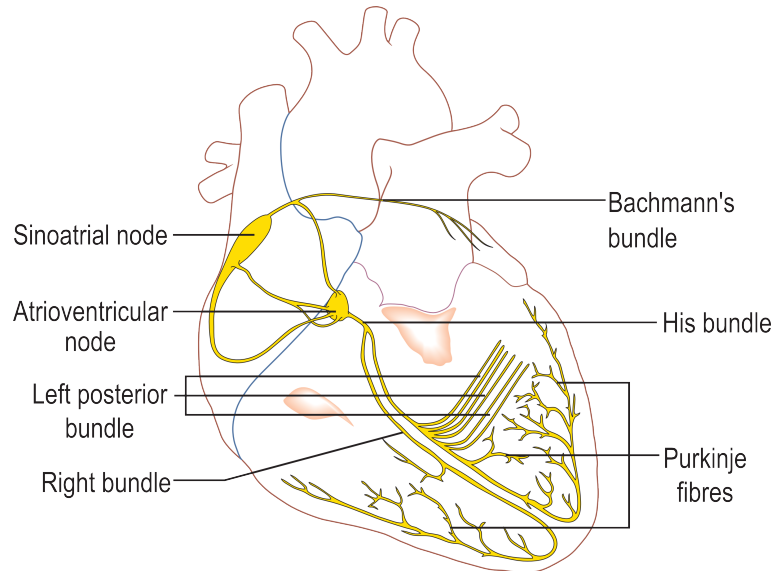
Figure 1.2: Schematic view of the conduction system of the heart

1.1.2 Action Potential

The cardiac action potential (AP) is actually the physiological basis of the ECG. It is a temporary change in voltage across cells, due to the movement of charged ions through membrane proteins. These proteins are called ion channels.

There are important physiological differences between cells that spontaneously generate the action potential and those ones that conduct it. The primary cell types of cardiac cells are nodal cells, Purkinje fiber cells, and atrial and myocardial cells, each with a slightly different function. For instance, the sinoatrial nodal cell primary function is to provide a pacemaker signal, while Purkinje fiber cells are functional to fast conduction. Because of these different functions, these cell types have different action potential shapes. Even within a single cell type, there can be substantial variation. For example, in the ventricles, epicardial, midmyocardial, and endocardial cells have noticeable differences in action potential duration, [42].

Moreover, differences in AP morphologies through apex-to base direction of the ventricle affect the distribution of the action potential in the whole space. For example, heterogeneous properties of myocytes embedded in the ventricular wall cause a spatial dispersion of the AP duration.

In addiction to the spatial dispersion, the AP duration could also show a temporal dispersion. This is due to beat-to-beat changes alternating between short and long action potentials.

We now use the standard model of the ventricular myocyte to analyse the cardiac action

potential, presented in Figure 1.3. It can be divided into five phases, depending on the flux of Sodium (Na^+), Potassium (K^+), Chlorine (Cl^-) and Calcium (Ca^{2+}) ions.

Phase 0**: Upstroke or Rapid Depolarization** The action potential begins with a depolarizing stimulus big enough to reach a threshold and generate an abrupt increase. In quiescent, non pacemaker cells, it is generally due to the opening of the voltage-activated Na^+ channels that causes a rapid increase in the membrane conductance and a rapid increase of Na^+ ions into the cell. This rapid influx of Na^+ ions is expressed by the inward I_{Na} current. The rate of depolarization during phase 0, expressed as dV/dt, is a reasonable approximation of the rate and magnitude of Na^+ influx and a determinant of conduction velocity for the propagated action potential, [115].

Phase 1**: Early Rapid Depolarization** This phase occurs with the rapid inactivation of the Na^+ channels that reduces the movement of sodium into the cell. At the same time, potassium and chlorine channels open and close rapidly, causing a flow of K^+ and Cl^- ions out of the cell. These ions are carried by I_{to1} and I_{to2} currents and make the membrane potential slightly more negative, [107].
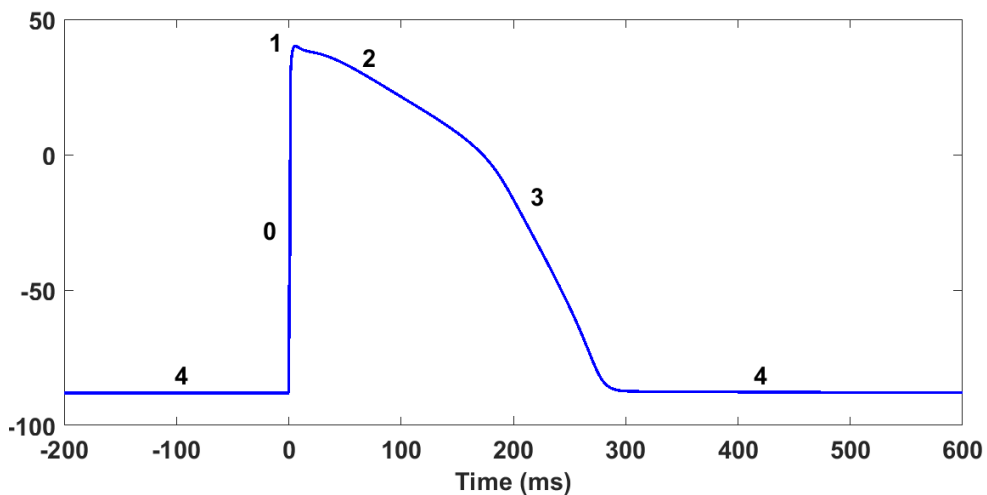
Figure 1.3: A cardiac action potential: phase 0 (upstroke), phase 1 (voltage peak), phase 2 (plateau), phase 3 (repolarization), phase 4 (resting)

Phase 2**: Plateau** In this phase the membrane potential remain almost constant (the membrane repolarizes extremely slowly), because of the charge balancing into and out of the cell. In this way, slow delayed rectifier potassium channels allow K^+ to leave the cell (generating the I_{ks} current), while L-type calcium channels allow the movement of Ca^{2+} into the cell (I_{Ca} current). This calcium opens more calcium channels located into the sarcoplasmic reticulum (SR) into the cell, and, in turn, induces the release of calcium from the SR. This calcium release is responsible for heart contraction.
The plateau phase is responsible for the long duration of the action potential, [34].

Phase 3**: Final Rapid Repolarization** During the third phase, the L-type Ca^{2+} channels close and the slow delayed rectifier K^+ channels remain open. This activity corresponds to a

negative change in membrane potential, that allows different types of potassium channels to open, such as the rapid delayer rectifier K^+ channels and the inwardly rectifying K^+ current. Membrane repolarization is exactly due to this outward current, corresponding to the loss of positive charge from the cell.

The delayed rectifier channels close at the begin of phase 4, whereas the inward rectifier channels and the ion pumps remain active. This means that the calcium used for muscle contraction is pumped out of the cell, resulting in muscle relaxation, see [19].

Phase 4**: Resting membrane potential** This phase is responsible for the diastole, when the cell is at rest. The major ion that determines the resting potential is extracellular potassium concentration. For these reasons, the resting potential is maintained close to the potassium equilibrium potential, that is about $-84mV$, [115].

1.2 Modeling of Cellular components

Mathematical models of cardiac cellular electrophysiology evolved significantly over the last 50 years. A large amount of experiments was performed to achieve knowledge concerning the cardiac electrophysiology, obtaining data and quantities from specific function regions. Examples are voltages across membranes and through different spatial domains, flow and concentrations of ions.

The measurement data were partly used to create mathematical models, such as the models of membrane patches, of single cells and of cell clusters. Models allow the simulation of the electrophysiological behaviour with numerical methods, [116].

First of all, we should be able to model the physiology of a generic cell, and after that take in consideration specialized cell, as cardiac ones. The description of the electrophysiology of cellular components should start from the behaviour of the cell membrane and the transport of ions through the channels and exchangers. This kind of transport is determined by gradients of ionic concentrations and electrical forces.

1.2.1 Cell membrane

The cell membrane consists of a phospholipid bilayer, perforated by pores, made up of proteins. The main function is to suppress the diffusion of ions and molecules in and out of the cell and it separates the intra- and extracellular space with different ionic concentrations. The gradient of ionic concentrations results from both transport and cellular mechanisms.

The electrical behaviour of a cellular membrane can be measured with different methods, but the most used is the patch clamp technique. In this case the voltage over the membrane is kept constant by supplying a convenient current. This system allows to record the voltage and the course of current, even though voltage measurements are varied stepwise. Measurements are often performed in conjunction with the application of drugs, which allows the discrimination of the involved currents and channels, [106].

The best way to describe the electrical activity of the membrane is by a resistor-capacitor
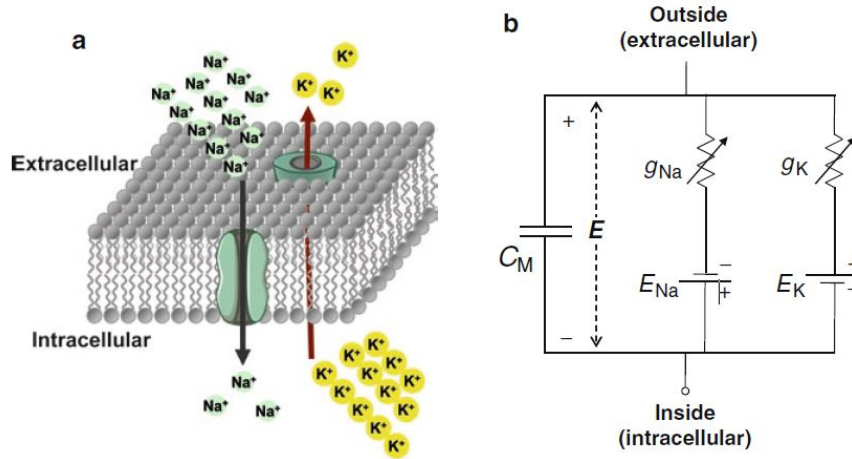
Figure 1.4: Three-dimensional view of a representative section of a schematic plasma membrane with embedded proteins (a) and an equivalent circuit (b), see[116].

circuit, as in Figure 1.4. By definition, the capacitance is

$$C_m = \frac{Q}{V}$$

where V is the voltage potential drop over the membrane, Q is the charge across the capacitor and C_m is assumed to be constant.

With this notation, the change of the transmembrane voltage can be described by the capacitative current

$$I_{cap} = \frac{dQ}{dt} = \frac{d(C_m V)}{dt} = C_m \frac{dV}{dt}$$

Using this equation, the current conservation low becomes

$$C_m \frac{dV}{dt} + I_{ion} = I_{app}$$

where I_{ion} is the sum of the ionic currents and I_{app} is the applied current.

Nernst Equilibrium Potential

The other phenomenon that could be described is how a difference in ionic concentration can result in a potential difference across the membrane separating the two concentrations. The resulting voltage is generated by electrical and chemical forces and can be described by different equations. The suitable constitutive law for the equilibrium voltage across the border of two regions is the Nernst-Planck equation, [35].

Given a ion k with valence z, the equilibrium is achieved when each local process and its reverse proceed at the same rate. This means that the total flux J through the membrane at thermodynamical equilibrium is zero. In this specific case, the total flux is the sum of two contributions: the diffusion flux and the electrical one.

The ion motion by the electric field causes an electric flux, satisfying Planck equation

$$J_E = -\frac{z}{|z|}\mu c \nabla u,$$

where u is the electric potential and μ is the ion mobility.

On the other hand, the ion motion down the concentration gradient causes a diffusion flux J_D, that satisfies the Fick law

$$J_D = -D\nabla c,$$

where c is the concentration and $D = \frac{\mu RT}{|z|F}$ is the diffusion coefficient.

In conclusion, the equilibrium is achieved if

$$J = J_D + J_E = -D\nabla c - \frac{z}{|z|}\mu c \nabla u = 0.$$

Using the relation between the diffusion coefficient and the ionic mobility, the total ionic flux is described by the Nernst-Planck equation

$$J = -D\left(\nabla c + \frac{zF}{RT}c\nabla u\right) \tag{1.1}$$

and the equilibrium corresponds to the equation

$$D\nabla c = \frac{zF}{RT}c\nabla u. \tag{1.2}$$

Let's now consider a cell membrane that extends from $x = 0$ (inside) to $x = L$ (outside), with a constant diffusion coefficient D. Using the standard notation, we'll denote intercellular quantities with the index i and extracellular quantities with the index e. That are, for example, ionic concentrations $c_i := c(0)$ and $c_e := c(L)$ and potentials $u_i := u(0)$ and $u_e := u(L)$.

At the steady state the concentration does not change and equation (1.2) reduces to the a dimensional problem in $c(x)$

$$\frac{dc}{dx}(x) + \frac{zF}{RT}\frac{du}{dx}(x)c(x) = 0.$$

This linear differential equation, integrated in $(0, L)$, gives as solution:

$$c(L) = \exp\left(-\frac{zF}{RT}(u(L) - u(0))\right)c(0).$$

Using the standard notation written above, the solution yields

$$V_{eq} := u_i - u_e = -\frac{RT}{zF}\log\left(\frac{c_i}{c_e}\right), \tag{1.3}$$

that is the Nernst equation for the equilibrium potential, derived in 1888, [19]. The only limit of this mathematical result is that the formulation includes only one kind of ion.

Generic reversal potential

The assumption that biological membranes are permeable to a single ion only is not valid, and even low permeabilities may have an important effect. The Goldman-Hodgkin-Katz equation was developed to extend the Nernst equation by allowing the occurrence of multiple kinds of ions. First of all, this model assumes that the membrane is uniform, planar, and infinite in its lateral extent. Then, the variation of the potential field and the ionic concentration within the membrane are functions of x only. With the same standard notation used above, and the definition $V := u(0) - u(L) = u_i - u_e$, we can suppose the electric field constant across the membrane, that is

$$\frac{du}{dx} = -\frac{V}{L}.$$

This corresponds to the steady state.

In this case, we'll have different ions and different fluxes, and each of them will be marked with the index k. Every flux satisfies the Nernst-Planck Equation (1.1), thus get for the kth flux

$$J_k = -D_k \left(\nabla c_k + \frac{z_k F}{RT} c \nabla u \right). \tag{1.4}$$

Once again, equation 1.4 can be reduced to the one dimensional problem in $c(x)$

$$\frac{dc_k}{dx}(x) + \frac{z_k F}{RT} \frac{du}{dx}(x) c_k(x) + \frac{J_k}{D_k} = 0.$$

This linear differential equation, integrated in $(0, x)$, gives as a solution

$$c_k(x) = \frac{J_k RTL}{D_k z_k VF} \left(1 - \exp\left(\frac{k_k VF}{RTL} x \right) \right) + c_i \exp\left(\frac{z_k VF}{RTL} x \right).$$

Unfortunately, to find out the equilibrium potential, it's necessary to know every current, in order to sum them. For this reason, we solve the previous equation for J_k, giving

$$J_k = \frac{D_k z_k FV}{LRT} \frac{c_i - c_e \exp\left(-\frac{z_k VF}{RT} \right)}{1 - \exp\left(-\frac{z_k VF}{RT} \right)}.$$

We can now use this result to find the electrical current density $I_k := z_k F J_k$, that is

$$I_k = \frac{P_k z^2 F^2}{RT} \frac{c_i - c_e \exp\left(-\frac{z_k VF}{RT} \right)}{1 - \exp\left(-\frac{z_k VF}{RT} \right)} \tag{1.5}$$

where $P_k = \frac{D_k}{L}$ is the permeability of the membrane to the ion k. Equation 1.5 is called Goldman-Hodgking-Huxley equation and gives an important voltage-current relation.

When considering the ion flux through the membrane at the resting state, the sum of all currents through the membrane is necessarily zero. If we consider the main contributors

(potassium, sodium, and chloride ions), we may write

$$I_L + I_{Na} + I_{Cl} = 0.$$

By substituting in each current the corresponding voltage-current relation (1.5), and noting that potassium sodium valences are $z = +1$, while chloride one is $z = -1$, we find that

$$v_r = -\frac{RT}{F} \log \frac{P_{Na} c_{i,Na} + P_K c_{i,K} + P_{Cl} c_{i,Cl}}{P_{Na} c_{e,Na} + P_K c_{e,K} + P_{Cl} c_{e,Cl}}. \tag{1.6}$$

This meas that the relative contribution of each ion species to the resting potential (1.6) is weighted by that ion's permeability, [72].

Anyway, in this field, it's commonly used the linear current-voltage relation, derived by approximation of a constant diffusive gradient. Using two types of ions with opposite valences, Poisson-Nernt-Planck model leads to the electrical current density

$$I_k = G_k(V - v_k), \tag{1.7}$$

where v_k is the Nernst potential of the ion k ((1.2)) and $G_k = \frac{zFD}{L} \frac{c_{e,k} - c_{i,k}}{v_k}$.
Considering again the main contributors (potassium, sodium and chloride ions), we find the resting potential

$$v_r = -\frac{G_{Na} V_{Na} + G_K V_K + G_{Cl} V_{CL}}{G_{Na} + G_K + G_{Cl}}. \tag{1.8}$$

1.2.2 Ionic Channels

A single ionic channel flips randomly between a conducting and non-conducting state. Trough measurements of the stochastic opening and closing over a period of time, it is possible to assign to every channel a specific probability of opening and closing.
If we consider a population of ions channels, we find that its behaviour is the sum of the single channel behaviours.

Sodium channels are responsible for the fast depolarization in myocytes, and voltage clamp measurements show a fast transition to the high conductivity state if the voltage exceeds a threshold. Furthermore, the conductivity is significantly time dependent and decreases rapidly after activation.

Potassium channels are responsible for the repolarization of myocytes and neurons. They show several different behaviours: there are channels responsible for the ultra-rapid delayed rectifier current, some other for the slowly activating delayed rectifier current, and even the inward rectifier current.

Calcium channels are differentiated into two types. L-type calcium channels show relatively large and long lasting ion flow after activation. T-type channels show a tiny and transient ion flow.

The $Na^+ - K^+$ pump transports sodium and potassium ions in and out of the cell, consuming

ATP. In every single procedure, three Na^+-ions go into the cell, while two K^+-ions go outside. The transport depends on different factors, such as ions concentration, transmembrane voltage and temperature.

The Calcium pump transports calcium out of the cell, using ATP.

The main responsible of the calcium transport out of the cell is the Na-Ca exchanger. In a single procedure three extracellular sodium ions are exchanged with a single intracellular calcium ion, [35].

Consider a membrane portion of unit area containing a given type of ionic channels. The behaviour of a single ionic channel can be modeled with functions describing the transition between conducting and non-conducting states. In the simplest case two states are assumed: S_0 as opened and S_1 as closed. Assuming a stochastic transition, it's usual to assign an opened probability s_0 and a closed probability s_1, that reflects percentages of close and open channels per unit area of the surface membrane, [106].

Using a first order kinetic with transition rate constants α and β, such that $S_0 \xrightarrow{\alpha} S_1$ and $S_1 \xrightarrow{\beta} S_0$, we find

$$\begin{cases} \dfrac{ds_1}{dt} = \alpha s_0 - \beta s_1 \\ s_0 + s_1 = 1 \end{cases}.$$

thus, setting the gating variable $w = s_1$, gating variable, the system becomes

$$\frac{dw}{dt} = \alpha(1 - w) - \beta w. \qquad (1.9)$$

At equilibrium conditions, there is any change in channel state and $\frac{dw}{dt} = 0$; thus, we can define

$$w_\infty = \frac{\alpha}{\alpha + \beta} \qquad \tau_w = \frac{1}{\alpha + \beta}$$

respectively the equilibrium state and the time constant. We can finally write the gating equation

$$\frac{dw}{dt} = \frac{w_\infty - w}{\tau_w}. \qquad (1.10)$$

Transition rate constants depends, in general, on the transmembrane potential V; thus, in a voltage clamp set their new values depends on the fixed v_0. Since these coefficients are constant, the differential equation (1.10) can be solved for w, giving the evolution depicted in Figure 1.5:

$$w(t) = w_\infty(v_0) \left(w_\infty(v_0) - w(0) \right) e^{-\frac{t}{\tau_w}}. \qquad (1.11)$$

Given a population of N ionic channels in a given area S of membrane surface, the function w represents the percentage of open channels. Thus the quantity $g(V,t) = \frac{N}{S}w$ represents the proportion of open channels in a unit area of the membrane surface.

In general, the total current through a population of ionic channels is resulting from the product

$$I_{ion} = g(V,t)I_c(V),$$
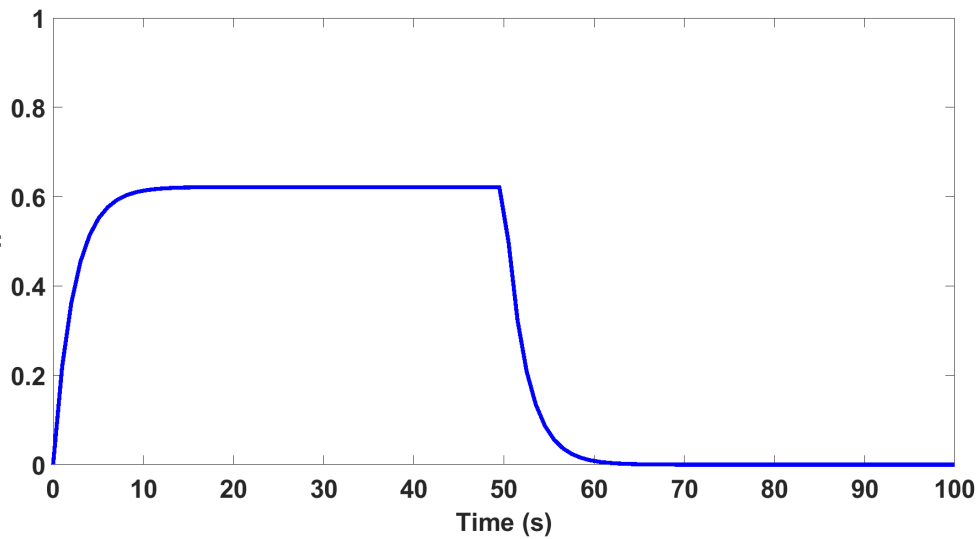
Figure 1.5: Evolution of the gating variable in a specific voltage clamp set: at time $t = 0$, V increases from 0 to $v_0 = -65mV$ and keeps this value until $t = 50$, when it returns back to 0. Thus we have two dynamics: the first in $[0, 50]$ with $w(0) = 0$, the second in $[50, 100]$ with $w(0) = w_\infty$.

where $I_c(V)$ is the current voltage relation of a single open channel.

In the specific case of a linear current voltage relation, equation ((1.7)) yields

$$I_{ion} = g(V, t)I_c(V) = \frac{N}{S}wg_c(V - v_c)$$

where g_c is the channel conductance and v_c is the resting potential. The previous equation is generally written as

$$I_{ion} = \bar{G}_c w(V - v_c), \tag{1.12}$$

where $\bar{G}_c$ is the maximal channel conductance per unit area of the membrane surface, [19]. This is the reason why a ionic channel is generally represented as a resistor with a specific conductance.

1.2.3 Hodgkin-Huxley model

In this context, the classical work of Hodgkin and Huxley (1953) represents the ancestor model of all modern cardiac electrophysiology.

According to the previous formalism, authors divided the total membrane current into capacitative and a ionic currents, using an equivalent electrical circuit (Figure 1.6), made of resistances in parallel to capacity, [25].

Furthermore, they splitted the ionic current into components carried by sodium ions (I_{Na}),
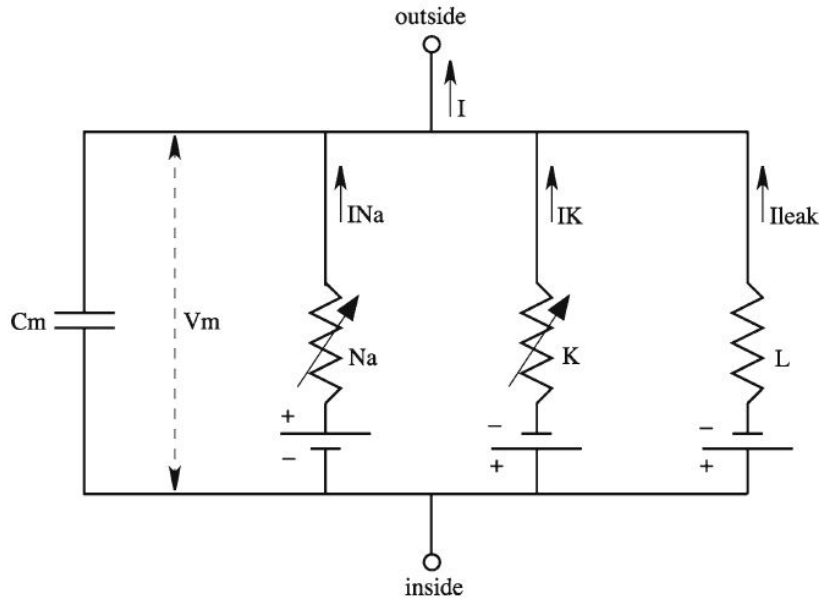
Figure 1.6: The electrical circuit representing the membrane of an electrical excitable cell [116].

potassium ions (I_K) and other ions (I_l, leakage current). Thus

$$\begin{cases} C_m \dfrac{dv}{dt} + I_{ion} = I_{app} \\ I_{ion} = I_{Na} + I_K + I_l \end{cases}$$

The next step they reached was showing that the ionic membrane permeability satisfied the linear current-voltage relation (1.12).
The conductance $G_l = \bar{G}_l = 0.3$ is assumed to be constant, while the other conductances are associated to a resistor with a non linear dynamic. Specifically, the time course of sodium and potassium conductances presents a stochastic behaviour, described for a general ionic channel, [106].

The time dependence of G_K is easy to describe and is based on the assumption that potassium ions can cross the membrane only when four similar particles occupy a certain region of the membrane. Thus, we introduce the gating variable n, that stands for the portion of the particles in a certain position. According to equation (1.9) with the proper transition rate constants α_n and β_n, the formal expression used to describe potassium conductance is

$$\begin{cases} G_K = \bar{G}_K n^4 \\ \frac{dn}{dt} = \alpha_n(1-n) - \beta_n n \end{cases},$$

where $\bar{G}_K = 36$ is the maximal conductance for potassium ions, [36].

Otherwise, sodium conductance is determined by two variables. Each of them obeys a first order equation, because sodium conductance is assumed to be proportional to the number of sites

occupied simultaneously by three activating molecules, without being blocked by an inactivating one. In this case, we'll introduce the activation variable m, and the inactivation one h, satisfying once again the gating variable equation (1.9).

Indicating the transfer rate constants in the two direction, respectively, α_m and β_m for the first gating variable and α_h and β_h for the second one, the formal system that occurs is

$$\begin{cases} G_{Na} = \bar{G}_{Na} m^3 h \\ \dfrac{dm}{dt} = \alpha_m(1-m) - \beta_m m \\ \dfrac{dh}{dt} = \alpha_h(1-h) - \beta_h h \end{cases},$$

where $\bar{G}_{Na} = 120$ is the maximal conductance for sodium ions, [35].

To sum up, replacing every equation depending on the stochastic transition rate with the equivalent formulation depending on the steady state values (that is (1.10)), the formal Hodgkin-Huxley model becomes

$$\begin{cases} C_m \dfrac{dv}{dt} + I_{ion}(V,m,h,n) = I_{app} \\ \dfrac{dm}{dt} = \dfrac{m_\infty(V) - m}{\tau_m(V)} \\ \dfrac{dn}{dt} = \dfrac{n_\infty(V) - n}{\tau_n(V)} \\ \dfrac{dh}{dt} = \dfrac{h_\infty(V) - h}{\tau_h(V)} \end{cases} \tag{1.13}$$

where

$$x_\infty = \frac{\alpha_x(V)}{\alpha_x(V) + \beta_x(V)}, \tag{1.14}$$

$$\tau_x(V) = \frac{1}{\alpha_x(V) + \beta_x(V)}, \qquad x = m, n, h \tag{1.15}$$

and

$$I_{ion}(V,m,n,h) = \bar{G}_{Na} m^3 h(V - V_{Na}) + \bar{G}_K n^4(V - V_K) + \bar{G}_l(V - V_l)$$

is the total ionic current, depending on voltage, [25].

This model is of great importance for the modern cardiac electrophysiology. Furthermore, because of its simple formulation, it is widely used to perform with a reduced effort some preliminary tests for electromechanical frameworks presenting higher numerical complexity. Thus, we developed a C++ code for the HH model, embedded in the $Life^X$ library (Figure 1.7), this one being a high-performance Finite Element library mainly focused on mathematical models and numerical methods for cardiac applications. It is written in C++ using the most modern programming techniques available in the C++17 standard and is based on the deal.II finite element core, [1].
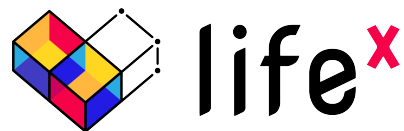

Figure 1.7: Official $Life^X$ logo, [1]

1.3   Modeling of Cardiac myocytes

Following the Hodgkin-Huxley (HH) formalism, various kinds of HH-type models of neurons and other excitable cells are proposed. The HH-type equations include many variables, depending on the number of different ionic currents and their gating variables considered in the models, whereas the original formulation possess only four variables.

For this reason it could be useful to formalize the general structure of a cardiac membrane model, with N ionic currents and M gating variables. The dynamics of gating variables $\boldsymbol{w} := (w_1 \ldots w_M)$ is described by the system of ODEs:

$$\begin{cases} \dfrac{d\boldsymbol{w}}{dt} = R(V, \boldsymbol{w}) \\ \boldsymbol{w}(0) = \boldsymbol{w_0} \end{cases} \tag{1.16}$$

where $R_j(V, \boldsymbol{w}) = \frac{dw_j}{dt} = \alpha_j(V)(1 - w_j) - \beta_j(V)w_j, \quad j = 1 \ldots M$, that is the general gating variable equation, used in the HH formalism.

In addiction to the HH formalism, we need to introduce concentrations. Considering S intercellular concentration variables, the dynamic of the vector $\boldsymbol{c} := (c_1 \ldots c_S)$ is given by the system:

$$\begin{cases} \dfrac{d\boldsymbol{c}}{dt} = S(V, \boldsymbol{w}, \boldsymbol{c}) \\ \boldsymbol{c}(0) = \boldsymbol{c_0} \end{cases} .$$

In this case, for the specific ion c_j, we have $S_j(V, \boldsymbol{w}, \boldsymbol{c}) = \frac{dc_j}{dt} = -\frac{I_{c_j}(V, \boldsymbol{w}) A_{cap}}{V_{c_j} z_{c_j} F}$ for $j = 1 \ldots S$, where I_{c_j} is the sum of ionic currents carrying the ion, A_{cap} is the capacitive membrane area, V_{c_j} is the volume of the compartment and z_{c_j} is the ion valence.

To sum up, the evolution of the transmembrane potential of a single myocyte is given by the generalization of the system (1.13):

$$\begin{cases} C_m \dfrac{dV}{dt} + I_{ion}(V, \boldsymbol{w}, \boldsymbol{c}) = I_{app} \\ \dfrac{d\boldsymbol{w}}{dt} = R(V, \boldsymbol{w}) \\ \dfrac{d\boldsymbol{c}}{dt} = S(V, \boldsymbol{w}, \boldsymbol{c}) \\ V(0) = v_0, \qquad \boldsymbol{w}(0) = \boldsymbol{w_0}, \qquad \boldsymbol{c}(0) = \boldsymbol{c_0} \end{cases} \tag{1.17}$$

where the ionic current of the membrane I_{ion} depends on the concentration variables too, through the reversal potential. Being more precise, with the standard notation for the membrane conductance G_k and the reversal potential v_k, the ionic current has the general structure

$$I_{ion} = \sum_{k=1}^{N} G_k(V, \boldsymbol{c}) \sum_{j=1}^{M} w_j^{p_{j_k}} (V - v_k(\boldsymbol{c})) + I_n(V, \boldsymbol{w}, \boldsymbol{c}),$$

where p_{j_k} are integers and I_n is the sum of time independent ionic fluxes, [19].

In the last years a large number of HH-type models of myocytes was constructed, with

increasing abilities to describe the different electrophysiological mechanisms.

Different families of ionic models have been proposed: *(i)* phenomenological models, which are simple and constructed to reproduce the macroscopic behaviour of the cell in terms of V; *(ii)* first generation models, which reproduce the macroscopic behaviour and the physiology of the cell by accounting the most important ionic currents; *(iii)* second generation models, which provide a very detailed description of the cell behaviour.

HH-type models and the computational physiology on cardiac cells started with the Noble model (1962), which is a model of excitable membrane of Purkinje fibres. Twenty years later, the development of single channel recording technology allowed quantitative measurements of various ionic channels, thus DiFrancesco and Noble (1985) developed the model of Purkinje fibres, [116]. Anyway, we will focus on cardiac ionic models of ventricular cells.

1.3.1   Beeler and Reuter model

In 1977, Beeler and Reuter published the first mathematical model of a mammalian ventricular myocyte. Their work became the framework for development of later more comprehensive models of cardiac ventricular action potentials and has been used extensively in simulations of AP propagation in multicellular models of cardiac tissue.
This model incorporates only four intercellular currents (see Figure 1.8): an initial fast inward current carried primarily by sodium, I_{Na}; a secondary or slow inward current, I_s, carried mainly but not exclusively by calcium ions; a time activated outward current designated I_{x1}; and a time-independent potassium outward current designated I_{K1}. Thus

$$I_{ion} = I_{Na} + I_s + I_{x1} + I_{K1}.$$

Variables of the model are the transmembrane voltage V_m and six activation and inactivation parameters m, h, j, d, f, x_1 controlling the conductance of the membrane. Each of these parameters is governed by a Hodgkin-Huxley equation (1.16) with specifically chosen transfer rate coefficients. It was also discovered that the intracellular calcium concentration changes during the course of an action potential, thus $[Ca^{2+}]_i$ was included in the model as an additional dynamic variable.

The **fast sodium current** (I_{Na}) is primarily responsible for the rapid upstroke of the action potential. It was adapted from Hodgkin and Huxley, using the same activation gate m and the inactivation gate h, with the addition of a slow inactivation gating variable j. Thus the final formulation of the fast sodium current is:

$$I_{Na} = \left(g_{Na}m^3hj + g_{NaC}\right)(V - E_{Na})$$

with the Nernst voltage of sodium $E_{Na} = 50mV$, the maximal sodium conductance g_{Na} and the background sodium conductance g_{NaC}, chosen to reproduce the measured steady sodium leakage current.

The **slow inward current** I_S, primarily carried by calcium ions, influences the duration of
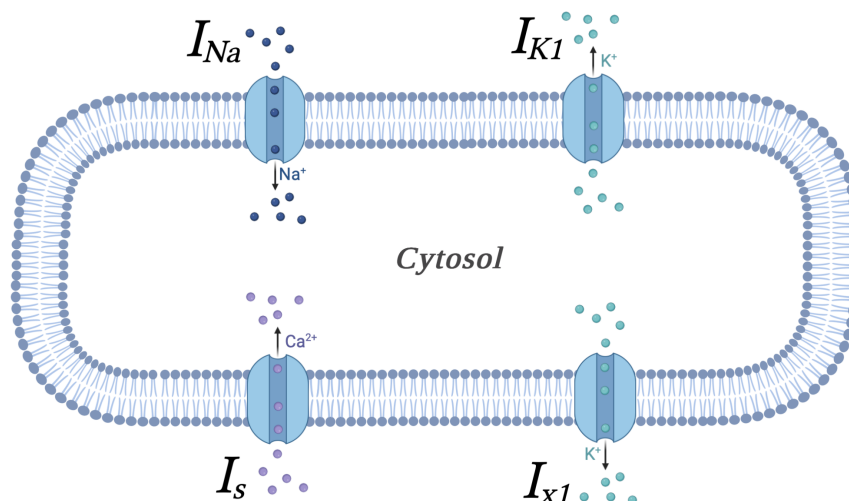
Figure 1.8: Schematic diagram of the Beeler-Reuter cell model used.

the AP. The Ca^{2+} influx is modeled by the equation

$$I_s = g_s df(V - E_s)$$

activated by d and inactivated by f.

Since the reversal potential $E_s = -82.3 - 12.0287 \cdot \log(0.001[Ca^{2+}]_i)$ is calcium-dependent, the internal Ca^{2+} concentration must be tracked, via

$$\frac{dc}{dt} = 0.07(10^{-1} - c) - 0.01 \cdot I_s$$

where $c = [Ca^{2+}]_i$.

The two outward currents are instead responsible for the repolarization phase and mediate the return to the resting potential. The **time-dependent potassium current** I_{x1} is controlled by a single gating variable $x1$ and satisfies the equation

$$I_{x1} = 8 \cdot 10^{-3} x_1 \left(\frac{e^{0.04(V+77)} - 1}{e^{0.04(V+35)}} \right)$$

while the **time-independent potassium current** I_{K1} depends on the voltage only, [13].

Although the Beeler–Reuter model has had a fairly long and robust run of popularity, it happened that gradually updated models replaced it. The first modification was about Na^+ current. Because of the rapid activation, it was not possible to measure accurately the inward current and, as a result, all the early models used the HH formulation. As a consequence, there wasn't a sufficient rapid upstroke for the action potential, and this had an important effect on the propagation speed for propagated APs.

Once appropriate data became available, it was possible to suggest an improved description of

the sodium inward current.

1.3.2 Luo-Rudy model

The Luo-Rudy model describes the electrophysiology of a ventricular cell from guinea pig based primarily on data from single-cell and single-channel measurements.
The authors' activity can be divided into two parts, thus they published two different works, with significant differences, in 1991 and 1994, see [64].

The passive model

The first phase of the Luo-Rudy model describes the electrophysiology of a ventricular cell, published in 1991, based primarily on data from single-cell and single-channel measurements. The model results as a a succession of the Beeler-Reuter model using similar formulations for the fast sodium current and the slow inward current.
In the model, the extracellular concentrations of ions are fixed. This is the reason why it's usually identified with a passive model: the ion concentration is unchanged, thus the model cell is always alive or no chance to die. Anyway, because of the effects of potassium concentration on the time course of repolarization, they introduced in the model this dependence on potassium current.

The model incorporates six intercellular currents, that can be divided in two inwards and four outward (see Figure 1.9). Thus

$$I_{ion} = I_{Na} + I_{si} + I_K + I_{K1} + I_{Kp} + I_b$$

Variables of the model are the transmembrane voltage V_m, the intercellular calcium concentration $[Ca^{2+}]_i$, and seven activation and inactivation parameters m, h, j, d, f, x, x_i controlling the conductance of the membrane. Each of these parameters is governed by a Hodgkin-Huxley equation (1.16) with specifically chosen transfer rate coefficients, [106].

The **fast sodium current** (I_{Na}) is time dependent. It has the usual HH formulation, with the omission of the constant background sodium conductance. Thus the final formulation of the fast sodium current is:

$$I_{Na} = g_{Na} m^3 h j \left(V - E_{Na}\right)$$

with the Nernst voltage of sodium $E_{Na} = 50mV$, the maximal sodium conductance g_{Na}.

The **Slow inward current** (I_{si}) corresponds to the I_s current in the Beeler and Reuter model, thus it has the same formulation. Furthermore, this current depends on $[Ca^{2+}]_i$ and is directly linked to calcium dynamic.

The **Time-dependent potassium current** (I_K) is the last dependent current of the model. It was adapted from the existed model, using the same activation gate x, with the addition of the inactivation gating variable x_i. Thus the final formulation of the fast sodium current is:

$$I_K = g_K x x_i \left(V - E_K\right).$$
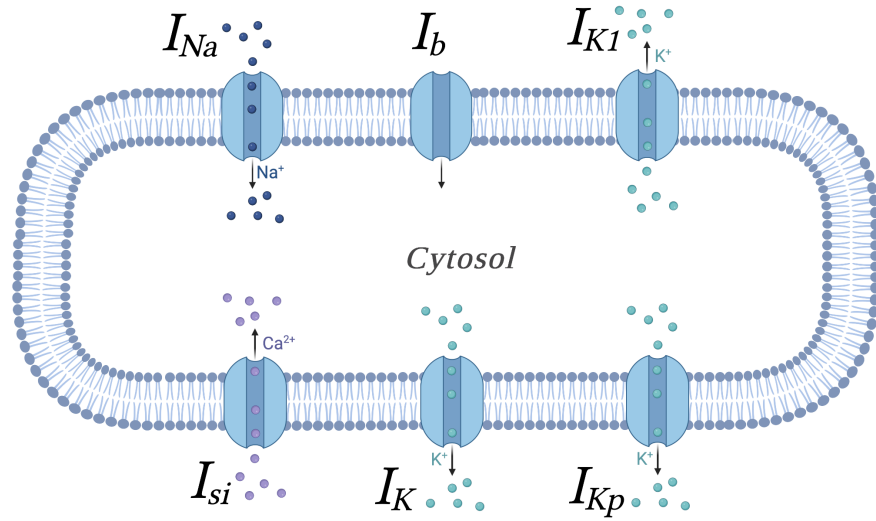
Figure 1.9: Schematic diagram of the currents considered in the Passive Luo Rudy model.

Here, the gating variable x is governed by the usual Hodgkin-Huxley equation (1.16), while the inactivation variable x_i has a different dynamic.

Furthermore, potassium reversal potential E_K depends for the first time on the concentrations of both K^+ and Na^+ and follows the equation

$$E_K = \frac{RT}{F} \log \left(\frac{[K^+]_o + PR_{NaK}[Na^+]_o}{[K^+]_i + PR_{NaK}[Na^+]_i} \right),$$

where PR_{NaK} stands for the permeability ration for Na^+, relative to K^+.

The **Time-independent potassium current** is the first of the three currents that does not depend on any gating variable. In this specific case, the variable was approximated by the steady state formulation $K1_\infty$, by using a time constant small enough. Thus the current magnitude is

$$I_{K1} = g_{K1}K1_\infty(V - E_{K1}),$$

where, once again, the maximal potassium conductance, depends on the extracellular potassium concentration, [19].

The **Plateau potassium current** I_{Kp} restores the cell to the resting state, and

$$I_{Kp} = g_{Kp}K_p(V - E_{Kp})$$

where $E_{Kp} = E_{K1}$ and K_p depend on the membrane voltage only.

The **Background current** I_b is a linear function, that is

$$I_b = g_b(V - E_b),$$

where the maximal conductance and the reversal potential are fixed values,see [65].

Calcium dynamic

In the second phase of Luo-Rudy's work, I_{Ca} is reformulated on the basis of the most recent data from single cell and single-channel experiments. Other processes are also incorporated in the new model, but the most important difference is due to the new formulation of calcium dynamic. The mechanisms by which a cell controls its Ca^{2+} concentration are of central interest in cell physiology, because prolonged high cytoplasmic calcium concentration is toxic. Thus, lots of control mechanisms operate on different levels, in order to ensure that this substance does not exceed in the wrong places.

Calcium is removed from the cytoplasm in two principal ways: it is pumped out of the cell across the plasma membrane, and it is sequestered into internal compartments, such as the SR. Since the Ca^{2+} concentration in the cytoplasm is much lower than either the extracellular concentration or the concentration inside the internal compartments, both these methods require a large amount of energy, [113].

On the same way, calcium influx occurs via two principal pathways: inflow through Ca^{2+} channels in the plasma membrane and release from internal stores. In the specific case, calcium release form SR is mediated principally by two types of Ca^{2+} channels that also have the role of receptors.

The ryanodine receptor, so called because of its sensitivity to the plant alkaloid ryanodine, plays an integral role in excitation–contraction coupling in skeletal and cardiac muscle cells. This protein underlies Ca^{2+}-induced Ca^{2+} release, whereby a small amount of calcium entering the cardiac or skeletal muscle cell through calcium channels initiates an explosive release of Ca^{2+} from the SR, [42].

The Calcium-Induced Calcium-Release. Structurally, the SR consists of junctional sarcoplasmic reticulum (JSR) and network sarcoplasmic reticulum (NSR). The network SR is formed by a series of interconnected tubules that span the region between the transverse-tubules (T-tubules). The junctional SR is the place where this organelle forms specialized junctions with the sarcolemmal T-tubules, which result in the close juxtaposition of ryanodine-sensitive calcium channels (RyRs) in the SR and sarcolemmal voltage-gated L-type channels, [134].

During excitation-contraction coupling, membrane depolarization opens L-type calcium channels near the junctional SR. This allows a small amount of Ca^{2+} to enter the small cytosolic volume that separates the SR and the T-tubule sarcolemma, rising local calcium concentration beyond a threshold for RyRs activation. This mechanism is known as Calcium-Induced Calcium-Release (CICR), [10].

While the CICR mechanism initiates the transient elevation of intracellular calcium concentration in both ventricular and atrial myocytes, there are substantial spatiotemporal differences in the properties of atrial and ventricular calcium transient. For example, in ventricular myocyte the Ca^{2+} release is virtually uniform throughout the cell, while in atrial myocyte the Ca^{2+} wave arises in the junctional SR, in the periphery, and propagates to the center of the cell, activating secondary release from the other SR compartment, [28].

To sum up, the update to the model consists of considering different calcium concentration in different cellular parts. Thus, we'll next include in the model:

$[Ca^{2+}]_i$: cytoplasmic concentration of free calcium;

$[Ca^{2+}]_{jsr}$: junctional SR free calcium concentration;

$[Ca^{2+}]_{nsr}$: network SR free calcium concentration.

The dynamic model

The Luo-Rudy dynamic model, published in 1994, is an extension of the passive model and describes the electrophysiology of a ventricular cell. It includes not only sodium and potassium channels of previous models, but also introduces sodium-potassium pump, calcium pump, L-type calcium channel, non-specific calcium-activated channel, sodium-calcium exchanger on the membrane as well as calcium-induced calcium release channel and calcium pump on the membrane of SR with calcium buffers in the myoplasm.

In the dynamic model the cell is considered alive. To achieve this goal, it needs the ions to go back after firing an action potential in order to maintain the intracellular ion balance. Thus, in a shot of AP, potassium ions leave out of the cell, sodium ions get into the cell from extracellular space and calcium ions get into the cells both from extracellular space and for SR. So, ion pumps are required in the cell membranes and SR to maintain the ion balance inside the cell, [25].

The model incorporates 11 intercellular currents, see Figure 1.10. Thus the ionic current results only as an extension of the passive model, that is

$$I_{ion} = I_{Na} + I_{CaL} + I_K + I_{K1} + I_{Kp} + I_{NaCa} + I_{nsCa} + I_{pCa} + I_{NaK} + I_{bCa} + I_{bNa}.$$

Variables in this first part of the model are the transmembrane voltage V_m, and eight activation and inactivation parameters $m, h, j, d, f, X_{s1}, X_{s2}, X_r$ controlling the conductance of the membrane. Each of these parameters is governed by a Hodgkin-Huxley equation (1.16) with specifically chosen transfer rate coefficients. The intracellular ions concentration are variables of the model too, whose equation will appear later, [106].

The **fast sodium current** (I_{Na}) has the same formulation of the passive model, except for the decreasing of the maximal conductance.

The **L-Type Calcium current** (I_{CaL}) corresponds to the slow inward current I_{si}. The L-type channel is permeable to Ca^{2+}, Na^+, K^+, with different permeability ratios. Thus, the total current through this channel is expressed as the sum of the individual components current, that is

$$I_{CaL} = I_{CaLCa} + I_{CaLNa} + I_{CaLK}.$$

Here, because there is only one physical channel, each of these terms is governed by the same gating variables, obtaining

$$I_{CaLX} = d \cdot f \cdot f_{Ca} \cdot \bar{I}_{CaLX}$$

with $\bar{I}_{CaLX}$ the maximal current through the channel for the X ion specie, with $X = Ca, Na, K$.
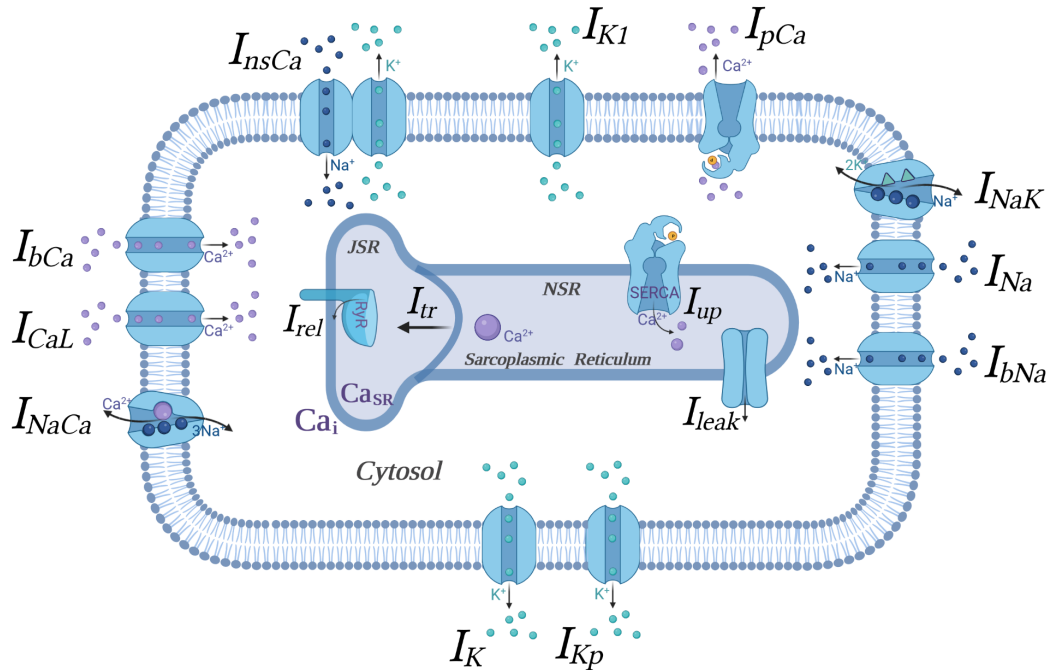
Figure 1.10: Schematic diagram of the currents considered in the Luo Rudy dynamic model. The intracellular compartment is the SR, which is divided into the two subcompartments. Ca^{2+} buffers are present in both the cytoplasm and the JSR.

Once again, d represents the usual activation variable, f represents the usual inactivation one, while f_{Ca} is a new inactivation variable, whose equation depends on the intercellular calcium concentration.

Just one year later, in the first update appeared the T-type calcium current, governed by two gating variables. Their name is due to their activities: the L-type current appears long lasting, if compared to the transient calcium current.

The **Time-dependent potassium current** (I_K) has the same formulation of the passive model, with an additional activation gate. Thus, we find

$$I_K = g_K x^2 x_i \left(V - E_K \right),$$

where the inactivation gate has a different dynamic.

In other terms, this current represents the rapid potassium kinetic.

The **Time-independent potassium current** does not change its formulation, except for the maximal potassium conductance.

In other updates, this term represents the slow potassium current.

The **Plateau potassium current** I_{Kp} does not show any change in its equations.

The **Sodium-calcium exchanger** I_{NaCa} and the **Sodium potassium pump** I_{NaK} currents describe membrane activities mediated by ATP. Their equations depend on all the intercellular concentrations: $[Ca^{2+}]_i, [Na^+]_i, [K^+]_o$.

The **Non-specific calcium-activated current** I_{nsCa} describes the activity of a channel

equally permeable to Na^+ and K^+, under Ca^{2+} overload conditions. Therefore, I_{nsCa} is regarded as the sum of the Na^+ current I_{nsNa} and the K^+ current I_{nsK} through this channel.

The **Sarcolemmal calcium pump** I_{pCa} provides the behaviour of this other mechanism, in addiction to the exchanger I_{NaCa}, for the extrusion of calcium ions out of the cell. As suggested, the pump is included in the model to maintain the low level of $[Ca^{2+}]_i$ at rest.

The **Calcium background current** I_{bCa} is formulated as a linear leakage current, whose resting potential depends on calcium concentrations.

The **Sodium background current** I_{bNa} is also formulated as a linear leakage current. Its contribution to $[Na^+]_i$ is balanced by Na^+ ion extrusion through I_{NaK} and entry through I_{NaCa}, so that the resting level of $[Na^+]_i$ is maintained, see [63].

Concentrations dynamics   The evolutions of the intercellular concentrations of the sodium and potassium can be described by simple ODEs. In the formulation, we'll consider not only the total ion current through all the ion channels, but also the currents through pumps and exchangers. Thus, we have:

$$\frac{d[K^+]_i}{dt} = -\frac{A_{cap}}{V_{myo}F}\left(I_K + I_{K1} + I_{Kp} - 2I_{NaK}\right)$$

$$\frac{d[Na^+]_i}{dt} = -\frac{A_{cap}}{V_{myo}F}\left(I_{Na} + I_{bNa} + 3I_{NaK} + 3I_{NaCa}\right),$$

where A_{cap} is the capacitative area of the membrane and V_{myo} is the volume of the myoplasm.

According to the previous presentation, the SR is represented by two subcompartements, employed for the buffering of calcium ions. The intracellular calcium mechanisms are governed by four currents:

I_{up} represents the inward calcium current from the cytoplasm to NSR, through a pump mechanism;

I_{leak} is the outward calcium current from NSR back to cytoplasm

I_{tr} stands for the calcium current between NSR and JSR

I_{rel} is the outward calcium current that releases calcium to the cytoplasm from JSR.

To sum up, the model considers the three different concentrations of the free calcium in the cytoplasm, $[Ca^{2+}]_i$, in the JSR, $[Ca^{2+}]_{jsr}$, and in the NSR, $[Ca^{2+}]_{nsr}$. Using the notation $I_{Ca,t} = I_{CaL} + I_{nsCa} + I_{pCa} + I_{bCa}$, their evolutions are described by the following ODEs:

$$\frac{d[Ca^{2+}]_i}{dt} = -\beta_{myo}\left(\frac{A_{cap}}{2V_{myo}F}\left(I_{Ca,t} - 2I_{NaCa}\right) + \frac{V_{nsr}}{V_{myo}}\left(I_{up} - I_{leak}\right) - \frac{V_{jsr}}{V_{myo}}I_{rel}\right),$$

$$\frac{d[Ca^{2+}]_{jsr}}{dt} = -\beta_{myo}\left(I_{tr} - I_{rel}\right) \qquad \frac{d[Ca^{2+}]_{nsr}}{dt} = -I_{up} - I_{leak} - \frac{V_{jsr}}{V_{nsr}}I_{tr},$$

where β_{myo} and β_{jsr} model instantaneous calcium buffering, [64].

1.3.3 Ten Tusscher and O'Hara-Rudy models

The most studied models of human ventricular cells are Ten Tusscher-Panfilov (TT) model (published in 2004 and updated in 2006) and O'Hara-Rudy (ORd) one (published in 2011). Differently from all the previous models, they present a high level of electrophysiological detail, and they are based on human experimental data of the major ionic currents, [131].

TT model presents I_{ion} as the sum of 12 transmembrane ionic currents (see Figure 1.11), thus

$$I_{ion} = I_{Na} + I_{CaL} + I_{to} + I_{Kr} + I_{Ks} + I_{K1} + I_{NaCa} + I_{NaK} + I_{pCa} + I_{bK} + I_{bCa} + I_{bNa}.$$

The **sodium current** (I_{Na}) is the sum of Fast Na^+ current and Late Na^+ current, with identical activation time constant. These currents can't be considered to be separated channels, but they represent different gating models, separated functionally in time.

The **L-Type Calcium current** (I_{CaL}) has the same formulation as previous models.

Potassium currents are divided into *Slow delayed rectifier current* (I_{Ks}), *Inward rectifier* K^+ *current* (I_{K1}) and *Rapid delayed rectifier current* (I_{Kr}), with terms representing the outward potassium concentration dependence.

The **transient outward current** has the following simple formulation:

$$I_{to} = g_{to}rs(V - E_K)$$

where r is the voltage dependent activation gate and s is the voltage dependent inactivation gate.

The **Sodium-calcium exchanger** I_{NaCa} and the **Sodium potassium ATPase pump** I_{NaK} currents have the same formulation of Luo Rudy models, except for a factor that accounts for the higher concentration of calcium in the subspace close to the sarcolemmal membrane where the exchanger is operating.

The **Sarcolemmal calcium pump** I_{pCa} has the commonly applied equation, similar to the equation used in Luo Rudy models.

The **Background currents** I_{bCa}, I_{bNa}, I_{bK} with reduced amplitudes, so that the generally lower major current conductances used to match human data in construction of this model would be properly balanced.

The dynamic of the main ions (sodium, potassium and calcium) is not affected by many changes. Potassium and sodium concentrations are governed by the following system:

$$\frac{d[Na^+]_i}{dt} = -\frac{I_{Na} + I_{bNa} + 3I_{NaK} + 3I_{NaCa}}{V_C F}$$

$$\frac{d[K^+]_i}{dt} = -\frac{I_{K1} + I_{to} + I_{Kr} + I_{Ks} - 2I_{NaK} + I_{bK} + I_{stim}}{V_C F}.$$

where I_{stim} stands for the external stimulus current.

In the same way, calcium concentrations can be divided into two different parts, that are the total calcium in the cytoplasm, accounting buffered and free calcium in the cytoplasm, and the total calcium in the SR, accounting the buffered and the free calcium in the SR.

Exactly like the previous model of Luo and Rudy, these concentrations are formulated in the following way, [79]:

- the leakage current from the SR to the cytoplasm

$$I_{leak} = V_{leak} \cdot (Ca_{SR} - Ca_i);$$

- the pump current taking up calcium in the SR

$$I_{up} = \frac{V_{maxup}}{1 + \frac{K_{up}^2}{Ca_i^2}}$$

- the calcium induced calcium release current, depending on the activation and inactivation gating variables g and d,

$$I_{rel} = K_{rel} \cdot \left(c_{rel} + \frac{a_{rel} \cdot Ca_{SR}^2}{b_{rel}^2 + Ca_{SR}^2} \right) \cdot d \cdot g \qquad (1.18)$$

where $V_{maxup}, V_{leak}, K_{up}$ are specific parameters.

What really represents an improvement in the direction of simulating human cardiomyocytes is the possibility to reproduce human epicardial, endocardial, and M cells action potentials. Histologically, M cells are similar to epicardial and endocardial cells. Electrophysiologically and pharmacologically, they appear to be a hybrid between Purkinje and ventricular cells, [3].

It is possible to switch from one type to the other by changing a little set of parameters.
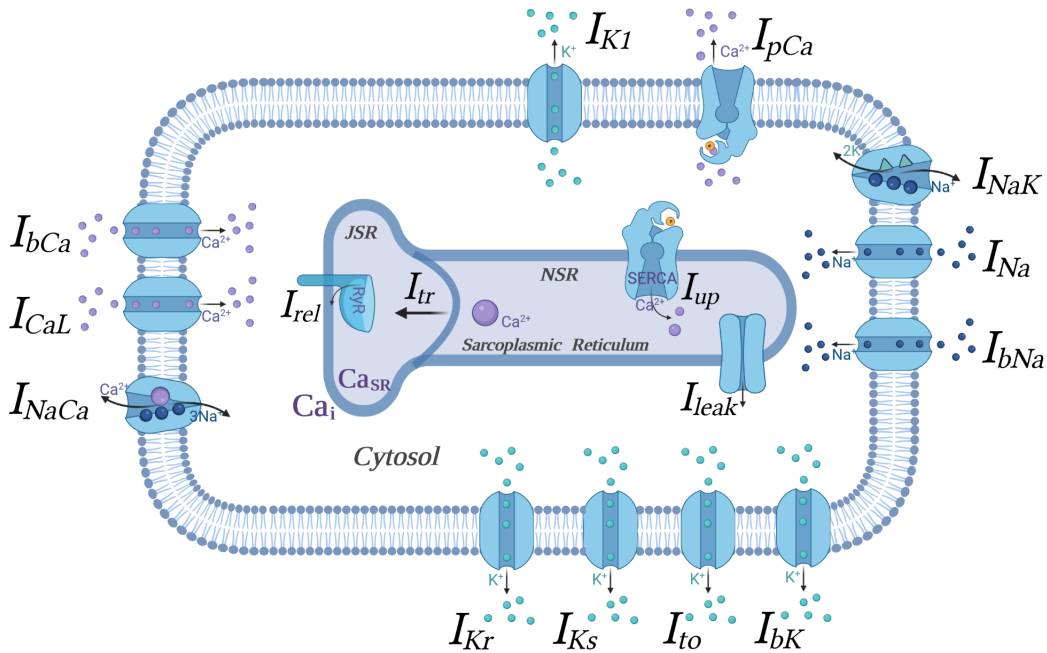

Figure 1.11: Schematic diagram of the currents considered in Ten Tusscher model.

Through the model we are also able to explain differences between cells behaviours. For example, endocardial cells differ from epicardial cells in their lower I_{to} density and in their slower recovery from inactivation. Furthermore, M cells differ from epicardial and endocardial cells by having a different I_{Ks} density, while I_{to} density and dynamics are similar to those of epicardial cells. Like Purkinje fibers, M cells develop delayed afterdepolarizations more readily in response to agents that calcium load or overload the cardiac cell. Thus, they may contribute to the development of both substrate and triggers associated with arrhythmogenesis. Finally, the model shows a longer AP duration of M cells because of the lower I_{to} density, see [130].

O'Hara-Rudy model The main currents formulation and the histological differences among cells (transmural heterogeneity) are preserved also in the O'Hara-Rudy model. The main difference consists in a specific cell structure, that includes four compartments: the bulk myoplasm (myo), the subspace (SS) representing the space near the T-tubules, the JSR and the NSR.

As a consequence, the whole Na^+/Ca^{2+} exchange current I_{NaCa} is split into two contributions: the 80% of the total amount concurs to the myoplasm ionic flux ($I_{NaCa,i}$), the residual 20% results as a current into subspace ($I_{NaCa,ss}$).

Furthermore, within these compartments are placed ionic currents and fluxes described by Hodgkin-Huxley equations or Markov models and some additional currents are responsible of the ion flux between the myoplasm and the subspace. These diffusion currents a $I_{diff,Na}$, $I_{diff,Ca}$ and $I_{diff,K}$.

Similarly, the L-type calcium current (I_{CaL}) is defined as the sum of two components, namely I_{CaK} and I_{CaNa}.

This model is of great importance for the modern cardiac electrophysiology. Several human models have been proposed for ventricular electrophysiology, and among them the ORd model stands out among the others because of the representation of Calcium signalling, the capability to manifest arrhythmia precursors such as alternans and early afterdepolarisation, and good response to simulated drug block and disease remodelling.

Figure 1.12: Official $Life^X$ logo, [1]

A novel update of this milestone was developed in 2019 as the ToR-ORd model and this new formulation is provided in the $Life^X$ library, [126].

Nevertheless, ORd was selected by a panel of experts as the model best suited for regulatory purposes. Thus, we developed a C++ code for the ORd model, embedded in the $Life^X$ library (Figure 1.12), this one being a high-performance Finite Element library mainly focused on mathematical models and numerical methods for cardiac applications, [1].
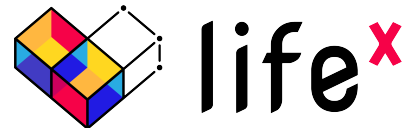
Chapter 2

Human Induced Pluripotent Stem Cells (hiPSC)

Every organ and tissue in our body has stem cells as foundation cells. Indeed, these tissues are made up of highly specialized cells, originally coming from an initial pool of stem cells formed shortly after fertilization. Throughout our lives, we continue to lean on stem cells in order to replace injured tissues and cells that we lose every day, i.e. those in our skin, hair, blood, and the lining of our gut. Stem cells are characterized by two key properties: (i) the ability to self-renew, dividing in a way that makes copies of themselves, and (ii) the ability to differentiate, giving rise to the mature types of cells that form our organs and tissues.

Induced pluripotent stem cells (also known as iPSCs) are a kind of pluripotent stem cells that can be generated directly from adult cells (e.g., skin cells). These cells exhibit morphology and growth properties typical of embryonic stem cells and express the same marker genes, see [122]. IPSCs hold promise in the field of regenerative medicine, thanks to their ability to propagate indefinitely and to give rise to every other cell type in the body. Human embryonic stem cells might be used in disease treatment, but problems arise because of ethical troubles and tissue rejection following in vivo transplantation. IPSCs allow circumventing these issues since they can be derived directly from adult tissues, [114].

In many fields, the primary challenge is to use iPSCs to replace those lost due to damage or disease processes. Although the iPSC technology has not yet advanced to a stage where therapeutic transplants have been deemed safe, iPSCs are readily used in drug discovery and to understand the patient-specific basis of disease. This means they are used for drug screening, especially in efficacy and potential toxicity investigations.

Such approaches are now becoming more and more popular because of the increasing interest in phenotypic screening and the advantages of human iPSCs in disease modeling compared to traditional screenings, see [114].

2.1   A decade of progress

The iPSC technology was pioneered by S. Yamanaka, who was awarded the Nobel Prize in 2012, along with Sir J. Gordon, for the discovery of mature cells reprogrammed to become pluripotent.

The first step was fulfilled in 2006 by Yamanaka ad K. Takahashi. In their study, they showed that cells with a gene expression profile similar to the embryonic stem cells can be generated from mouse somatic cells by using retroviral transduction of four transcription factors: Oct3/4, Sox2, Klf4, and c-Myc, [122].

To reach this conclusion, they assumed that genes important to embryonic stem cells functions might play pivotal roles in somatic cell pluripotency induction. First of all, they selected 24 genes as candidates and introduced each of them into mouse embryonic fibroblasts (connective tissue cells), obtaining a resistant colony. After that, in order to determine which of them were critical, they sequentially examined the effect of withdrawal of individual factors from the pool of transduced candidate genes on the formation of resistant colonies, see 2.1.

Through different data analyses on their experiments, authors also confirmed the statement that iPSCs are similar, but not identical, to embryonic stem cells, [17].

Just one year later, three separate research groups improved the reprogramming approach, giving rise to iPSCs that were indistinguishable from embryonic ones (in morphology, proliferation and gene expression). Anyway, this improvement did not change the main assumption and pluripotent stem cells were derived by retroviral-mediated expression of the same four transcription factors, [81]. A schematic view of the generation process is presented in Figure 2.1.
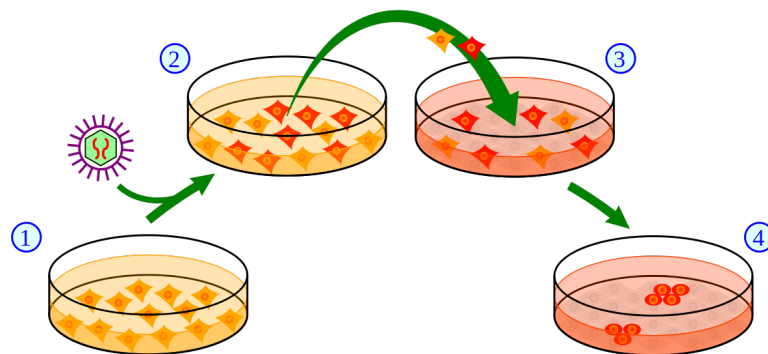
Figure 2.1: Schematic process on the generation of iPSCs. (1) Culture donor cells (2) Transduce stem cell-associated genes into the cell by viral vectors. (3) Culture of cells, according to stem protocols. (4) A small subset of these cells generate iPSCs colonies.

Once again Yamanaka research group, in 2007, was the first to derive human induced pluripotent stem cells (hiPSCs). With the same principle used in mice reprogramming, researchers used the same four pivotal genes to transform human fibroblasts, using a retroviral system. The fundamental transcriptional network governing pluripotency is common in humans and mice, but extrinsic factors and signals maintaining pluripotency are unique for each species. Thus hiPSC are not identical to human embryonic cells: differences between the two lines can be detected

through DNA microarray analyses.

Fibroblasts can be obtained by a skin biopsy, thus different efforts were done in order to identify cell types that are more easily accessible, see [123].

2.1.1 Differentiation of hiPSCs

Tissue-specific stem cells, which are often identified as "adult" or "somatic" stem cells, are already somewhat specialized and they are able to reproduce almost every mature cell that you can find in the same tissue or organ in which they reside, also if considering different mature cell types. Because of their ability to generate multiple, organ-specific, cell types, they are described as "multipotent." For example, if we consider stem cells lying in the adult brain we notice that they can make neurons and two types of glial cells, astrocytes and oligodendrocytes. Tissue-specific stem cells are highly present in different organs that need to be continuously filled themselves, such as the blood, skin and gut, even though they have even been found also in less regenerative organs, like the brain. These types of stem cells represent a very small population and are often hide deep

Figure 2.2: Schematic view of the differentiation process from skin cells to differentiated hiPSCs

in the tissue, giving as a result a hard identification, and difficulties in isolating and growing in a laboratory setting, see Figure 2.2.

Unlike adult stem cells (tissue-specific), embryonic stem cells potentially could generate every cell type found in the body. Furthermore, the importance of these cells is the possibility to grow and expand indefinitely, under the right conditions, in this unspecialized and undifferentiated state. This is the reason why these cells play a key role in learning about early human developmental processes, otherwise inaccessible. Furthermore, they help researchers to study diseases and define strategies that ultimately could lead to therapies designed to replace or restore damaged tissues.

2.1.2 Disease modeling

Induced pluripotent stem (iPS) cells technology became popular also in regenerative medicine and the first clinical study started in 2014. The challenge is to identify pathological mechanisms underlying human diseases, in order to discover new therapeutic strategies.

One of the main reason why researchers are interested in studying iPS cells, and one of the major advantages, is that they represent a good way to create pluripotent stem cell lines, that are specific to a disease or even to an individual patient. The development of disease-specific stem
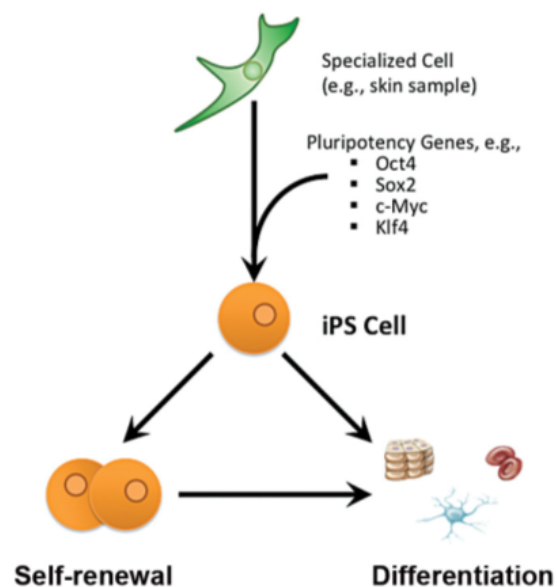
cells is a very attractive tool for studying the the mechanisms underlying a particular disease and then for testing drugs for their treatment. One of the major advantages of patient-specific stem cells in the field of cell therapy is that these cell lines arising from the patient themselves may minimize different serious complications and rejection risks, besides immunosuppression that can occur following.

In the case of a genetic disease, the specific disease modeling begins with the process of deriving hiPSCs containing the mutation with a key role in the disease. The second step is to differentiate them into disease-relevant cell types (see Figure 2.3). The resultant cells are then used to reveal disease aetiology, even though iPSCs exhibit line-to-line variations, which makes data interpretation a little bit harder.

Moreover, because of pluripotency, it's possible to differentiate into cells otherwise hard to access, such as neurons.

Cell therapies based on iPSCs collapse because of several obstacles concerning the risk of tumorigenicity. Dismissed the clinical application using cell products, the main clinical use of iPSCs is about drug discovery.

The first scope is about screening for efficacy: the aim is to find out the target considered to be significant for the disease. Specifically, potential drug candidates have been identified using either phenotypic and target-based screening. Only cells differentiated front the patient-derived iPSCs could present molecular and cellular phenotypes. Whether the phenotype that is selected as a readout for a drug screen is truly relevant to the disease can be confirmed by a gene editing approach if the gene responsible for the disease phenotype is known and can be validated.

Another application is in drug repositioning, in which existing drugs already approved for specific diseases are tested to find new applications in other diseases, see Figure 2.3.

The second scope is about screening for toxicity. The development of new drugs is highly expensive, because of failures occurring in late-stage clinical trials. Many unpredicted adverse effects can occur especially because of cardiac and liver toxicity.

Various preclinical strategies have been proposed to detect drug-induced electrophysiological cardiotoxicity, including using *in-vitro* human ion channel assays, human-based *in-silico* reconstructions and human stem cell-derived cardiomyocytes, [114].

Current therapies Nowadays, the most frequently used stem cells for therapy are blood stem cells. In the past, doctors usually used bone marrow transplants to transfer blood stem cells to patients, while currently more advanced techniques for collecting blood stem cells are used to treat leukemia, lymphoma and other blood diseases. The most popular alternative to bone marrow transplantation is the umbilical cord blood collection, and preserved as a source of blood stem cells. Also some corneal and skin disorders or injuries can be treated by grafting tissues that are maintained or derived by stem cells, and different studies show that these therapies are safe and effective.

Potential therapies Other promising stem cell treatments are still at very early experimental stages. Mesenchymal stem cells, for example, randomly located throughout the whole body
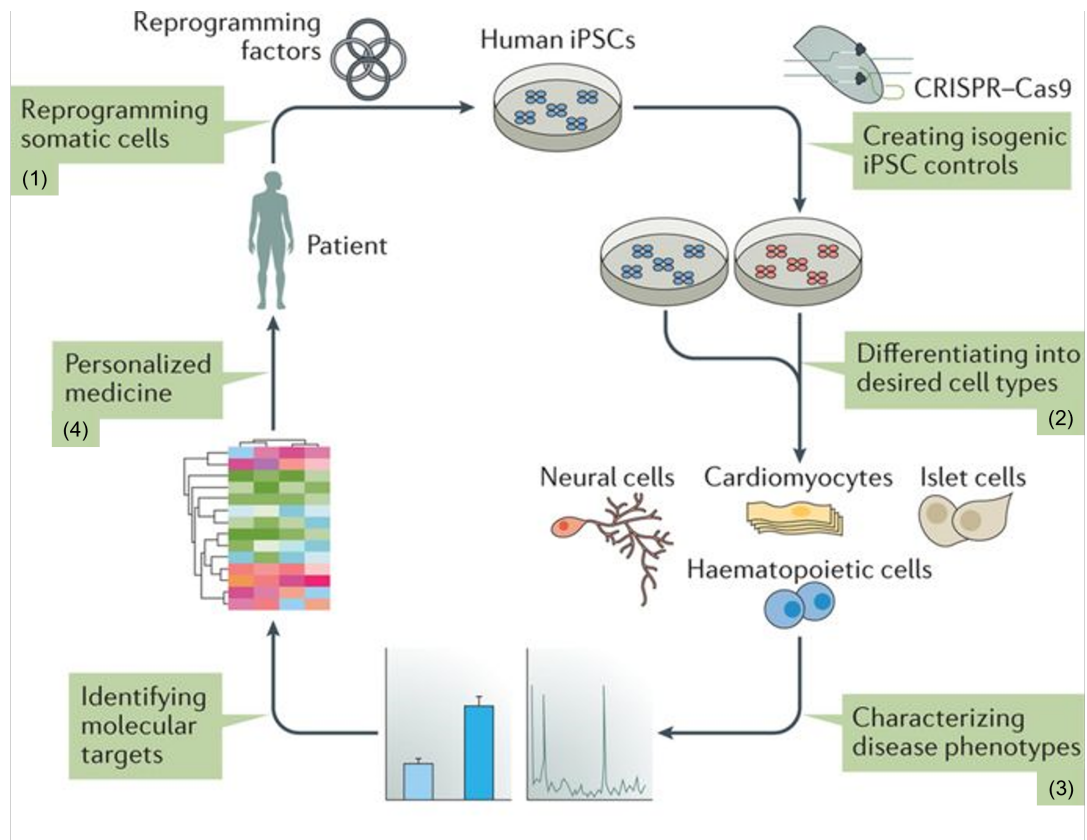
Figure 2.3: Typical steps of the creation and use of hiPSCs-based disease models: starting from the patient, (1) hiPSC can be derived using the reprogramming protocol; (2) a differentiation process allows to deal with with hiPSC-CMs; (3) different diseases can be characterized and modeled and finally (4) patient specific therapies feed the personalized medicine field.

(including in the bone marrow), can be treated and driven to become bone, cartilage, fat and maybe even muscle. In different experimental setup, mesenchymal stem cells showed the ability to modify immune functions, generating considerable interest in developing ways of using these cells to treat a high percentage of musculoskeletal abnormalities, cardiac disease and some immune disorders.

Remaining challenges Despite the successes we have seen so far, we summarize some of the major challenges that should be solved in order to use stem cells as a cell therapy to treat a wider range of diseases. Initially, the source of stem cell should be enlarged. The process actually needed to identify, isolate and grow the desired kind of stem cell, especially when rare adult cells are needed, is painstaking and difficult. On the other hand, embryonic stem cells and generic pluripotent stem cells, can be grown indefinitely in laboratories, with the advantage of having the potential to differentiate in any cell in the body, but such processes are already very complex and require to be tightly controlled. iPS cells are also limited by these concerns. In both cases, different challenges should be won to ensure that these cells can be isolated and used safely and routinely. Furthermore, the match between the donor and the recipient tissue needs a very close

match, as it happens with organ transplants: the more closely the tissue matches the recipient, the lower the risk of rejection. The development of iPSCs opened the door to the expansion of patient-specific pluripotent stem cell lines that can later be developed into a needed cell type showing lower problems of rejection and immunosuppression occurring from unrelated donors transplants. Finally, a specific system for allocating the cells to the expected part of the body should be developed. Once in the right organ, the new cells should then be forced to integrate and cooperate together with the other existing cells of the body.

2.2　hiPSCs-Derived Cardiomyocytes (hiPSC-CMs)

The purpose of this work, anyway, is to model one of the three possible germ layers of hiPSCs, thus we will focus on the ability to establish specific differentiation toward the cardiac lineage. That is why it is important to characterize the cardiomyocyte differentiation potential of hiPSCs, to define the developmental steps involved in this process, and to study the molecular, structural, and functional properties of the generated hiPSCs–CMs.

Differentiation to cardiac lineage relies on many signaling pathways. The most important pathways are based on inducers and inhibitors of cardiac specification, [144].

hiPS-CMs are spontaneously beating cardiomyocytes derived from human induced pluripotent stem cells. The cells express the major cardiac markers and ion channels, they are functionally similar to adult human CMs, and exhibit expected responses to cardiac stimuli, making them excellent *in-vitro* tools for studying human CMs function and for cardiac safety pharmacology assays.

If we base on AP properties, cardiomyocytes' cultures deriving from a single clone of differentiating hiPSCs frequently results in a mix of cells that can be classified as atrial-, ventricular- and nodal-like CMs. However, this kind of classification may result in misleading interpretation when comparing CMs with prolonged action potential duration to healthy ones, [59].

2.2.1　Maturation process

Although several studies have shown that iPSC-CMs have molecular, structural and functional properties resembling those of adult cardiomyocytes, they have proved to be less mature than adult cells.

This means that information about electrophysiological and biochemical properties are limited.

The matter concerns iPSCs in general, because technologies for reprogramming cells evolved much more rapidly than our ability to control the maturation state and age of resulting derived cells. The general agreement is that human derived cells exhibit the properties of fetal-stage cells, and these properties are observed in hiPSCs lineages independently of initial somatic donor cell's age. The long-term goal is to re-program different cellular age and thereby to create specific cell types of any age, [40].

To sum up, the main process involved in this issue is the maturation. They represent contiguous temporal stages, but specific cellular processes underlying these mechanisms are
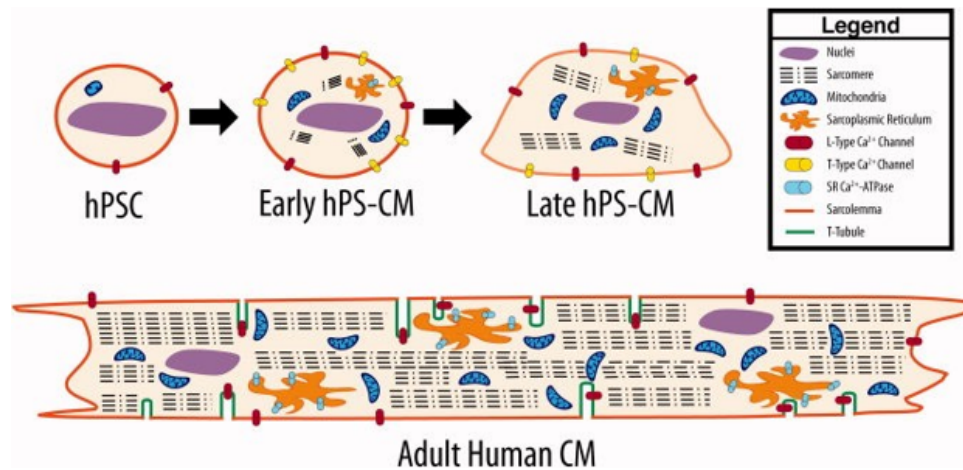
Figure 2.4: Visual comparison of hiPSC-CMs and human adult CMs morphology. Late hiPSC-CMs differ from human adult CMs, e.g., in shape, size and ion channel expressions. Adult CM are far larger, with multiple nuclei, large sarcomeric area, and large numbers of mitochondria. Figure credit [100]

highly different: cell maturation involves the development of functional features (such as electrical activity), while aging is associated with a gradual decline in structures and functions.

The most common strategy to induce aging in cell differentiated from human pluripotent ones is to treat these cells with cellular stressors. Another way is to express ectopical gene products that induce premature aging.

However, whether these methods can elicit cellular ageing through a normal ageing mechanism remains to be determined, [120].

Cardiomyocytes' maturation It's a general agreement that hiPSC-CMs are immature as they do not display the sub-cellular, cellular and tissue-level adult myocyte morphology and sarcomeric protein content and organization. A visual comparison of hiPSC-CMs and human adult CMs morphology is detailed depicted in Figure 2.4 .

The culture process lasts almost one month: after around 16 days in the culture, cells begin to segregate and by 30 days become subtype in specific ventricular or atrial cells.

Maturation of hiPSC-CMs is needed because it underlies the required physiological functions of the cell. That is why it is important to develop limited quantitative methods to track hiPSC-CMs maturation. One of the great challenges of an effective maturation marker rests in its reliability as an adult marker. In fact, many potential cardiac markers of the adult mature state are too susceptible to changes and the can revert in other signals during stress, [12].

Compared to their early-stage counterparts, late-stage hiPSC-CMs showed dramatic differences in specialized structures.

Considering the morphology, we noticed that the most important parameter of myocytes' function is their force production, as it determines how effectively the organ can circulate blood. An adult myocyte seems to have well-organized sarcomeres and rectangular shape, while, in comparison, the morphology of a stem cell-derived myocyte presents some distinct challenges.
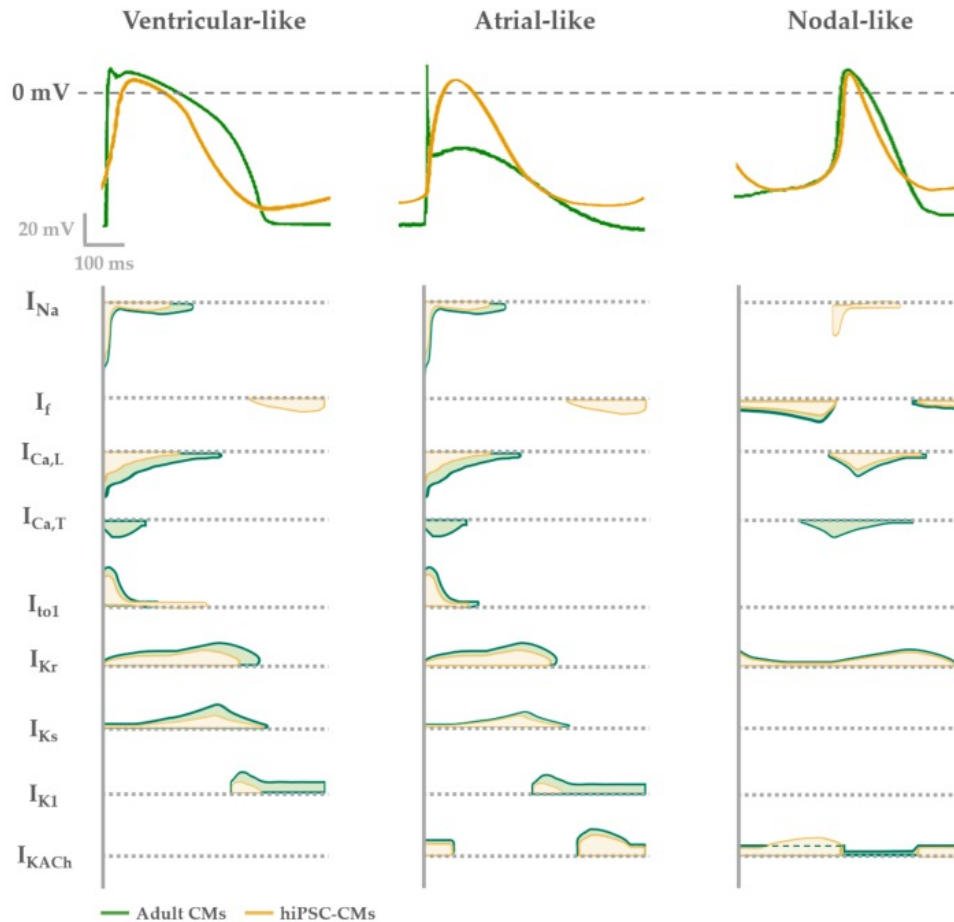
Figure 2.5: AP shape of different phenotypes, determined as the balance between inward and outward currents. The typical adult CM APs (green) is compared to hiPSC-CMs one (yellow). Figure credit [59].

Adults myocytes also show greater myofibril density and alignment.[140]

Functional properties of hiPSC-CMs also highlight the level of electrical and mechanical cell maturation. In order to characterize electrophysiological properties of the differentiation, different ionic currents have been recorded in single hiPSC-CMs by using the patch clamp technique. Figure 2.5 presents the contribution of the Sodium and Calcium inward currents to the depolarizing phase of the electrical activity, while the repolarizing process is governed by the outward Potassium current. Additionally, the Calcium inward component and the pacemaker current play a key role during the slower depolarization of spontaneous automatic cells and during the plateau phase in simulated phase. The comparison between the electrophysiological phenotypes of hiPSC-CMs and adult CMs suggests a great correspondence when considering nodal-like and sinoatrial CMs, because of the contribution of the funny current and and Calcium currents, together with the overlack of I_{K1}. On the other hand, if we consider atrial and ventricular APs, major differences between adult and hiPSC-CMs AP shapes are present. Indeed, hiPSC-CMs features, such as the Diastolic Membrane Potential, the AP upstroke velocity and the AP duration, are not superimposable to those of adult CMs, [59].

2.3 Engineered hiPSC-CMs tissue

The possibility to engineer hiPSC-derived cardiac cell cultures being as similar as possible to undiseased and diseased regions of the human heart is the required to improve the translation of hiPSC-CMs studies to humans.

In the area of cardiovascular diseases, hiPSC-CMs have already shown a wide range of possible applications; important parameters like morphology, calcium handling, and contractility have been successfully analyzed in such systems. 2D cultures of hiPSC-CMs are often used as a platform for investigating new therapies. Despite the improved maturation protocols developed in the last few years, hiPSC-CMs in 2D cultures are placed in a physiological and structural context that does not completely mimic the in vivo condition.

In an effort to overcome the intrinsic limitations 2D cell cultures in terms of spatial architecture, recent years have seen a burgeoning development of three-dimensional culture models.

However, re-creating *in-vitro* a reliable 3D tissue is undoubtedly more complex than using standard cell cultures, and several new aspects have to be considered simultaneously. Besides the source of cardiomyocytes, which has been discussed so far, at least three more elements must be considered for the creation of a 3D heart tissue model (see Figure 2.6): the type of supporting scaffold, when present, the external stimuli that need to be applied and, last but not least, the role played by the non-contractile cell population(s).

Such phenomenon has also involved the field of heart diseases and many groups have developed
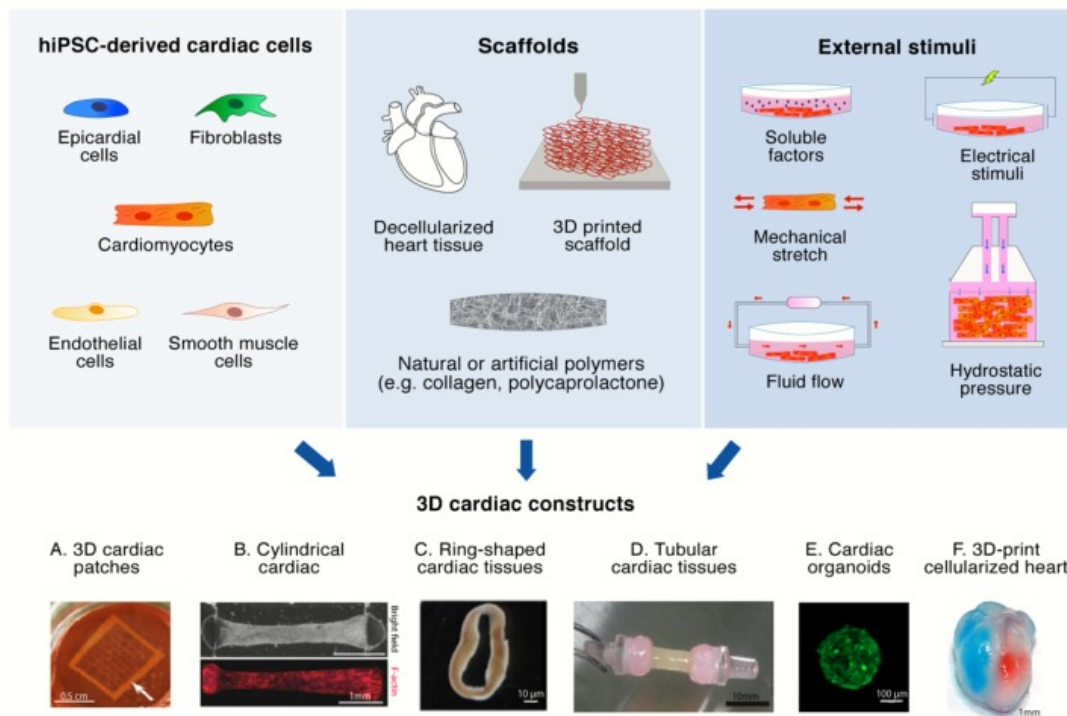

Figure 2.6: Generation of three-dimensional hiPSC-based cardiac constructs. Human iPSC-derived cardiac cells, scaffolds, and physical and environmental stimuli are the three main elements required for the generation of a 3D cardiac construct. Figure credit [105]

3D models of both healthy and pathological cardiac tissues [105].

The availability of human embryonic stem cells and the scalability of their directed differentiation into bona fide cardiomyocytes, as well,have facilitated the rapid evolution of myocardial tissue engineering.

For example, some researchers systematically approached the design of engineered human myocardium with structural and functional properties observed in the postnatal heart (Figure 2.7). Through overstimulation, they showed that the engineered human myocardium is a useful tool for the modeling of human heart failure in the dish, presenting outcomes similar to what is typically observed in clinical heart failure, [125].

Figure 2.7: The resulting ring-shaped engineered human myocardium, figure credit [125]

Another group developed a next-generation *in-vitro* biomimetic model of pumping human heart chamber, and demonstrated its capability for pharmaceutical testing. From human pluripotent stem cell-derived ventricular cardiomyocytes embedded in collagen-based extracellular matrix hydrogel, we engineered a three-dimensional electro-mechanically coupled, fluid-ejecting miniature human ventricle-like cardiac organoid chamber.

We will focus later on similar results. Harvard University researchers have bioengineered a three-dimensional model of a human left heart ventricle (Figure 2.8) that could be used to study diseases, test drugs and develop patient-specific treatments for heart conditions such as arrhythmia.

The tissue is engineered with a nanofiber scaffold seeded with human heart cells. The scaffold acts like a 3D template, guiding the cells and their assembly into ventricle chambers that beat *in-vitro*. This allows researchers to study heart function using many of the same tools used in the clinic, including pressure-volume loops and ultrasound. The long-term objective of this project is to replace or supplement animal models with human models and especially patient-specific human models: in the future, patient stem cells could be collected and used to build tissue models that replicate some of the features of their whole organ.
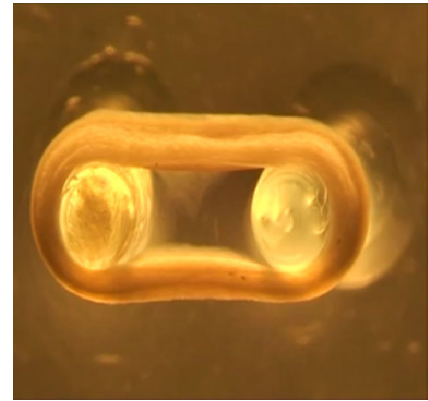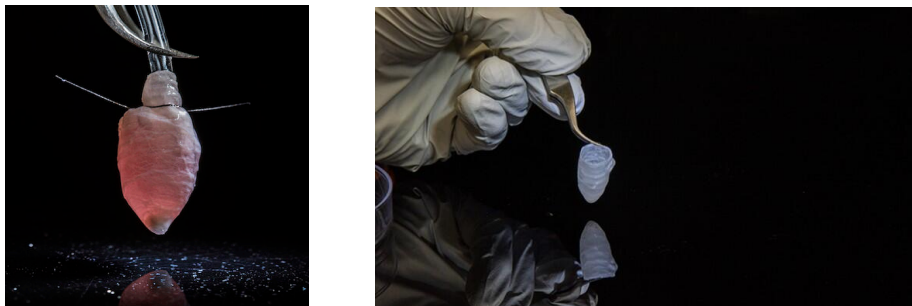

Figure 2.8: Three-dimensional model of a heart ventricle engineered with a nanofiber scaffold seeded with heart cells

Chapter 3

Computational modeling of hiPSC-Derived Cardiomyocyte (hiPSC-CM)

Recently, stem cell-derived cardiomyocytes appeared as a new promising *in-vitro* model, showing some significant differences with respect to adult myocytes, as presented in the previous chapter. This is the reason why models of adult cardiac AP inadequately describe the hiPSC-CM electrophysiology: differences between hiPSC-CM and adult myocyte action potentials require a new mathematical approach to hiPSC-CMs.

To fill this gap, some specific computational methods have been developed in the last decade. The forerunner was Michelangelo Paci, who developed a primal model in 2013, [85], creating a new line improved in 2018 and 2020. Some other models have been published in the last few years by Koivumäki in 2018, [50], and Kernik in 2019, [45].
Both the Paci generation and the others single models focus on the ventricular-like phenotype, one of the different cellular phenotypes emerging during the differentiation process. Among them it is possible to deduce a new primitive model from the Paci2013, atrial-like specific.

The conventional starting point is a modified version of previous human adult CM models: both ventricular-like and atrial-like models follow the classical second generation formulation, which describes the membrane potential with the generalized Cauchy problem in 1.17.
Each of the previous models is characterized by a different I_{ion} formulation, sometimes accompanied by alternative concentrations evolutions or equipped by an improved calcium dynamic formulation.

Considering the evolution in time, described by ordinary differential equations, for generic initial conditions, the system always reaches the steady state after 800 seconds.
In control condition, ventricular-like AP was simulated for each model, without external stimulation, thus $I_{stim} = 0$. Although the variety of methodologies and the ion channel expressions hidden behind every current, the presented electrophysiological models show a steady state spontaneous activity, characteristic of hiPSC-CMs (Figure 3.1).

The different pedigrees of hiPSC-CMs models are also based on specific experimental data,

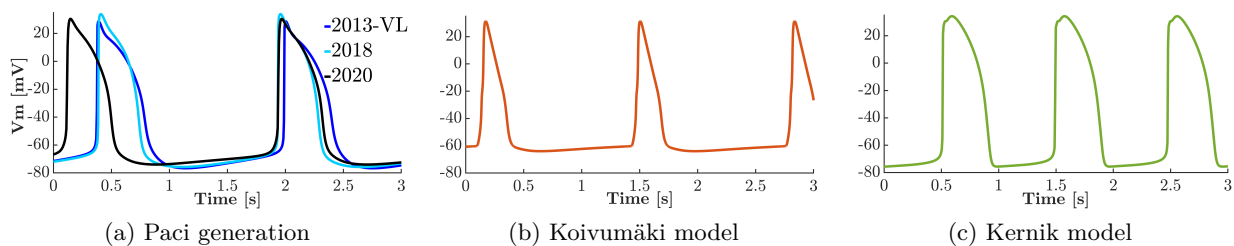(a) Paci generation   (b) Koivumäki model   (c) Kernik model

Figure 3.1: Steady state spontaneous APs described by different formulations for ventricular phenotype

recorded in voltage clamp method on cultured hiPSC-CMs. Parameters' rescaling with a basic fitting of available data was generally found by simulating the protocol used during the experiments, taking into account the phenotypical heterogeneity affecting the recordings obtained from a mixture of different cell lines phenotypes.

Anyway, different experimental data were not available to fit the recorded AP and cytosolic calcium transient traces. For this reason, the optimization algorithm was adapted from the Fabbri et al, purposed in [27]. The algorithm is based on the Nelder-Mead simplex method to find the optimal solution: this algorithm minimizes a non-linear cost function built on weighted quantitative data on AP features. Each biomarker is compared with the experimental data: the overall cost of a particular observed feature is zero if it fells into the experimental mean $\pm$ SD, otherwise it was increased in a linear way.

Specifically, Kernik optimization methodology is divided into several steps, as described in the Flow Chart of Figure 2 in [45]. For each current, a first parameter optimization minimized the error between the model and experimental voltage-dependence of the steady-state and time constants of a given gate. Once every current had been analysed, other maximal conductances and rates were optimized considering the described AP and Calcium Transient morphology markers.

The following AP morphology biomarkers (AP features) were usually measured from the *in-silico* data and were considered to build the cost function:

MDP	maximum (negative) diastolic membrane potential
AP_{peak}	peak potential of the action potential
APA	amplitude of the action potential, computed as the difference in voltage between MDP and the peak voltage during the AP
V_{max}	(or dV/dt_{max}) maximum upstroke velocity, the maximal slope between two points in the computed AP upstroke
APD_{10}	action potential duration at 10% of repolarization
APD_{30}	action potential duration at 30% of repolarization
APD_{90}	action potential duration at 90% of repolarization
CL	cycle length.

Some additional features or derived biomarkers are often defined to evaluate the triangulation of the AP shape. These are, for example:

$$AP_{tri} := \frac{APD_{90} - APD_{30}}{APD_{90}} \qquad \text{action potential triangulation used by Koivumäki}$$

$$rappAPD := \frac{APD_{30} - APD_{40}}{APD_{70} - APD_{90}} \qquad \text{AP shape factor used by Paci as a threshold value to discriminate among ventricular-like and atrial-like hiPSC.}$$

The goal of this chapter is to investigate differences between the existing pedigrees of math-based models. Changes in formulations mainly affect the number of compartments and the ion currents, pumps and exchangers included in different models.

3.1 Paci generation

The first generation we are taking into account is the Paci set of models, firstly developed in 2013. In almost every publication, I_{ion} is the sum of specific ionic currents: for each of them, experimental data were derived by [66], whose laboratory recorded these currents on hiPSC-CMs cultured for $30 - 32$ days using the voltage clamp method.

Different ionic currents will preserve an unaffected formulation, as well as the intercellular Ca^{2+} and Ca_i concentrations:

$$\frac{dCa_i}{dt} = I_{leak} - I_{up} + I_{rel} - \frac{I_{CaL} + I_{bCa} + I_{pCa} - 2I_{NaCa}}{2FV_c} \tag{3.1}$$

$$\frac{dCa_{SR}}{dt} = \frac{V_c}{V_{SR}} \left(I_{up} - I_{rel} - I_{leak} \right) \tag{3.2}$$

where F is the Faraday constant, V_c and V_{SR} the cytoplasmic and SR volume respectively, Ca_{SR} and Ca_i the free and buffered calcium insider cytoplasm and SR.
Intercellular Potassium concentration is unchanged, equal to $K_i = 150mM$ while the equation for the intercellular Na^+ improves between models.

3.1.1 Paci2013

This first publication corresponds to the development of two computational models of the hiPSC-CMs AP, distinguishing between the AL and VL phenotypes, emerging during the cell differentiation process. Differences in models are expressed by specific basic fitting parameters, that were scaled in case of known ratios between them to take into account the heterogeneity affecting the voltage clamp data.

The numerical threshold used to discriminate between AL and VL phenotype is the rappAPD, respectively greater and smaller then the threshold value of 1.5 for the ventricular-like and the atrial-like models. Some other visual differences (see Figure 3.2) can be reproduced, such as higher frequency of firing for the atrial like cells, longer APD and greater APA
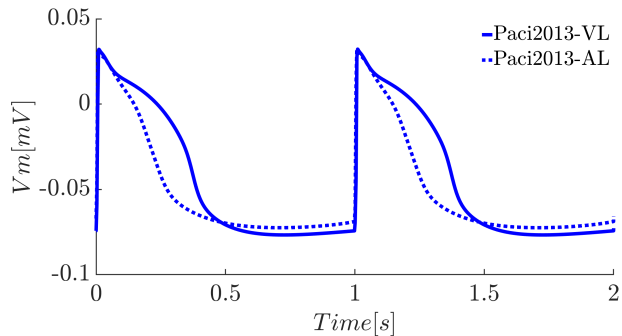

Figure 3.2: Simulated action potential using both AL and VL paced models

and MDP for ventricular like cells. Such differences are the result of little changes in the currents, yielding different ions concentrations. Calcium and sodium dynamics exactly reproduce what physiologically happens to ions concentrations during the action potential phases. Every rapid depolarization, due to the rapid increase of the membrane conductance, is caused by a rapid influx of sodium ions, corresponding to a sudden increase of Na^+ concentration. Upstroke is then followed by a rapid inactivation of sodium channels and a huge Na^+ concentration drop. Intracellular calcium concentration, on the contrary, increases during the plateau phase (see Figure 3.3), buffered by the Sarcoplasmic Reticulum.
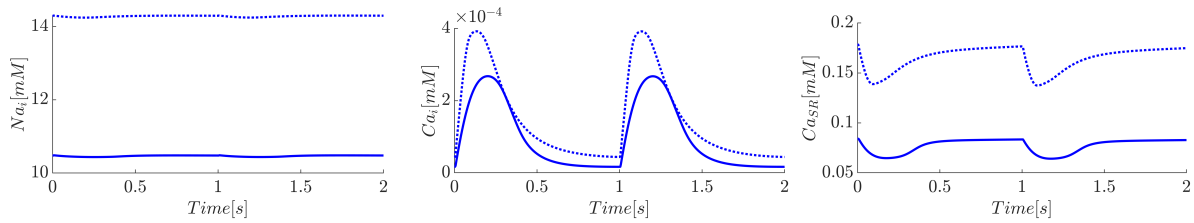
Figure 3.3: Simulated dynamics for both AL (dashed lines) and VL (solid line) paced models. Numerical values of Ca_{SR} and Ca_i underline the key role of Sarcoplasmic Reticulum, which prevent the cell to reach a toxic calcium concentration in the cytoplasm.

Figure 3.4 shows a schematic diagram of the model, depicting the compartmentalization (cytosol and sarcoplasmic reticulum, SR), essential for the calcium handling description. The elementary sodium evolution is written below, as the classical Hodgkin-Huxley formulation, describing the action potential through 12 membrane currents. The shape of these currents is presented in Figure 3.5.

$$\frac{dNa_i}{dt} = -\frac{I_{Na} + I_{bNa} + 3I_{NaK} + 3I_{NaCa}}{FV_c} \tag{3.3}$$

$$\frac{dV_m}{dt} = -I_{Na} - I_{CaL} - I_f - I_{K1} - I_{Ks} - I_{Kr} - I_{to} - I_{NaCa} - I_{NaK} + \tag{3.4}$$
$$- I_{pCa} - I_{bNa} - I_{bCa} + I_{stim};$$

The **Fast sodium current** (I_{Na}) is primarily responsible for the rapid upstroke of the action potential. As in the Hodgkin Huxley formulation, [36], it is modeled by three gating variables (m^3 for activation and $h \cdot j$ for inactivation), but their steady state functions are based on the experimental current-voltage, activation and inactivation curves. Thus

$$I_{Na} = g_{Na} \cdot m^3 \cdot h \cdot j \cdot (V_m - E_{Na}) \tag{3.5}$$

where each gating variable $w \in m, h, j$ satisfies Hodgkin Huxley equation (1.10).

The **L-Type Calcium current** (I_{CaL}) formulation is based on Ten Tusscher [130] and Grandi [33] models, fitting four voltage dependent gating variables, $d, f1, f2, fCa$. The same consideration reported for the identification of sodium currents activation and inactivation curves
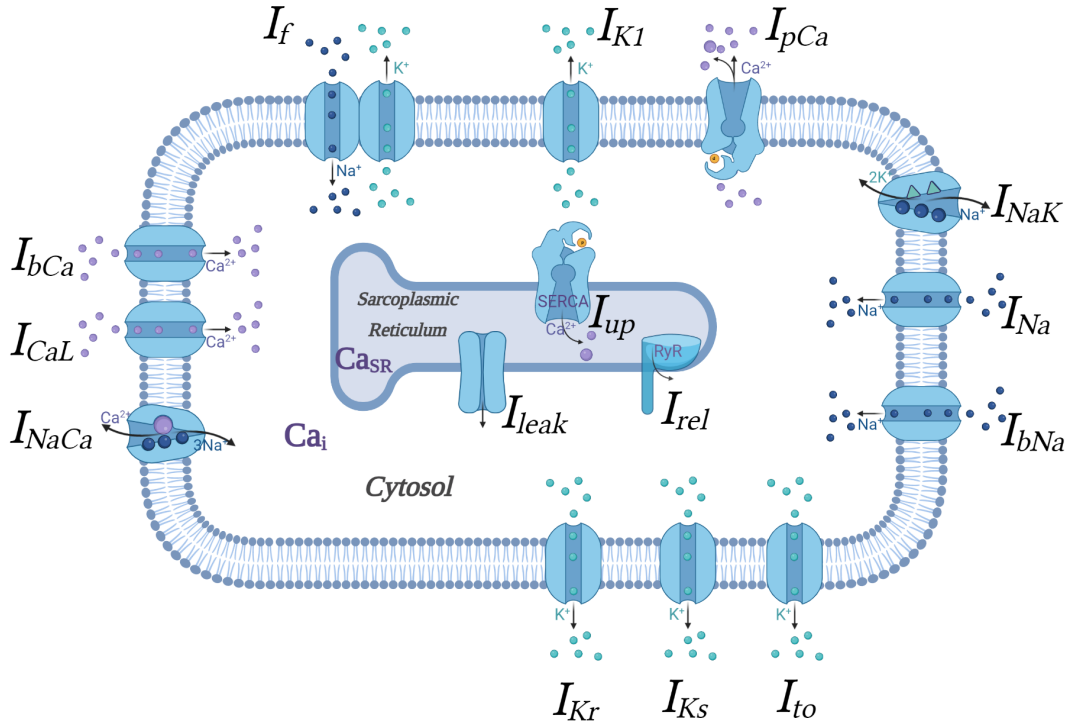
Figure 3.4: Schematic diagram of the model depicting the major functional components. Fluid compartments include cytosol and sarcoplasmic reticulum. Calcium-handling is described by: I_{up} uptaking Ca^{2+} by SR, I_{rel} releasing Ca^{2+} by ryanodine receptors (RyR) and I_{leak}. Sodium, calcium and potassium ions pass the membrane creating 12 different currents through channels, pumps and exchangers, as indicated.

applies here, thus

$$I_{CaL} = \frac{g_{CaL} \cdot 4V_m F^2}{RT} \cdot \frac{\left(Ca_i \cdot e^{\frac{2V_m F}{RT}} - 0.341 \cdot Ca_o\right)}{e^{\frac{2V_F}{RT}} - 1} \cdot d \cdot f1 \cdot f2 \cdot fCa.$$

The **Hyperpolarization-Activated Cyclic Nucleotide-Gated Funny current** (I_f) is activated when the membrane repolarizes and is responsible for starting the diastolic depolarization phase. By this mechanism, the funny current controls the rate of spontaneous activity of myocytes, and thus the cardiac rate. Some unusual features, such as mixed Na^+ and K^+ permeability, activation on hyperpolarization, and very slow kinetics, justify the name. Therefore, the particular kinetic can be described by the equation

$$I_f = g_f \cdot x_f \cdot (V_m - E_f), \tag{3.6}$$

where the gating variable x_f satisfies equation (1.10), with a time constant described by a sigmoidal function of voltage.

The **Transient Outward current** I_{to}, exactly as the **Rapid Delayed Rectifier current** I_{Kr} and the **Slow Delayed Rectifier current** I_{Ks}, conducts outward potassium currents during the plateau phase of action potentials and play a pivotal role in cardiac repolarization.

Their formulations are

$$I_{to} = g_{to} \cdot r \cdot q \cdot (V_m - E_K)$$

$$I_{Kr} = g_{Kr} \cdot \sqrt{\frac{K_o}{5.4}} \cdot x_{r1} \cdot x_{r2} \cdot (V_m - E_K)$$

$$I_{Ks} = g_{Ks} \cdot x_s^2 \cdot \left(1 + \frac{0.6}{1 + \left(\frac{3.8 \cdot 10^{-5}}{Ca_i}\right)^{1.4}}\right) \cdot (V_m - E_K)$$

where the constant $K_o = 5.4 mM$ stands for the potassium concentration out of the cell, and each gating variable $r, q, x_{r1}, x_{r2}, x_s$ follows the Hodgkin-Huxley formalism with voltage depending time constants.

The **Inward Rectifier current** is also a potassium current, related to a specific subset of potassium channels, helping to stabilize the resting membrane potential of the cell. The formula

$$I_{K1} = g_{K1} \cdot x_{K1,\infty} \cdot \sqrt{\frac{K_o}{5.4}} (V_m - E_K)$$

shows that the current involves only the steady state of the gating variable x_{K1}.

The **Sodium Calcium Exchanger current** I_{NaCa} and the **Sodium Potassium Pump current** I_{NaK} where based on previous models for human embrionic stem cells, such as [87]. Their specific formulations are rich of specific constants and depend on both voltage and intercellular sodium concentration.

$$I_{NaCa} = K_{NaCa} \cdot \frac{\exp\left\{\frac{\gamma VF}{RT}\right\} Na_i^3 \cdot Ca_o - \exp\left\{\frac{(\gamma-1)VF}{RT}\right\} \cdot Na_o^3 \cdot Ca_i \cdot \alpha}{(K_{mNai}^3 + Na_o^3)(K_{mCa} + Ca_o)\left(1 + K_{sat} \cdot \exp\left\{\frac{(\gamma-1)VF}{RT}\right\}\right)} \tag{3.7}$$

$$I_{NaK} = p_{NaK} \cdot \frac{\frac{K_o}{K_o + K_{mK}} \cdot \frac{Na_i}{Na_i + K_{mNa}}}{1 + 0.1245 \cdot \exp\left\{\frac{-0.1VF}{RT}\right\} 1 + 0.0353 \cdot \exp\left\{\frac{-VF}{RT}\right\}} \tag{3.8}$$

The **Sarcolemmal Calcium Pump current** I_{pCa} depends only on intracellular calcium concentration and is one of the corrective factors on the model formulation. Other additional corrective currents are **Sodium background current** I_{bNa} and **Calcium background current** I_{bCa}, which preserve a linear current voltage relation. Thus

$$I_{pCa} = g_{pCa} \cdot \frac{Ca_i}{Ca_i + K_{pCa}} \tag{3.9}$$

$$I_{bNa} = g_{bNa} \cdot (V_m - E_{Na}) \tag{3.10}$$

$$I_{bCa} = g_{bCa} \cdot (V_m - E_{Ca}) \tag{3.11}$$

where constant values (K_{pCa} and maximal conductances) were chosen to assure stable intracellular an SR concentrations for Na^+ and Ca^{2+}.
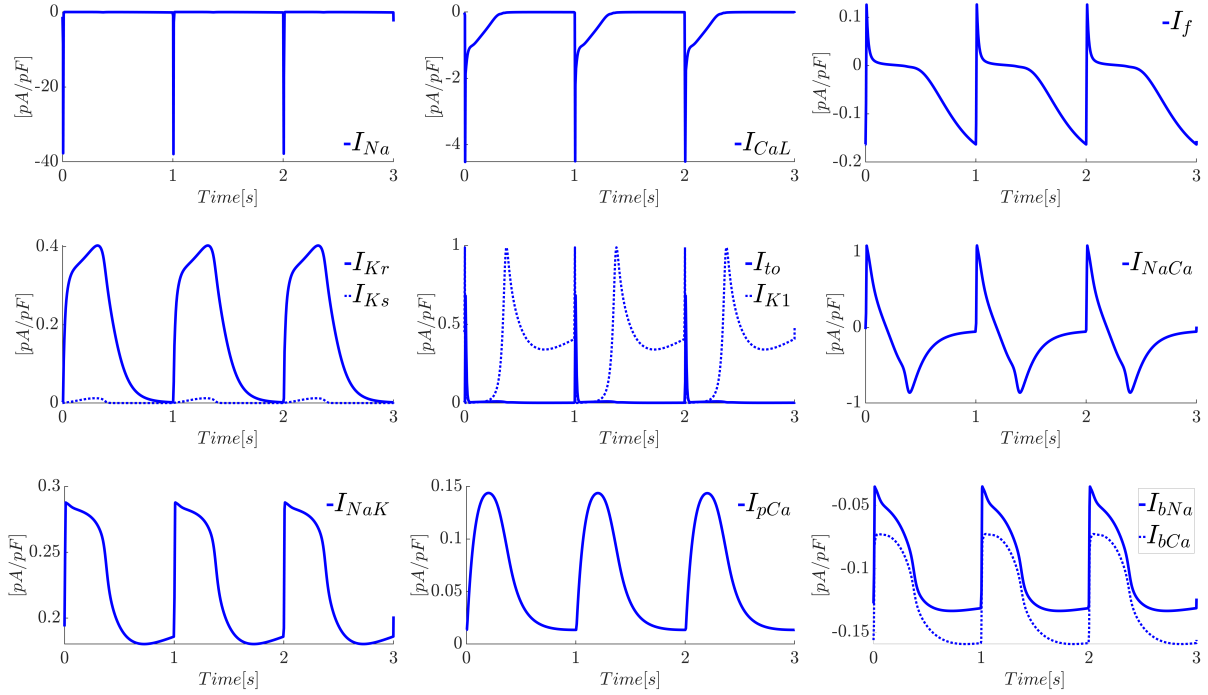
Figure 3.5: Schematic view of main membrane currents at steady state, for the ventricular-like model paced at $1Hz$.

To sum up the previous detailed description, the model consists of a set of 12 currents and 18 variables, differentiated into:

- Action Potential V_m, described by equation 3.4

- 3 ionic concentrations, described by 3.3, 3.1, 3.2;

- 14 gating variables, involved in 7 different membrane currents.

The generalized Cauchy (1.17), where $\boldsymbol{c} = (Na_i, Ca_i, Ca_{SR})$ and $\boldsymbol{w} = (w_1, \cdots w_{14})$, can be numerically solved using the ODE solver *ode15s* with a maximum step size of $1ms$.

3.1.2 Paci2018

Two minor updates improved the double version of Paci2013.
The first one was published in 2015 and slight improvements in the Paci2013 model were included in terms of parameters rescaling, [86].

Conversely, in 2017, AP model was modified to include the **Late Sodium Current** (I_{NaL}) formulation. The equation incorporated in Paci2013 was based on the one proposed by O'Hara-Rudy [80], fitting the maximal conductance with the new dataset. This current, being a membrane contribution, appears in the schematic diagram in Figure 3.7 and in the total current
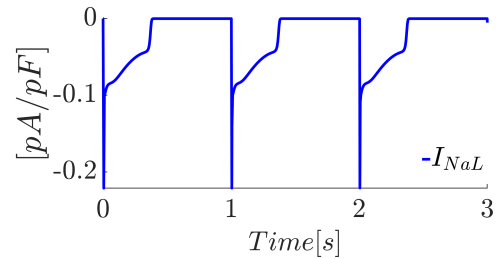
Figure 3.6: Additional I_{NaL} current

contribution for sodium and voltage dynamics, 3.12, 3.13

$$I_{NaL} = g_{NaL} \cdot m_L^3 \cdot h_L^3 \cdot (V_m - E_{Na})$$

where m_L and h_L are two integrated gating variables (current evolution presented in Figure 3.6).

A minor change appears also in the final version of Paci2018, concerning the mixed permeability of ions K^+ and Na^+. The new model formulation accounts also a specific Sodium contribution in the total I_f. This is the **Sodium component of the Funny current** (I_{fNa}) that does not change the total membrane current I_{ion}, but only affects intracellular sodium dynamic. Such current depends on the same gating variable x_f and is described by the simple formulation

$$I_{fNa} = 0.42 \cdot g_f \cdot x_f \cdot (V_m - E_{Na}).$$

The funny current flows in pacemaker channels, that are important parts of the electrical conduction system of the heart (nodal-line cells). Thus, in a context of immature cells evolving towards adult phenotypes, ventricular-like cells move to phenotypes not characterized by I_f. Even if this current does not appear in the schematic diagram 3.7, it plays an important role in the new Na^+ dynamic, written in equation 3.12.

The development of disease-specific models and the great investigation on hiPSC-CMs response to antiarrhythmic drugs steered models towards a ventricular-like characterization, hiding the underlying variability of different hiPSC-CMs phenotypes. Thus, starting from Paci2018, we are going to analyse ventricular-like hiPSC-CMs.
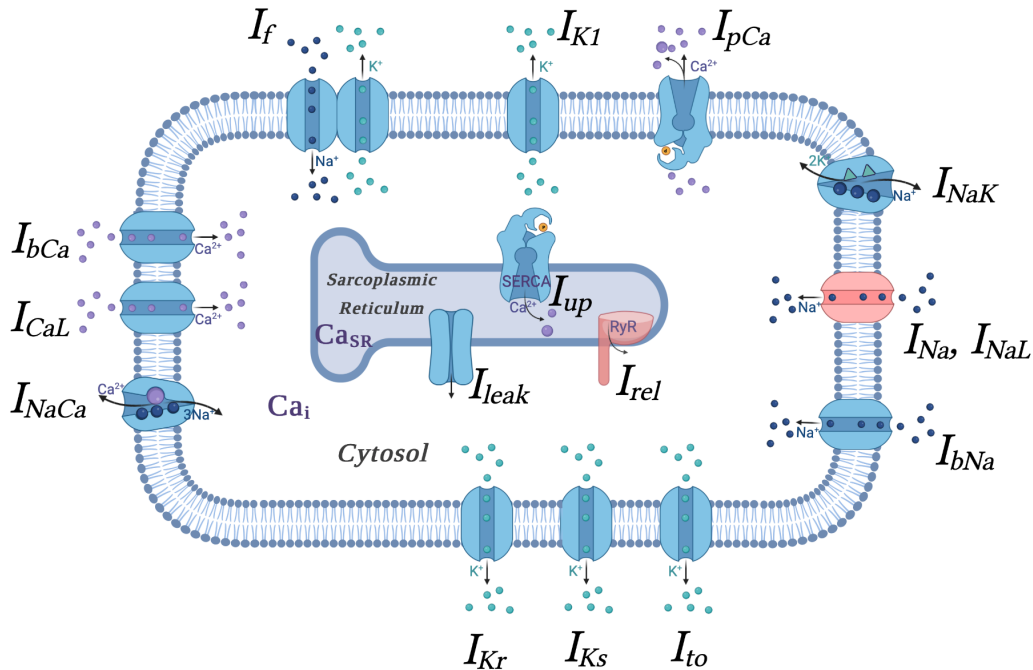
Figure 3.7: Schematic diagram of the model depicting the major functional components and the 13 membrane currents. Red channels identify currents with a different formulation with respect to the previous model. Ca^{2+}-handling is described by: I_{up} uptaking Ca^{2+} by SR, I_{rel} releasing Ca^{2+} by ryanodine receptors and I_{leak}.

Figure 3.7 shows a schematic diagram of the model, depicting the compartmentalization (cytosol and sarcoplasmic reticulum), essential for the calcium handling description. The elementary sodium evolution is written below, as the classical Hodgkin-Huxley formulation, describing the action potential through 13 membrane currents.

$$\frac{dNa_i}{dt} = -\frac{I_{Na} + I_{NaL} + I_{fNa} + I_{bNa} + 3I_{NaK} + 3I_{NaCa}}{FV_c} \tag{3.12}$$

$$\frac{dV_m}{dt} = -I_{Na} - I_{NaL} - I_{CaL} - I_f - I_{K1} - I_{Ks} - I_{Kr} - I_{to} - I_{NaCa} - I_{NaK} + \tag{3.13}$$
$$- I_{pCa} - I_{bNa} - I_{bCa} + I_{stim};$$

The growing importance of the novel *in-vitro* method for hiPSC-CMs led in few years to a better understanding of their specific biophysical mechanism and a great amount of action potential and calcium transient data. Particular attention was reserved to Ca^{2+} handling, thus an update version of the ventricular model was proposed with a more flexible Ca^{2+} handling formulation, [83].

Calcium Handling System Formulation

In cardiac myocytes, the process triggered by the action potential and resulting in the myocyte contraction is the excitation-contraction coupling. The mechanism, previously described as Calcium-induced calcium-released in 1.3.2, starts with the Ca^{2+} influx from the extracellular space through L-type calcium channels. This influx is sufficient to trigger calcium release from the Sarcoplasmic reticulum via specific calcium release channels, commonly called Ryanodine receptors (RyRs), increasing the cytosolic calcium. During the contraction cycle, calcium influx and efflux need to be balanced, thus the majority of Ca^{2+} is reabsorbed to SR by the specific enzyme Ca^{2+} APT-ase, called Sarco-Endoplasmic Reticulum Calcium ATP-ase (SERCA pump), restoring the Ca^{2+} to its basal cytosolic concentration.

The dynamic components of the cell dealing with the CICR mechanism are the membrane current, the intracellular and SR calcium concentrations. Their evolutions are completely described by three different currents: I_{up}, I_{leak}, I_{rel}.

The formulation of the SERCA pump (I_{up}) and the passive leakage current (I_{leak}) were not changed with respect to the Paci2013 model, inspired by the Ca^{2+} handling system of Ten Tusscher, [124]. Those are, respectively,

$$I_{up} = \frac{V_{max,up}}{1 + \frac{K_{up}^2}{Ca_i^2}} \tag{3.14}$$

$$I_{leak} = V_{leak} \cdot (Ca_{SR} - Ca_i) \tag{3.15}$$

where $V_{max,up}, V_{leak}, K_{up}$ are specific parameters, considered during the optimization process.

On the other hand, the same article purposed a functional but simplified description of the Ca^{2+} release from SR (I_{rel}). This quite elementary formulation of I_{rel} showed that the current is

not activated by the cytosolic calcium concentration sensed by the Ryanodine-sensitive receptors, but it is triggered in the same way as the membrane calcium current. This prevents the model producing proarrhythmic triggers, such as delayed after depolarization (DAD) and allowed a calcium flux also for an empty SR, which is clearly impossible.

In Paci2018, the description of calcium release flux through the RyR channel was reformulated I_{rel} according to the novel phenomenological model proposed by Koivumäki in 2011, [47].

$$I_{rel} = I_{rel,max} \cdot RyR_{CaSR} \cdot RyR_o \cdot RyR_c \cdot (Ca_{SR} - Ca_i) \qquad (3.16)$$

where $I_{rel,max}$ is the maximum Ca^{2+} release and the parameter RyR_{CaSR}, described below, express the dependence on Ca_{SR}.

Employing a Hodgkin Huxley formalism, the model has three gating variables: open (activation) Ryr_o, closed (inactivation) Ryr_c and adaptation RyR_a, used to modulate the working point of the RyR_o and RyR_c variables according to the cytosolic Ca^{2+} concentration (see Figure 3.8). Paci2018 model is now able to reproduce the dependence on intracellular calcium and the adaptation of RyR open probability's dependence on intracellular Ca^{2+}. The steady-state formulation is written in the following way:

$$RyR_{a,ss} = RyR_{a1} - \frac{RyR_{a2}}{1 + e^{\frac{Ca_i - RyR_{a,half}}{RyR_{a,k}}}}$$

$$RyR_{o,ss} = 1 - \frac{1}{1 + e^{\frac{Ca_i - RyR_{o,half}}{RyR_{o,k}}}}$$

$$RyR_{c,ss} = \frac{1}{1 + e^{\frac{Ca_i - RyR_{c,half}}{RyR_{c,k}}}}$$

where, RyR_{a1}, RyR_{a2} are constant optimized parameters, while the subscripts $half$ and k indicates, respectively, the half calcium concentration and the slope of the gating variable steady state.

Figure 3.8: Details of the novel calcium-handling gating variables and comparison with the previous Paci2013 model during spontaneous action potential.

To sum up the previous detailed description, the model consists of a set of 12 currents and 21 variables, differentiated into:

- Action Potential V_m, described by equation 3.13

- 3 ionic concentrations, described by 3.3, 3.1, 3.2;

- 15 gating variables, involved in 7 different membrane currents

- 3 gating variables RyR_o, RyR_c, RyR_a standing for the Ryanodine Receptors' probabilities of activation, inactivation and adaptation, needed for the novel characterization of calcium dynamic.

The generalized Cauchy (1.17), where $\boldsymbol{c} = (Na_i, Ca_i, Ca_{SR})$ and $\boldsymbol{w} = (w_1, \cdots w_{18})$, can be numerically solved using the ODE solver *ode15s* with a maximum step size of $1ms$.

3.1.3 Paci2020

The latest version of Paci generation model, released in 2020, is devoted to improving the AP automaticity mechanism.

Recent *in-vitro* and *in-silico* experiments show that the spontaneous electrical activity autonomously stops after a strong block of I_{NaCa}. Instead, in Paci2018 the spontaneous beating was preserved upon the I_{NaCa} block (see Figure 3.10a), and the reason of this failure was identified in a large window current for the fast sodium (I_{Na}).

The improved version of Paci2018 includes the same two compartmental structure of Paci2018, following the same Hodgkin-Huxley membrane potential description (see equation 3.13). Preserving this structure, the development affects three membrane currents, highlighted in the below schematic diagram in Figure 3.9.
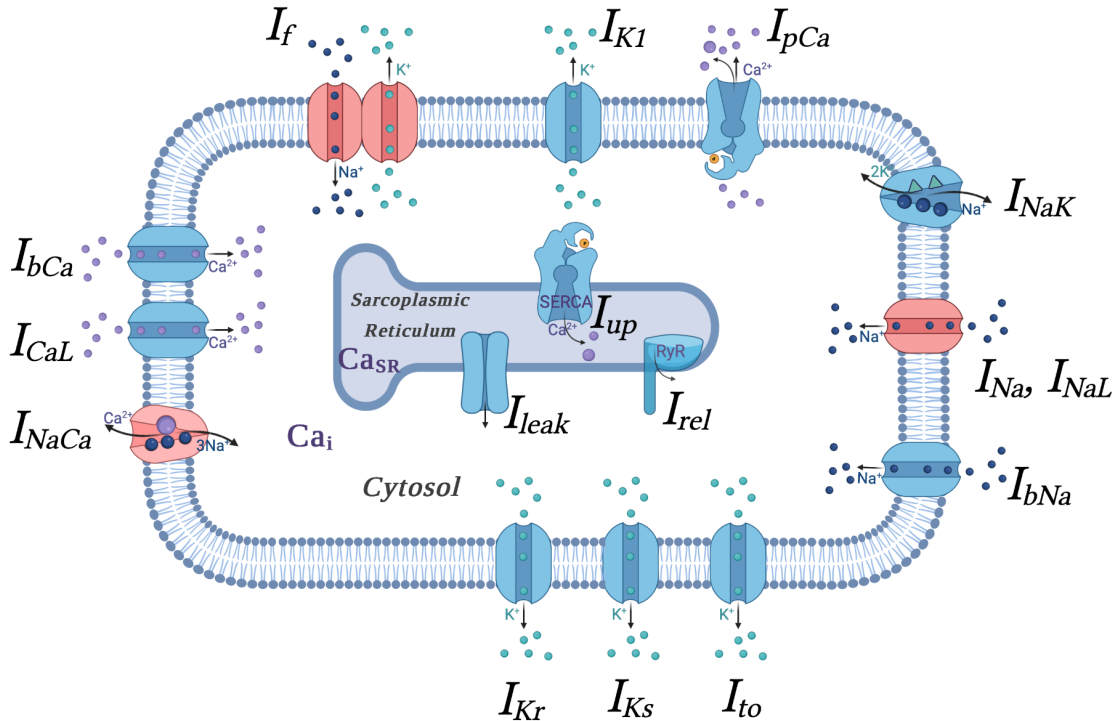
Figure 3.9: Schematic diagram of the model depicting the major functional components and the 13 membrane currents. Ca^{2+}-handling is described by: I_{up} uptaking Ca^{2+} by SR, I_{rel} releasing Ca^{2+} by ryanodine receptors (RyR) and I_{leak}. Membrane currents with a novel formulation are underlined with a different colour.

- The first change concerns the **Sodium current** I_{Na}. The original HH formulation was replaced by the new Koivumäki one [50]. The current equation is always describes by 3.5, but the different formulations of the steady-states $m_\infty, h_\infty, j_\infty$ and the time constants τ_m, τ_h, τ_j lead to a stronger gating evolution 1.10.

- A new updated formulation was written also for the **Funny current** I_f. The previous equation 3.6 was updated with the Koivumäki formulation, [50], in which I_f is expressed as the sum of two contributions, namely I_{fK} and I_{fNa}, triggered by two different channels.

$$f_{Na} = 0.37 \qquad\qquad\qquad\qquad f_K = 1 - f_{Na} \qquad\qquad (3.17)$$

$$I_{fNa} = f_{Na} \cdot g_f \cdot x_f \cdot (V_m - E_{Na}) \qquad\qquad I_{fK} = f_K \cdot g_f \cdot (V_m - E_K) \qquad (3.18)$$

$$I_f = I_{fNa} + I_{fK}. \qquad\qquad\qquad\qquad\qquad\qquad\qquad\qquad (3.19)$$

- Finally, different parameters involved in the calcium handling mechanism were manually tuned in order to correctly reproduce the cessation of the spontaneous firing activity after a strong block of I_{NaCa}, as reported in 3.10b. That are, for example, the maximum SERCA uptake, the maximum Na^+/Ca^{2+} exchanger and Na^+/K^+ pump.

(a) Paci2018   (b) Paci2020
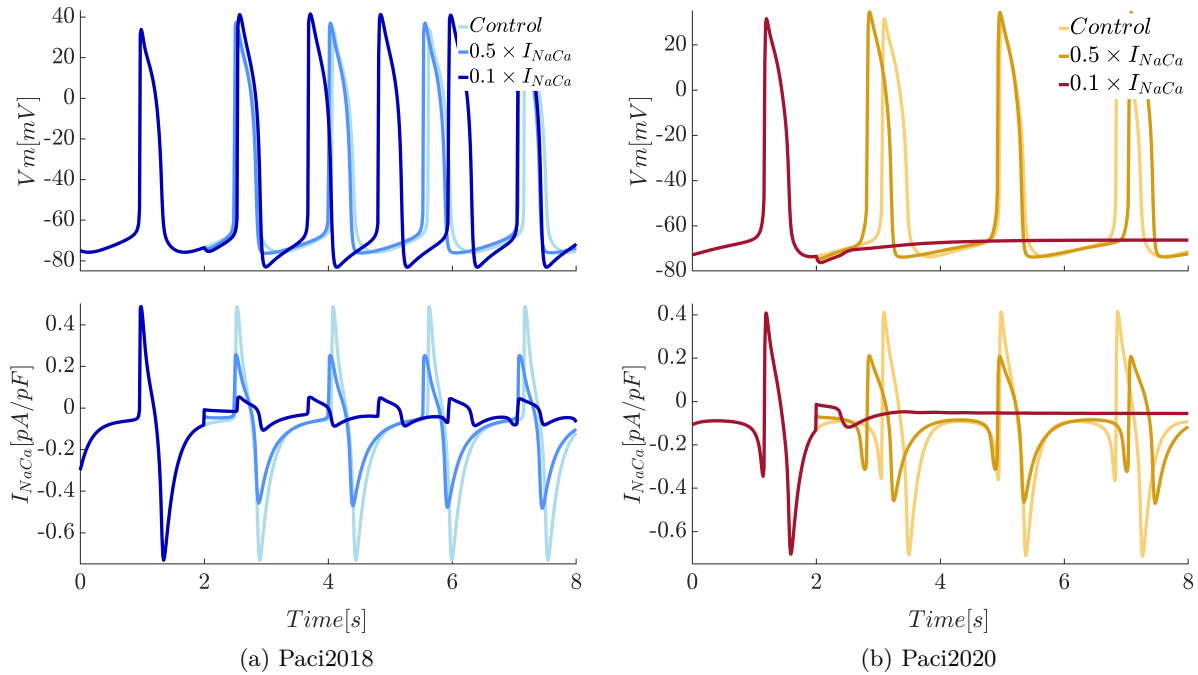
Figure 3.10: Simulation of Paci2018 (3.10a) and Paci2020 (3.10b) considering a strong block of I_{NaCa}: the first model could not allowed the cessation of the spontaneous activity, while the second correctly modeled this phenomenon.

As a result, these three changes allowed the cessation of the spontaneous electrical activity after a strong block of the I_{NaCa}, as depicted in figure 3.10b. We can now state that the spontaneous firing, namely the depolarization of the membrane potential, is triggered by the I_{NaCa}, elicited both by I_f and Calcium release from SR.

To sum up the previous detailed description, the model consists of a set of 13 currents and 22 variables, differentiated into:

- Action Potential V_m, described by equation 3.13

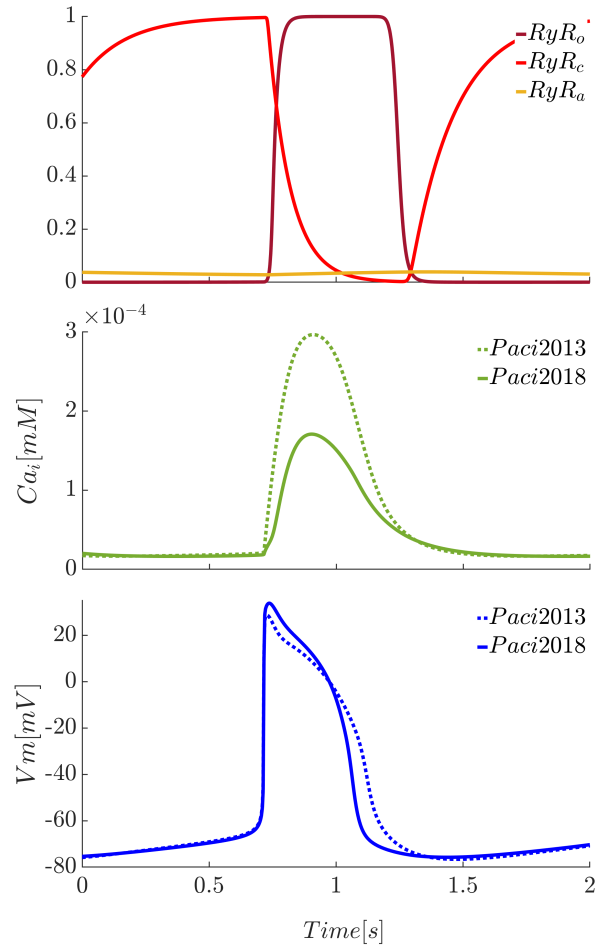- 3 ionic concentrations, described by 3.3, 3.1, 3.2;

- 16 gating variables, involved in 7 different membrane currents

- 3 gating variables RyR_o, RyR_c, RyR_a standing for the Ryanodine Receptors' probabilities of activation, inactivation and adaptation, needed for the novel characterization of calcium dynamic.

The generalized Cauchy (1.17), where $\boldsymbol{c} = (Na_i, Ca_i, Ca_{SR})$ and $\boldsymbol{w} = (w_1, \cdots w_{19})$, can be numerically solved using the ODE solver *ode15s* with a maximum step size of $1ms$.

3.1.4 Comparison

In the following pages (Figure 3.11) the growth of the Paci generation is depicted in a global view of all the membrane and sarcoplasmic reticulum currents. In Figure 3.12 the evolution of the Calcium dynamics from Paci2013 to Paci2018 is highlighted, as well as the evolution of the pumps dynamic from Paci2018 to Paci2020.

Another useful tool to compare models is the agreement with action potential biomarkers. Existing experimental data are from Ma et al. [66], and refer to spontaneous action potentials. Simulated values for each Paci generation model are reported in Table 3.1. Comparing Paci2013 and Paci2020 errors we can see that lots of them considerably get lower, while all the others are bounded.

Biomarkers	Exp. value (Mean $\pm$ SD)	Paci2013 Sim. value	Err.	Paci2018 Sim. value	Err.	Paci2020 Sim. value	Err.
MDP $[mV]$	-75.6 ± 1.2	-76.65	1.39	-75.74	0.18	-74.84	1.0
APA $[mV]$	104.0 ± 1.1	105.21	1.17	109.67	5.45	102.07	1.85
$Peak$ $[mV]$	28.3 ± 1.0	28.52	0.79	33.92	19.85	27.23	3.78
APD_{10} $[ms]$	74.1 ± 4.8	64.65	12.75	86.94	17.32	87.6	18.22
APD_{30} $[ms]$	180.0 ± 10.7	246.61	37.00	243.42	35.23	224.14	24.52
APD_{90} $[ms]$	414.7 ± 21.8	433.28	4.48	379.72	8.44	392.17	5.47
$RappAPD$	2.5 ± 0.2	3.02	21.0	3.14	25.6	2.64	5.8
CL $[ms]$	1700 ± 100	1600.3	5.86	1548.7	8.94	1714.8	0.87

Table 3.1: Recorded action potential parameters (Exp. value) from [66], simulated biomarkers and Percentage errors for each model.
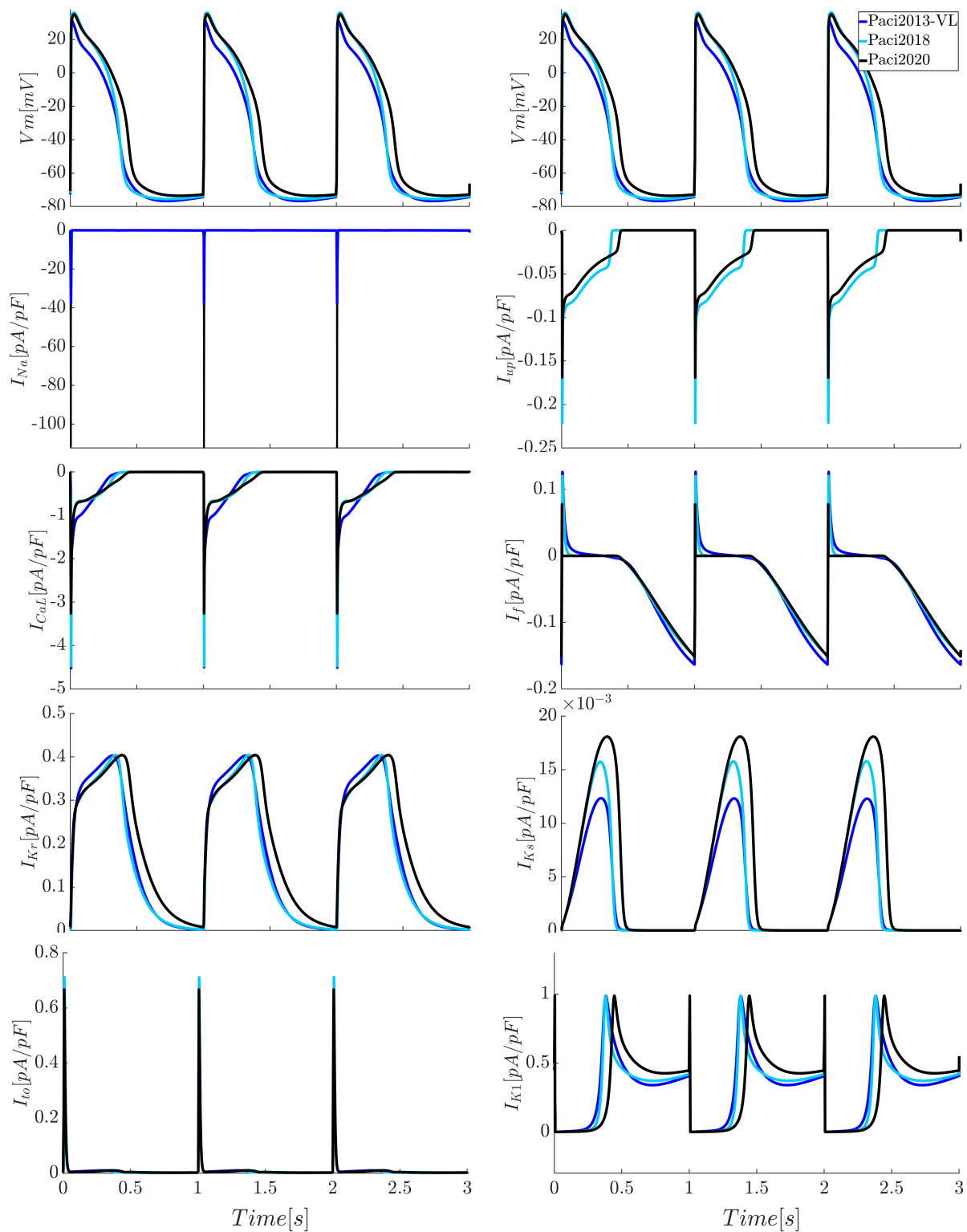
Figure 3.11: Membrane individual currents at steady-state. Simulation were performed with the pacing at 1Hz.
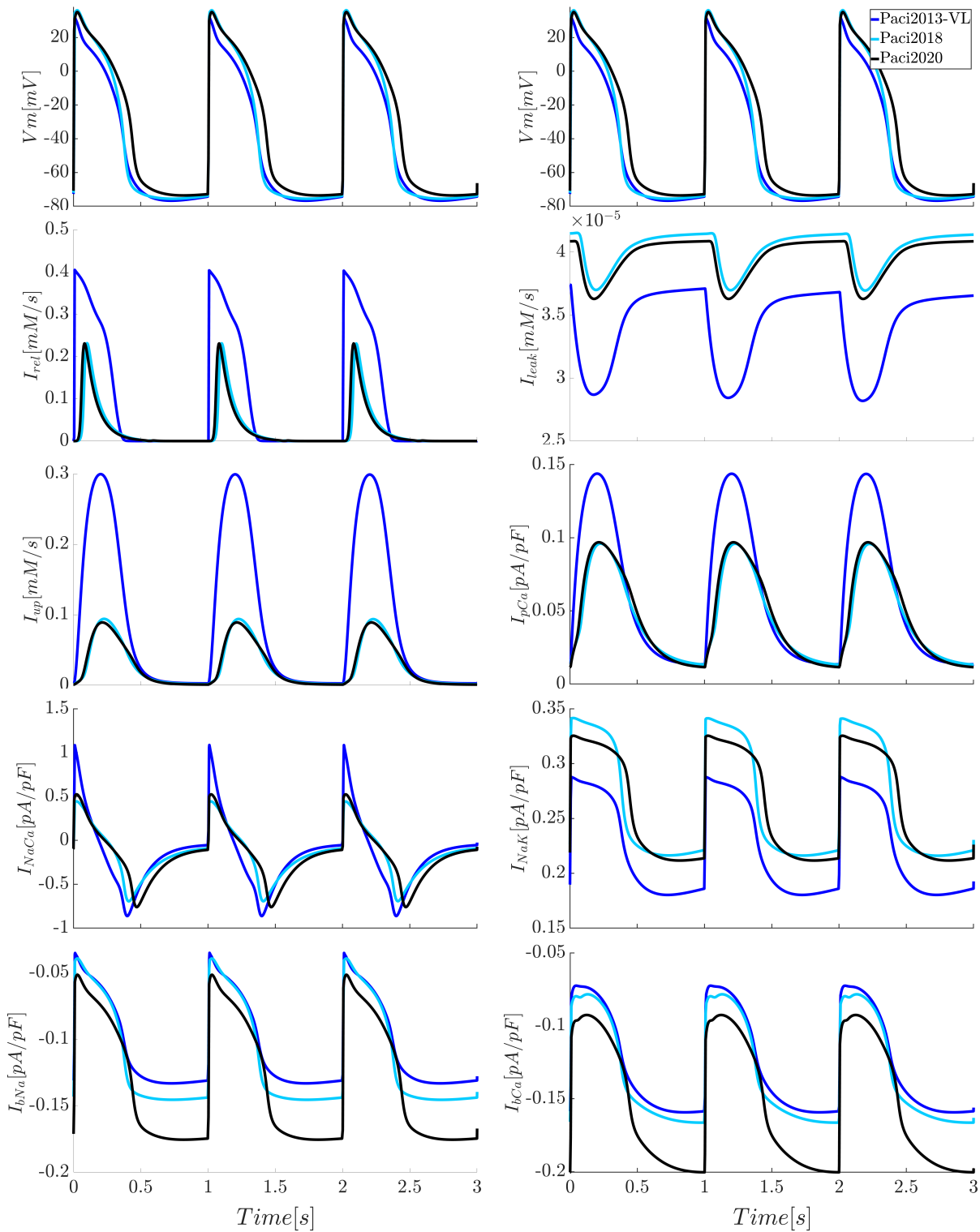
Figure 3.12: Sarcoplasmic Reticulum ($I_{rel}, I_{leak}, I_{up}$), background ($I_{bNa}, I_{bCa}$), pumps and exchangers ($I_{NaCa}, I_{pCa}, I_{NaK}$) currents at steady-state. Simulation were performed with the pacing at 1Hz.

3.2 Other generations

Two different pedigrees were published recently and both of them provided insights and contributions for the last Paci2020 model.

3.2.1 Koivumäki2018

The second pedigree appeared in 2018 based on the Paci2013 model, merging the membrane electrophysiology with a novel cell geometry structure and an inhomogeneous subcellular calcium distribution, [50].

Almost every membrane current preserved the original formulation, except for three of them, listed below and marked in the schematic diagram in Figure 3.13, namely:

- **Fast sodium** current I_{Na} was modified to be better in line with Skibsbye et al. model, [117]. The current equation is always written as equation 3.5, but the steady-state formulations $m_\infty, h_\infty, j_\infty$ and the time constants τ_m, τ_h, τ_j were updated to a better formulation. This formulation will be later used by Paci in the update version of Paci2020.

- **Hyperpolarization activated** current I_f was changed with a new one, published in 2007 [109]. Exactly like the I_{Na} current, this new formulation was adopted by Paci2020 and the current equations has been presented in 3.19.
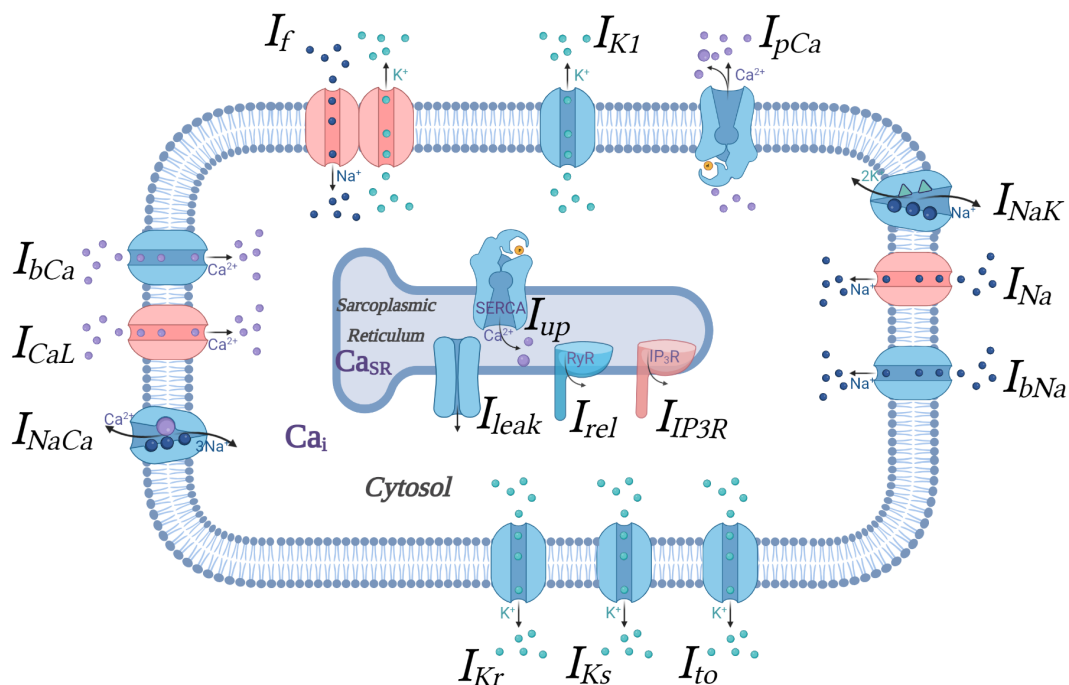
Figure 3.13: Schematic diagram of the model depicting the major functional components. Ca^{2+}-handling is described by: I_{up} uptaking Ca^{2+} by SR, I_{rel} and I_{IP3} releasing Ca^{2+} by ryanodine receptors and inositol trisphosphate proteins, respectively, finally I_{leak}.

- **L-type calcium** current I_{CaL}: this model variant comes from Koivumaki model of 2014, [49], and the current equation reads

$$I_{CaL} = g_{CaL} \cdot d \cdot f2 \cdot fCa \cdot (V_m - E_{Ca,app}),$$

where $E_{Ca,app} = 60mV$ is the considered Ca^{2+} reversal potential.

This model was published in the same year of Paci2018, and both of them developed a realistic representation of calcium dynamic, focusing on the interplay between calcium signals and membrane voltage. Unlike the mechanisms described in sections 1.3.2 and 3.1.2, Koivumäki focused on the structural immaturity affecting the cell and of the cycle as a consequence. Comparable structures exist in embryonic cardiomyocytes, as confirmed by measurements of the Calcium propagation speed in embryonic mouse myocytes.

The interaction between the calcium clock and the membrane clock is the underlying spontaneous electrical activation of hiPSC-CMs. Zhang et al. in [142] proved that the density of the functional I_f pacemaker current is not sufficient on its own for a spontaneous AP triggering, while RyR or SERCA inhibitions reduces the spontaneous activity. In this specific CICR model, cellular receptors responsible for the spontaneous Ca^{2+} release are both the RyRs and inositol trisphosphate proteins (IP3Rs). As described above, the embryonic calcium handling is a suitable description of a hiPSC-CMs CICR mechanism, thus the embryonic cell Ca^{2+} release model is applicable to hiPSC-CM modeling, [51].

Under this assumption, the Calcium release current can be expressed as the sum of two contributions, from the RyR receptors (I_{rel}) and from IP3Rs (I_{IP3}), whose purposed equations are from [44] and [118], respectively. On the other hand, I_{up} and I_{leak} present the standard TT formulation, namely 3.14 and 3.15. Additional equations are

$$I_{rel} = \mu_1 \cdot x_{RyR} \left(PO2 + P_{O2} \right) \cdot (Ca_{SR} - Ca_i) \tag{3.20}$$

$$I_{IP3} = IP3_{kf} \cdot (0.1 \cdot IP3_o + 0.9 \cdot IP3_a)^4 \cdot (Ca_{SR} - Ca_i) \tag{3.21}$$

where P_{O1}, P_{O2} are the gating variables standing for the transition probabilities between two different open states and $IP3_o, IP3_a$ gating variables are the receptor probabilities of opening and activating.

Differences in the CICR set of equations involve differences in the ionic current concentrations, here Ca_i, Ca_{SR}, Na_i and the additional K_i, defined by the following set of ODEs:

$$\frac{dCa_i}{dt} = I_{leak} - I_{up} + I_{rel} - \frac{I_{CaL} + I_{bCa} + I_{pCa} - 2I_{NaCa}}{2FV_c}$$

$$\frac{dCa_{SR}}{dt} = \frac{V_c}{V_{SR}} \left(I_{up} - I_{rel} - I_{leak} - I_{IP3} \right)$$

$$\frac{dNa_i}{dt} = -\frac{I_{Na} + I_{fNa} + I_{bNa} + 3I_{NaK} + 3I_{NaCa}}{FV_c}$$

$$\frac{dK_i}{dt} = -\frac{I_{to} + I_{Ks} + I_{Kr} + I_{K1} + I_{fK} - 2I_{NaK} + I_{stim}}{FV_c}$$

3.2.2 Kernik2019

The last generation we are taking into account is the Kernik model, in a study aimed to extend the existing descriptions to a wide range of hiPSC-CMs phenotypes, incorporating several calcium handling datasets. This model was developed in 2019 and includes 13 transmembrane currents (see Figure 3.15) such that:

$$\frac{dV_m}{dt} = - I_{Na} - I_{CaL} - I_f - I_{K1} - I_{Ks} - I_{Kr} - I_{to} - I_{CaT} - I_{NaCa}+ \tag{3.22}$$
$$- I_{NaK} - I_{pCa} - I_{bNa} - I_{bCa} + I_{stim}.$$

The ions dynamic is highly comparable to the Koivumäki2018 one, previously presented by Ten Tusscher [131] and Luo Rudy [63]:

$$\frac{dCa_i}{dt} = I_{leak} - I_{up} + I_{rel} - \frac{I_{CaL,Ca} + I_{CaT} + I_{pCa} + I_{bCa} - 2I_{NaCa}}{2FV_c}$$
$$\frac{dCa_{SR}}{dt} = \frac{V_c}{V_{SR}} \left(I_{up} - I_{rel} - I_{leak} \right)$$

each of them rescaled for the constant $Ca_{Buf,C}$ and $Ca_{Buf,SR}$ respectively, standing for the assumption of rapid equilibrium approximation for calcium buffers in various compartments. Furthermore,

$$\frac{dNa_i}{dt} = -\frac{I_{Na} + I_{fNa} + I_{CaL,Na} + I_{bNa} + 3I_{NaK} + 3I_{NaCa}}{FV_c}$$
$$\frac{dK_i}{dt} = -\frac{I_{to} + I_{Ks} + I_{Kr} + I_{K1} + I_{fK} + I_{CaL,K} - 2I_{NaK} + I_{stim}}{FV_c}$$

Different ionic currents preserved the original formulation, previously performed and described for the Paci generation: they are pump and exchanger currents ($I_{NaCa}, I_{NaK}, I_{pCa}$) and background currents (I_{bNa} and I_{bCa}), written in equations 3.7-3.11.

The **T-type calcium current** (I_{CaT}, Figure 3.14) never appeared in previous models, and was introduced because of the experimental data captured in hiPSC-CMs and usually found in embryonic heart, in varying quantities depending on the developmental stage of the cell. This current, of an immature cardiac phenotype, was previously modelled by Maltsev, [73], with the following equation:

$$I_{CaT} = g_{CaT} \cdot f_{CaT} \cdot d_{CaT} \cdot (V_m - E_{Ca}) \tag{3.23}$$

Figure 3.14: Additional T-type calcium current I_{CaT} performed at steady state.

where d_{CaT} is the activation gating variable and f_{CaT} is the inactivation one, both governed by a HH dynamic.
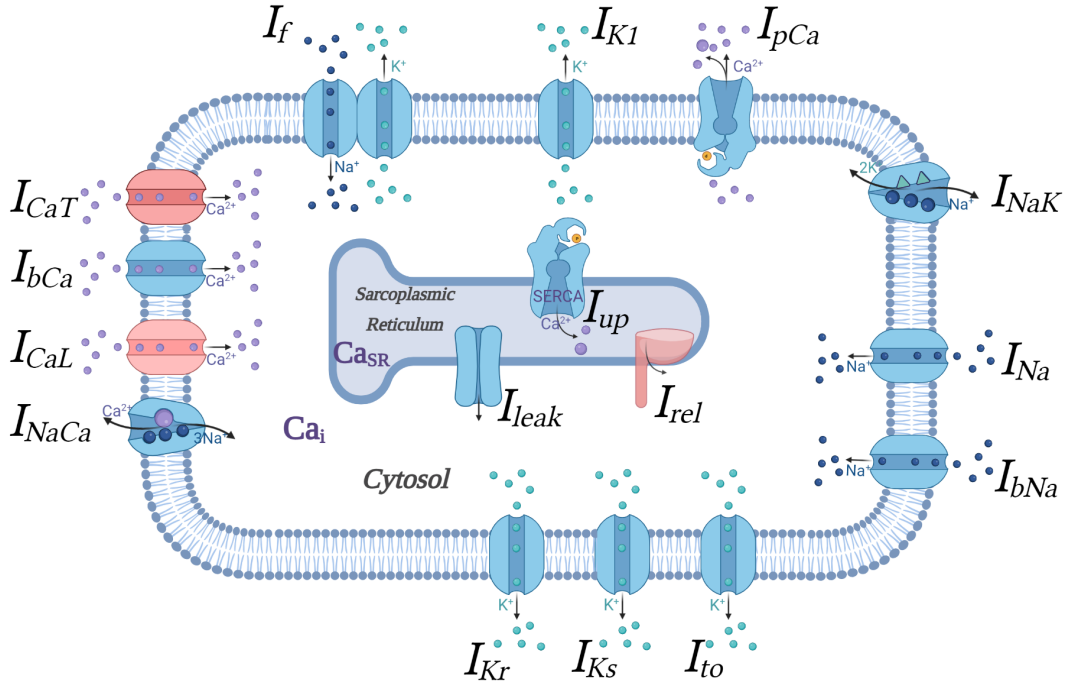
Figure 3.15: Schematic diagram of the cell containing all the ionic processes and compartments in the model.

The **L-type Calcium current** I_{CaL} was extended with a long-winded formulation, taking into account the contribution of each ion. The total current I_{CaL} is the sum of the Ca^{2+}, Na^+, K^+ currents, each of them modelled as 3.1.1 using the HH gates with Goldman-Hodgkin-Katz driving force. Thus, $I_{CaL} = I_{CaL,Ca} + I_{CaL,Na} + I_{CaL,K}$, where

$$I_{CaL,Ca} = \frac{g_{CaL,Ca} \cdot 4V_m F^2}{RT} \cdot \frac{\left(0.341 \cdot Ca_i \cdot e^{\frac{2V_m F}{RT}} - 0.341 \cdot Ca_o\right)}{e^{\frac{2VF}{RT}} - 1} \cdot d \cdot f \cdot fCa \tag{3.24}$$

$$I_{CaL,Na} = \frac{g_{CaL,Na} \cdot V_m F^2}{RT} \cdot \frac{\left(0.75 \cdot Na_i \cdot e^{\frac{V_m F}{RT}} - 0.75 \cdot Na_o\right)}{e^{\frac{VF}{RT}} - 1} \cdot d \cdot f \cdot fCa \tag{3.25}$$

$$I_{CaL,K} = \frac{g_{CaL,K} \cdot V_m F^2}{RT} \cdot \frac{\left(0.75 \cdot K_i \cdot e^{\frac{V_m F}{RT}} - 0.75 \cdot K_o\right)}{e^{\frac{VF}{RT}} - 1} \cdot d \cdot f \cdot fCa \tag{3.26}$$

where d is the activation gating variable, f the inactivation one and fCa calcium-dependent inactivation gate.

The calcium handling formulation was based on prior formulations, leaving I_{up} and I_{leak} currents unchanged. Released current indeed was changed with a Markovian description of the protein activity, according to the Shannon-Bers formulation [113]. Thus,

$$I_{rel} = k_s \cdot o \cdot (Ca_{SR} - Ca_i) \cdot \frac{V_{SR}}{V_c} \tag{3.27}$$

where o is the open gate, itself depending on closed (c) and inactivate (i) gating variables.

The six remaining transmembrane currents, namely $I_{Na}, I_{Kr}, I_{Ks}, I_{K1}, I_{to}$, where formulated using the same formulations of Paci2013. Each of them contained voltage-dependent activation/inactivation gating variables, reformulated using Hodgkin-Huxley-type gating formulation, with single exponential voltage-dependent rate constants.

The generic ion channel model is described by the gating variable w, whose dynamic is defined by the gating equation 1.10

$$\frac{dw}{dt} = \frac{w_\infty - w}{\tau_w} \tag{3.28}$$

where the equilibrium state w_∞ and the rate τ_w constants are

$$w_\infty = \frac{\alpha_w}{\alpha_w + \beta_w} \qquad \tau_w = \frac{1}{\alpha_w + \beta_w},$$

being α_w and β_w the constant transition rates in a first order kinetic.

The simplified single exponential model considers the voltage dependent formula

$$\alpha_w = x_1 e^{\frac{V_m}{x_2}} \qquad \beta_w = x_3 e^{\frac{V_m}{x_4}} + x_5$$

where $x_i, i = 1...5$ are optimized parameters.

3.2.3   Models comparison

Once given a detailed overview of the different models performing the hiPSC-CMs action potentials, it seemed appropriate to summarize differences and similarities of the different pedigrees. In this specific case we took into account the last Paci generation model (Paci2020),

Figure 3.16: Background currents underlying the steady-state action potentials. Simulation were performed with the pacing at 1Hz. Each model was run for 800 s to reach the steady state.
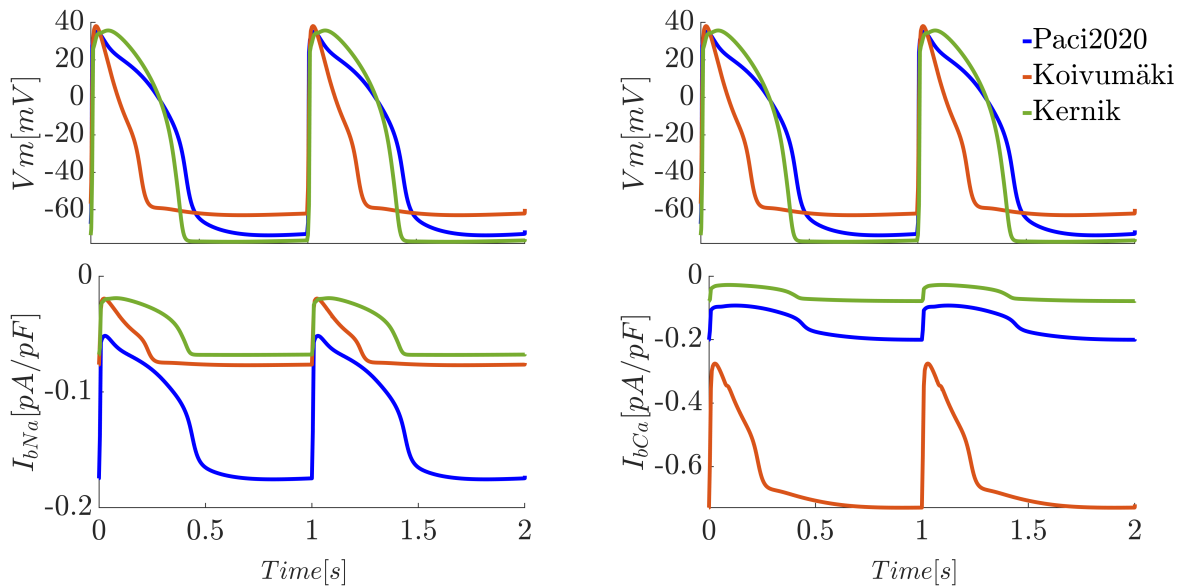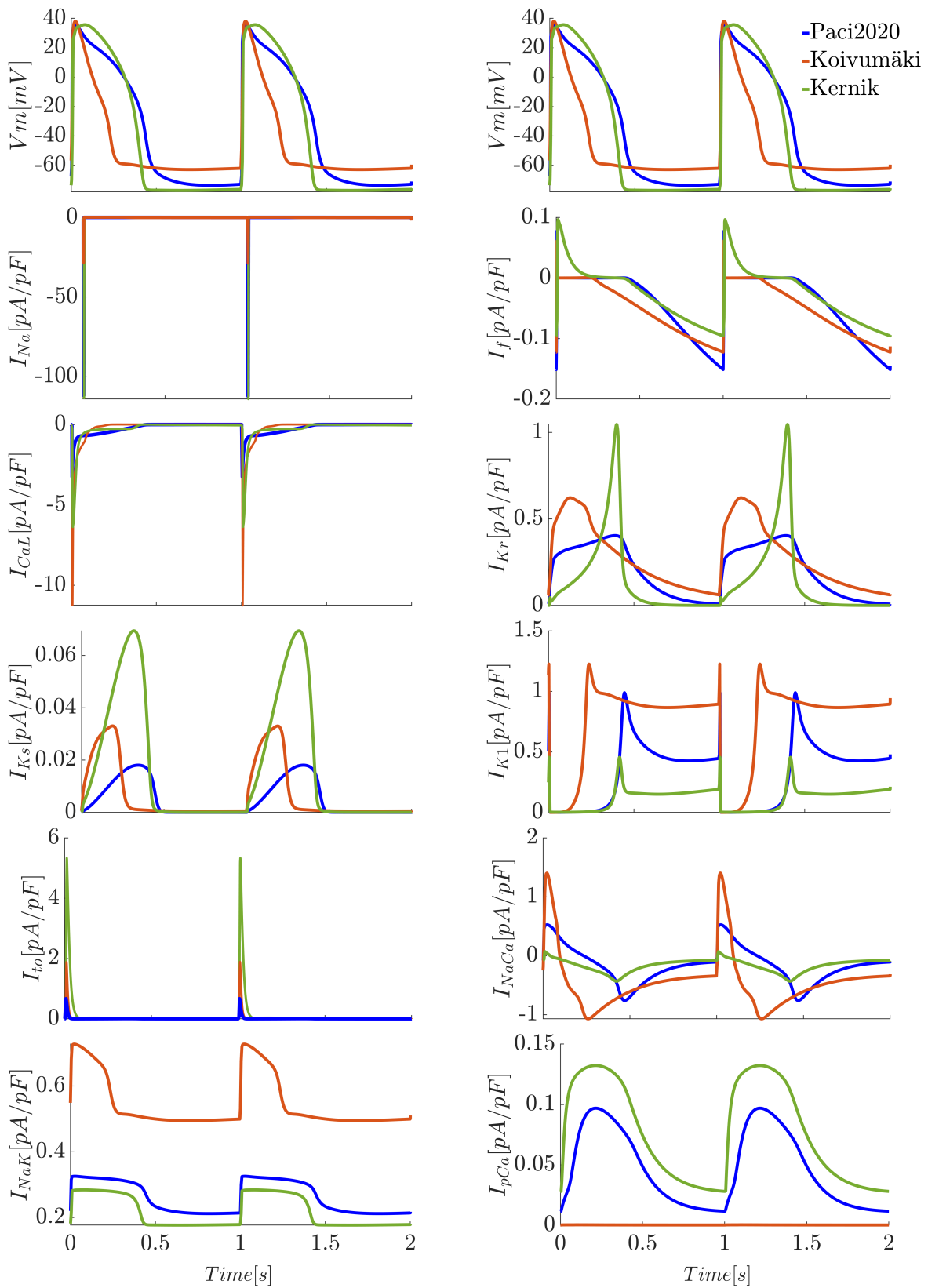
Figure 3.17: Membrane individual ion currents underlying the steady-state action potentials. Simulation were performed with the pacing at 1Hz.

	Paci2020	**Koivumäki2018**	**Kernik2019**
Membrane Currents			
I_{Na}	HH (3)	HH (3)	HH (3)
I_{NaL}	HH (2)	-	-
I_f	HH (1)	HH (1)	HH (1)
$I_{CaL,Ca}$	HH** (4)	HH** (4)	HH** (3)
$I_{CaL,Na}$	-	-	HH** (3)
$I_{CaL,K}$	-	-	HH** (3)
I_{CaT}	HH	HH	HH** (2)
I_{Kr}	HH (2)	HH (2)	HH (2)
I_{Ks}	HH (1)	HH (1)	HH (1)
I_{K1}	HH	HH	HH
I_{to}	HH (2)	HH (2)	HH (2)
I_{NaCa}	TT	TT	TT
I_{NaK}	TT	TT	TT
I_{pCa}	TT	TT	TT
I_{bCa}	HH*	HH*	HH*
I_{bNa}	HH*	HH*	HH
SR Currents			
I_{leak}	HH*	HH*	HH*
I_{up}	TT	TT	TT
I_{rel}	HH* (3)	Markov (3)	Markov (3)
I_{IP3}	-	Markov (5)	-
Equations number	22	26	23

Table 3.2: Summary of the different ion current and Sarcoplasmic fluxes formulations included in the three models
* means that the Hodgkin-Huxley current formulation is modeled as a resistive current
** means that the Hodgkin-Huxley gates formulation is modeled with the Goldman-Hodgkin-Katz driving force

Koivumäki2018 and Kernik2019, that are all based on the original hiPSC-CMs model Paci2013. Paci et al. investigated difference and similarities in the response to 15 different drugs between the pedigrees mentioned above, [84].

They are all single cell models, but they show differences in their compartmental structure: Paci2020 and Kernik 2019 include one compartment for the cytosol and one for the Sarcoplasmic Reticulum, while Koivumäki formulation considers a complex layered compartmentalization. This latter geometry, tightly connected to a different Ca^{2+} dynamic description, takes into account a calcium spatial distribution that approximates the whole cell as a sphere made up of 61 sub-compartments.
Because of the simpler compartments charachterization, Paci2020 and Kernik2019 are faster to simulate, while Koivumäki2018 is almost 100 times slower.

Table 3.2 shows the paradigm used for each current, pointing out the importance of I_{CaL} in Kernik2019. As suggested in [84] this overexpression sustains a stronger spontaneous activity.

Conversely, Paci2020 and Koivumäki automaticity is sustained by a different Ca^{2+} handling.

Finally, in the qualitative comparison presented in Figures 3.16 and 3.17, Koivumäki2018 presents the most triangular AP shape, with a short APD_{90}. According with the above considerations, Paci2020 and Koivumäki2018 show a similar I_{NaCa} shape, because of the role in sustaining the automaticity.

Chapter 4

Dynamic clamp technique

Following the discovery of the electrical properties of cells, it was necessary to develop instruments and protocols suitable for the study of currents crossing the biological membrane through ion channels.

The Patch Clamp technique is the main technique in electrophysiology to record action potentials or membrane currents from isolated cells. The principle of the method is to electrically isolate a patch of membrane from the external solution and record the current flowing into the patch. This is achieved by pressing a glass pipette, which has been filled with an electrode and a suitable solution, against the surface of a cell.

The whole-cell recording is achieved by destroying the membrane patch applying light suction (see Figure 4.1). The interior of the cell then comes into contact with the solution in the pipette, reaching, in a patch phase, a *Giga-Seal* configuration: a seal whose electrical resistance is more than $10 G\Omega$ is formed, [78].

Currently, *Voltage Clamp* and *Current Clamp* are the most widespread recording modes. In the first case, a feedback circuit

Figure 4.1: Patch Clamp configuration, as described in [78]

holds the membrane potential at a set level, allowing the recording of the net membrane current at a given membrane potential. In the second case, it is possible to record the resulting membrane potential of the cell, while the current injected through the patch pipette is under control. Action potential measurements may either occur spontaneously or in response to an injected stimuli current.

A third electrophysiological technique, the **Dynamic Clamp (DC)** method, has been
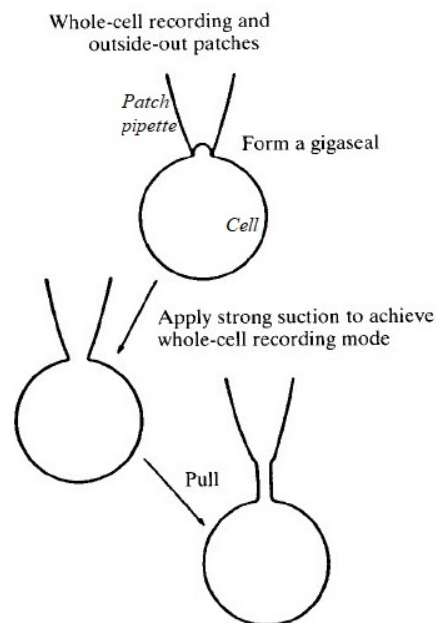
developed as an extension of the traditional intracellular recordings, allowing the introduction of an artificial controlled conductance into the biological cell.

4.1   Dynamic clamp configuration

When we talk about dynamic clamp we are referring to a collection of closely related techniques, where the cell under examination is subjected to a protocol that dynamically evolves over time. It has been introduced by Scott et al in 1979 in the study of bidirectional interaction of two spontaneously beating clusters of embryonic chick ventricular cells. He designed a system in which two isolated cell clusters not in physical contact with each other could be electrically coupled at any desired value of intercellular resistance, [112]. Building on the traditional current clamp, the generic *Coupling clamp* technique creates intercellular electrical coupling through a virtual gap junction between two isolated cardiac myocytes, that are not physically coupled.

Similar techniques were independently introduced in neurophysiology by Sharp et al. with the purpose to introduce artificial conductances into biological neurons and additional membrane ionic current, [101]. Actually, in electrophysiology, this technology may also be used to simulate the presence of an additional current in the membrane of a single isolated myocyte, while it is in free-running current clamp mode [137].

Figure 4.2: Dynamic Clamp feedback loop when injecting an artificial conductance, see [137]

In this second configuration, the membrane potential V_m, recorded from the cell, is continuously sampled into a personal computer. There, the V_m-dependent current I_x may be computed in real-time by a mathematical model and a signal is sent to the amplifier to inject this current into the myocyte.

To sum up, the fundamental steps of the dynamic clamp (see Figure 4.2) can be summarized as follow:

1. Membrane voltage (V_m) is measured using the patch clamp technique;

2. V_m is sent from the amplifier to the data acquisition system of the computer;

3. V_m is used in the computational current model;

4. Calculated current data is sent to the patch clamp amplifier;

5. The current is injected into the cell.

Often, the current I_x comes from the real-time solution of a set of non-linear differential equations, depending on V_m, consequently requiring more complex real-time algorithms for highly realistic

experiments. The aim is to create a system with an update rate higher than the physical phenomenon that is simulated in the model.

Dynamic Clamp does not impose a particular behaviour on the cell but can be considered as a method of studying in experimental set the interaction between excitable cells and a user-specified computational model.

4.1.1 Real-Time eXperiment Interface

The Dynamic clamp closed-loop paradigm is a system where an acquired signal is used to compute the system output. This technology requires closed-loop control that operates on timescales that are physiologically relevant, which span tens of microseconds at the ion channel level. Thus, the core of the experimental setup is the software used as an interface between the set of equations and the hardware used to measure biological parameters. The speed of today's computer processors moves the limiting factor of the overall speed to the rate of signal input and output operation, even if complex mathematical models are used in the computations of the current to be injected. Starting from the choice of a real-time operating system, one of the implementation possibilities is based on a RT-Linux (see Figure 4.3). This system consists of a variant of the usual Linux, where only two software processes are working: the first one is a real-time process with high priority while the second one is with low priority and dedicated to the user interface.

Figure 4.3: RTXI system architecture. The software uses a two-thread architecture where modules communicate and share data in real-time through a signal and slot system

RTXI is a complete and open-source software platform adopted by many labs to administer dynamic clamp experiments. The software provides real-time control using a real Linux operating system and interfaces with different digital acquisition boards (peripheral devices for closed-loop data acquisition), allowing the computer to perform functions of Input/Output, [90].

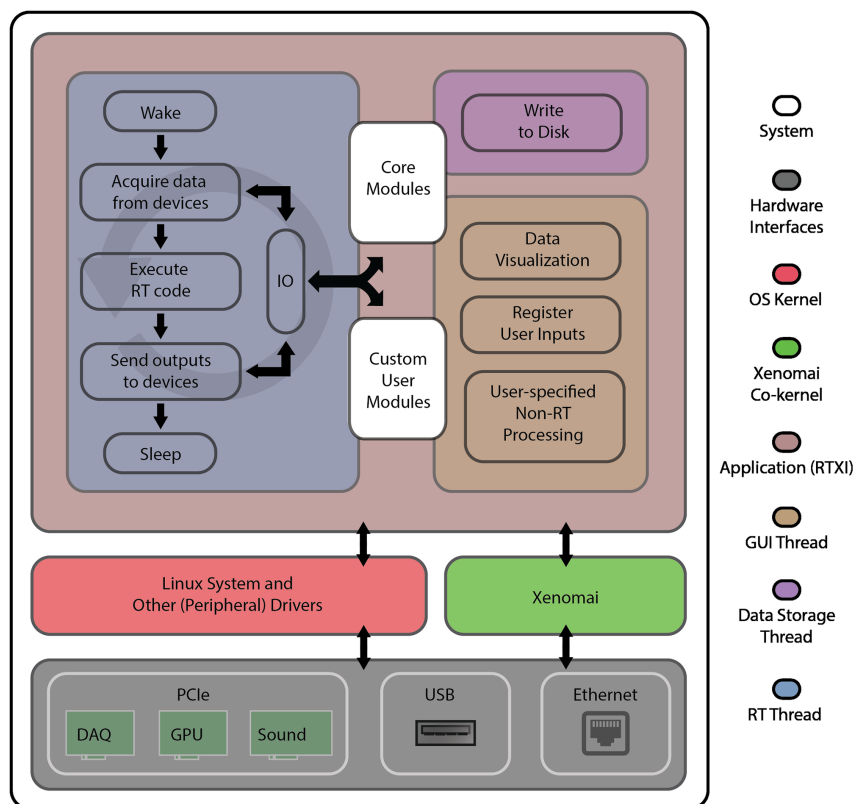RTXI provides a modular architecture, allowing investigators to use pre-existing modules or to construct complex experimental controls by writing self-made C/C++ modules.
The prioritized RT thread wakes on each clock cycle and sequentially runs data acquisition operations, loaded modules functions, and signal output. Then, the thread sleeps until the following cycle.
A separate user interface thread is responsible for all graphical components and user input, allowing for real-time instructions to take priority over graphical components.

4.2 Cardiocentro Ticino Institute experimental observations

Under the suggestion of Professor Krause, we started a collaboration with *Cardiocentro Ticino Institute (CCT)* and *Ente Ospedaliero Cantonale(EOC)*, meeting the team of Prof. Lucio Barile, principal investigator of the Laboratory for Cardiovascular Theranostics. CCT main research interests are largely directed towards understanding pathophysiological mechanisms underlying cardiovascular diseases and focus on finding novel cell-free approaches to promote successful cardioprotection and myocardial regeneration to prevent heart failure.

Following the statement of the previous chapter, hiPSC-CMs result in a mix of cells that can be classified as atrial-, ventricular- or sinoatrial-like CMs. However, they exhibit different action potential (AP) properties that may be a subjective and misleading method to separate different cardiac phenotypes.
Nevertheless, the discrimination of different immature AP morphologies in standard hiPSC-CM culture is difficult and largely debated.
Their recent work aimed to use *in-silico* models to develop a new approach to automatically discriminate the electrophysiological differences between hiPSC-CMs.

4.2.1 DC approach for discrimination of chamber-specific hiPSC-CMs

The *in-vitro* maturation of hiPSC-CMs, in terms of electrical properties and physiology, develops in a time-dependent way. Moreover, the Inward Rectifier Potassium Current (I_{K1}) expression is still too low or lacking, thus leading to more depolarized MDP compared to the mature atrial/ventricular CMs. In these immature electrophysiological conditions, the voltage-gated ion channels, which normally contribute to the AP profile, cannot be activated at the right time and the right density although rightly expressed at the membrane level.
A valid and effective approach to overcoming immature characteristics of hiPSC-CM is the injection of *in-silico* inward rectifier K^+ current in a loop with recorded cellular membrane potential in a real-time mode.
DC allows the hyperpolarization of MDP to values suitable to generate a mature AP waveform,

driving electrical biomarkers towards values useful for a blind classification of differentiating CM, through the specific unsupervised learning algorithm, [2].

Retinoic Acid protocol Multiple differentiation protocols were applied to enrich the functional subtypes. Thus, the conventional standard culture was modified by applying $1\mu M$ of retinoic acid (RA) using a protocol currently considered the best option to push hiPSC differentiation towards an atrial phenotype, [24].

A higher percentage of atrial-like CMs in RA culture was primarily confirmed at a genetic level. Moreover, the treatment yielded a higher beating frequency with a contraction duration, time to peak, and relaxation time shorter in RA than in Control. Consistently, Current Clamp recordings confirmed a higher percentage of atrial-like CMs in RA by overexpression of atrial markers, and downregulation of ventricular ones.

I_{K1} formulations To overcome the lack of I_{K1} in immature hiPSC-CMs, they applied in DC mode two *in-silico* state-of-art currents, choosing from the O'Hara-Rudy [80] computational model of human ventricular AP and from Koivumäki [47] human atrial model the I_{K1} formulation to be injected.

Firstly, the minimum amount of injected current was optimized in order to hyperpolarize the cells to a physiological resting value. The conductance G_{K1} was progressively increased by $0.05nS/\mu F$ per step, reaching $G_{K1} = 0.7nS/\mu F$ as the critical conductance needed to stabilize the MDP and APD_{90} in both atrial and ventricular profiles.

Phenotype classification In order to discriminate phenotypes of differentiated cells, two cell clusters were created on the exclusive basis of nine electrical biomarkers. They showed similar cell capacitance, but they displayed an electrical pattern consistently attributable to a specific phenotype.

In one of the clusters, diastolic membrane potential was less polarized, action potential duration was shorter, with a lower amplitude and more triangular shape. Among those biomarkers, they selected APD_{20}/APD_{90} as the one used to define the cut-off value that could discriminate cells of different clusters, set equal to 0.44. This cut-off was then pharmacologically validated in a distinct subset of cells.

4.2.2 Further observations

Action potentials were recorded by switching the injection of the atrial current formulation from Koivumäki (I_K) and the ventricular current formulation from O'Hara-Rudy (I_{ORd}). In every cell, I_K injection is associated with a more hyperpolarised MDP, leading to distinct AP profiles. The resulting morphologies recapitulate either atrial or ventricular human APs, including both triangular AP shapes without sustained plateau and long AP with a spike-and-dome shape, [2].

Under the injection of the atrial I_K, the triangular form was elicited in atrial CMs and the plateau phase was preserved in ventricular-like CMs. On the other hand, under the injection of the ventricular I_{ORd}, a high percentage of atrial-like CMs gave rise to an irregular plateau
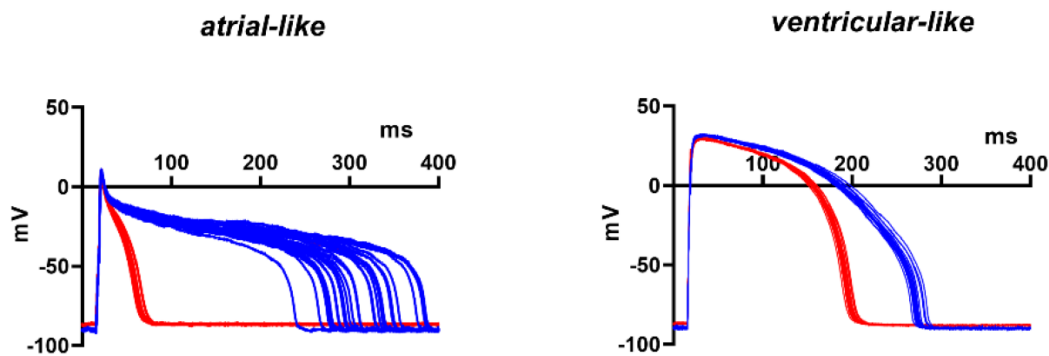
Figure 4.4: In blue, AP recordings after I_{ORd} injection; in red, AP recordings after I_K injection. The Figure is taken from [2]

and ventricular-like CMs elicited a longer AP plateau, as shown in Figure 4.4. Furthermore, the ventricular formulation of I_{K1} injected in atrial-like cells generated abnormal AP waveforms, characterized by a "chair-like" plateau.

In conclusion, the optimized I_{K1} formulation is a promising tool to cluster cells in a heterogeneous population, through the blindly derived cut-off of the APD_{90}/APD_{20} biomarker. Cell clusterisation was obtained by unsupervised learning algorithms.

4.3   Virtual dynamic clamp

Since in the DC technique the injected current can be fully described by mathematical equations, it is useful to perform *in-silico* the whole interface protocol and the current injection. In a fully computational set, it is possible to simulate the hiPSC-CM electrical activity using existing mathematical models, made up of a set of ordinary differential equations, describing dynamics of the ionic currents. Then, it is possible to test different I_{K1} models, comparing the physiological responses and giving a mathematical definition of the waveforms' differences.

In the chosen mathematical membrane model, we firstly suppressed the native I_{K1} current, in order to reach the immature physiological condition of the cell membrane. The we added different I_{K1}formulations taken from existing ionic current models to the total ionic current, as in the experimental DC current injection procedure.

4.3.1   Paci2013 model for hiPSC-CMs

The Dynamic clamp technique indiscriminately deals with both atrial-like and ventricular-like hiPSC-CMs. Virtual DC simulations were performed using the computational ionic model developed by Paci et al. [85], which electrophysiologically characterizes models for both AL and VL hiPSC-CMs. The parameter setting of the model allows us to investigate quantitatively the two AL and VL configurations, even if no atrial-specific current is present in the model. The original Paci2013 model, constrained by experimental data, simulated traces of spontaneous electrical activity.

The first test we performed was about the suppression of the native I_{K1} (red line in Figure 4.5). The lack of the potassium current leads both atrial and ventricular model to a quiescent depolarized resting potential, higher than $-20mV$.

<div align="center">(a) Atrial-like   (b) Ventricular-like</div>
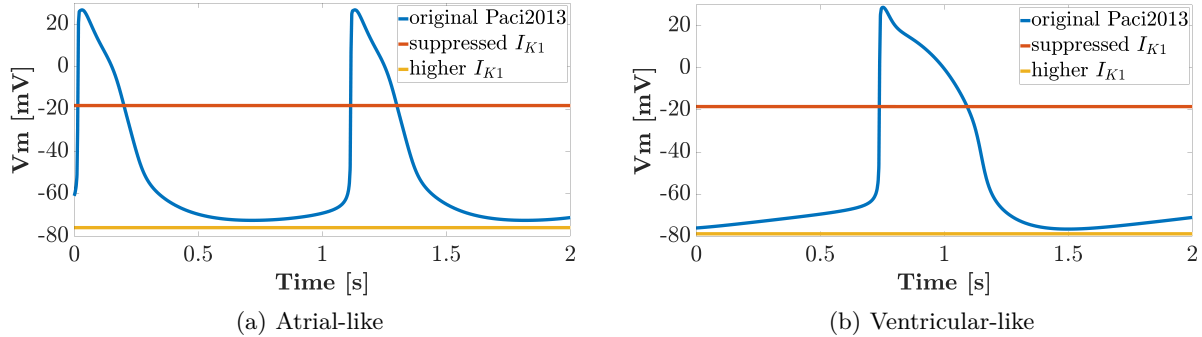
Figure 4.5: Paci2013 simulations considering different I_{K1} current densities: the suppression of this current leads the cell to a depolarized resting potential

Furthermore, in DC experiments the injection of the additional current is joined with the injection of the applied current I_{app}. Anyway, in the virtual dynamic clamp setup, we focused on the I_{K1} injection effects. According to Fabbri [27], the required higher amount of I_{K1} could bring the cell to a stable and hyperpolarized MDP ($\simeq -78\ mV$), the yellow line in Figure 4.5.

In this framework, we assessed the resulting AP morphology under 1 Hz of pacing rate of the models.

4.3.2 Tested inward-rectifier I_{K1} currents

We carried out the virtual dynamic clamp by considering different I_{K1} models available in the literature. In a general perspective, we took into account four ventricular-specific I_{K1} formulations, coming from different human ventricular action potential models, Ten Tusscher (TT) [124], Grandi [33], Fink [30], O'Hara-Rudy (ORd) [80]; two atrial specific I_{K1} formulations, Koivumäki (K) [47] and Courtemanche (CRN) [22], and one mixed formulation published by Bett [14], usually compared to the atrial ones.

Literature I_{K1} formulations are described by the following equations, where

$$E_K = \frac{RT}{F} \log\left(\frac{K_o}{K_i}\right)$$

is the potassium reversal potential (being T the temperature, F the Faraday constant, R the universal gas constant) and V the membrane voltage of the model written in Volt. On the other hand, Paci2013 model is written considering the membrane voltage Vm in millivolt. Thus, the conversion rule is

$$Vm = 10^3 V.$$

Ten Tussscher The first human ventricular model we took into account is the Ten Tusscher Panfilov, published in 2004, [124], and used again in 2006, [130]. The I_{K1} formulation is described

by equation 4.1, where $x_{K1\infty}$ is written as a time-independent inward rectification factor, that is a function of voltage, corresponding to the steady state of a gating variable.

$$\alpha_{K1} = \frac{0.1}{1 + e^{0.06(V-E_K-200)}}$$

$$\beta_{K1} = \frac{3e^{0.0002(V-E_K+100)} + e^{0.1(V-E_K-10)}}{1 + e^{-0.5(V-E_K)}}$$

$$x_{K1\infty} = \frac{\alpha_{K1}}{\alpha_{K1} + \beta_{K1}}$$

$$I_{K1} = G_{K1}\sqrt{\frac{K_o}{5.4}} \cdot x_{K1} \cdot (V - E_K) \tag{4.1}$$

where the maximal conductance in nanosiemens per picofarad is

$$G_{K1} = 5.405 \quad nS/pF. \tag{4.2}$$

Grandi   The second human ventricular I_{K1} formulation is the one published in 2010 by Grandi et al. [33]. Here, the formulation is roughly similar to the previous one, depending on a steady state gating variable $K1_\infty$. For any G_{K1} defined in the literature, thus we will consider the neutral value $G_{K1} = 1 \quad nS/pF$.

$$\alpha_{K1} = \frac{1.02}{1 + e^{0.2385(V-E_K-59.215)}}$$

$$\beta_{K1} = \frac{0.49124 \cdot e^{0.08032(V+5.476-E_K)} + e^{0.06175(V-594.31-E_K)}}{1 + e^{-0.5143(V+4.753-E_K)}}$$

$$K1_\infty = \frac{\alpha_{K1}}{\alpha_{K1} + \beta_{K1}}$$

$$I_{K1} = 0.35\sqrt{\frac{K_o}{5.4}}K1_{ss}(V - E_K) \tag{4.3}$$

Fink   The following ventricular model published in 2008 by Fink presents a huge parameters setup, [30]. The main model equations for I_{K1} are the following 4.5,

$$g_{K1} = g_{K1}^0 \cdot (aT + b) \cdot \sqrt{\frac{Ko}{5.4}} \tag{4.4}$$

$$\frac{G}{G_{max}} = \phi \cdot r_1^\infty(V) + (1 - \phi) \cdot r_2^\infty(V)$$

$$I_{K1} = g_{K1}\frac{G}{G_{max}}(V - E_K) \tag{4.5}$$

where the temperature dependence of the conductance given by Q_{10} yields the parameters a and b. Other parameters and lows are listed below, where $[SPM]$ denotes the intercellular spermidine concentration, Buf_{Mg} and K_{MgBuf} are the Michaelis-Menten law constants.

$a = 1/35$	$b = 55/7$	$g_{K1}^0 = 0.06821 \quad pA/pF/mV$
$\phi = 0.8838$	$s = 1.0648$	$[SPM] = 0.0014613 \quad mM$
$K_{MgBuf} = 0.174 \quad mM$	$Buf_{Mg} = 5.67$	$[Mg^{2+}]_i^{Total} = 5 \quad mM$

$$b = Buf_{Mg} - [Mg^{2+}]_i^{Total} + K_{MgBuf} \qquad c = K_{MgBuf} \cdot [Mg^{2+}]_i^{Total}$$

$$[Mg^{2+}]_i = \frac{1}{2}\left(\sqrt{b^2 + 4c} - b\right) \qquad \psi = 1 + \frac{[Mg^{2+}]_i}{K_{B(Mg)}}$$

$$K_{I(Mg)} = 2.8e^{-\frac{V - s \cdot E_K}{180}} \qquad K_{B(Mg)} = 0.45e^{-\frac{V - s \cdot E_K}{20}}$$

$$K_{d1(SPM)} = 0.0007e^{-\frac{V - s \cdot E_K + 8[Mg^{2+}]_i}{4.8}} \qquad r_1^\infty(V) = \frac{\psi^2}{[SPM]/K_{d1(SPM)} + [Mg^{2+}]_i/K_{I(Mg)} + \psi^3}$$

$$K_{d2(SPM)} = 0.04e^{-\frac{V - s \cdot E_K}{9.1}} \qquad r_2^\infty(V) = \frac{1}{1 + [SPM]/K_{d2(SPM)}}$$

Here, the maximal conductance is defined by equation 4.4, equal to 4.6 for the given specific values of the parameters.

$$G_{K1} = 0.6821 \quad nS/pF \tag{4.6}$$

O'Hara-Rudy The last human ventricular I_{K1} formulation we took into account is the recent O'Hara-Rudy model of 2011, [80]. In this complete formulation, the current depends on the time-independent factor R_{K1} and on the time-dependent gating variable x_{K1} corresponding to an additional ODE, with initial condition $x_{K1}(0) = 0.996801$.

$$x_{K1,\infty} = \frac{1}{1 + e^{-\frac{V + 2.5538K_o + 144.59}{1.5692K_o + 3.8115}}}$$

$$\tau_{x,K1} = \frac{122.2}{e^{-\frac{V + 127.2}{20.36}} + e^{\frac{V + 236.8}{69.33}}}$$

$$\frac{dx_{K1}}{dt} = \frac{x_{K1,\infty} - x_{K1}}{\tau_{x,K1}}$$

$$R_{K1} = \frac{1}{1 + e^{\frac{V + 105.8 - 2.6 + K_o}{9.493}}}$$

$$I_{K1} = G_{K1}\sqrt{K_o} \cdot x_{K1} \cdot R_{K1} \cdot (V - E_K) \tag{4.7}$$

where the maximal conductance is

$$G_{K1} = 0.1908 \quad nS/pF \tag{4.8}$$

Koivumäki The first human atrial model we took into account is the recent Koivumäki, published in 2011 [47], where the Inward Rectifier Potassium Current comes from the previous Nygren model of 1997, [77].

$$I_{K1} = G_{K1}K_o^{0.4457}\frac{V - E_K}{1.0 + e^{1.5(V - E_K + 3.6)\frac{F}{RT}}} \tag{4.9}$$

The equation written above is time independent and the maximal conductance has been updated considering [49], where $g_{K1} = 3.5nS$ and $C_m = 50pF$, thus

$$G_{K1} = \frac{g_{K1}}{C_m} = 0.07 \quad nS/pF. \tag{4.10}$$

Courtemanche   This second considered model is the first human atrial formulation, published in 1998 [22], with a simpler I_{K1} formulation

$$I_{K1} = \frac{G_{K1}(V - E_K)}{1 + e^{0.07(V+80)}} \tag{4.11}$$

where the original maximal conductance is

$$G_{K1} = 0.09 \quad nS/pF. \tag{4.12}$$

Bett   This last model is not a specific human atrial model. The first formulation appeared as a model for both atrial- and ventricular-like human cardiomyocytes, [52], and was then used in 2013 by Bett [14] in a dynamic clamp setup with the following equation specific for undifferentiated hiPSC-CMs

$$I_{K1} = 0.5\frac{V + 85}{1 + e^{0.0896(V+85)}} + 0.01(V + 85). \tag{4.13}$$

As suggested by Fabbri et al. [27], we conducted *a priori* comparison between the seven I_{K1} formulations. First of all, we scaled all of them in order to obtain the same outward peak current density ($0.63pA/pF$), corresponding to the peak of the Koivumäki model, this one being one of the most recent AL models. Thus, given

- I_K the reference Koivumäki current equation in 4.9

- I_F the alternative current formulation with $K \in \{TT, Grandi, Fink, ORd, CRN, Bett\}$, where the formulation 4.7 has been considered at the steady state version
  $I_{K1} = G_{K1}\sqrt{K_o} \cdot x_{K1,\infty} \cdot R_{K1} \cdot (V - E_K)$

the scaling factors $\mathcal{K}_F$ can be easily found imposing $\max I_K = \mathcal{K}_F \max I_F \quad \forall F$.

In the following Table, we summarized the literature maximal conductance, and the relative new normalized maximal conductance reduced by the scaling factor. Considering voltages between -120 and $10\ mV$, each normalized model generated the steady state normalized I_{K1} currents shown in Figure 4.6.

Model	Scaling factor	Literature $G_{K1}\,[nS/pF]$	Normalized $G_{K1}\,[nS/pF]$
Ten Tusscher	0.34109	5.405	1.8436
Fink	0.48919	0.6821	0.3337
Grandi	0.41384	-	0.41384
O'Hara-Rudy	0.68753	0.1908	0.1312
Courtemanche	1.1101	0.09	0.0999
Bett	0.36827	-	0.36827
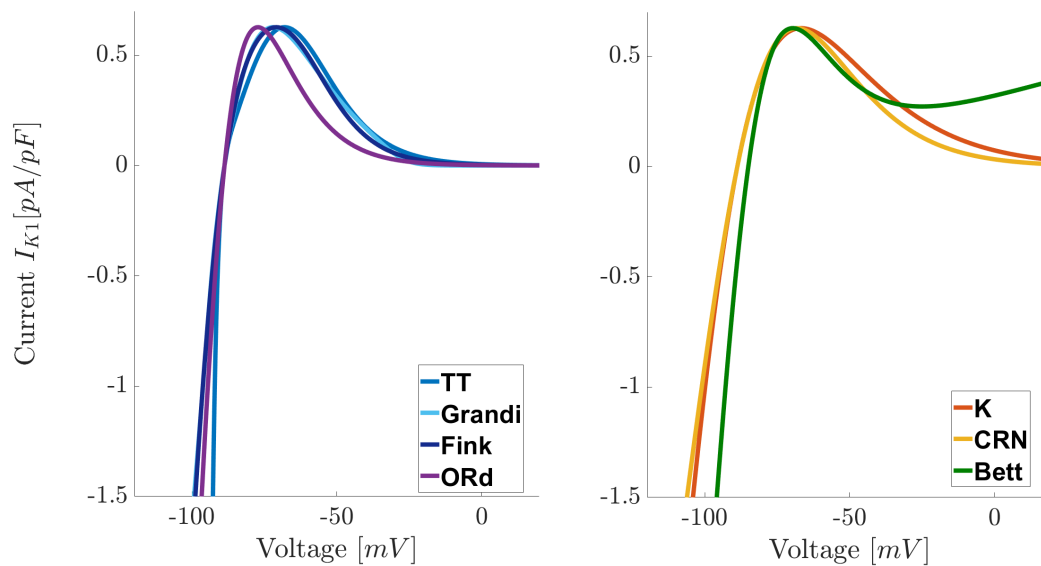
Figure 4.6: Normalized I_{K1} currents from ventricular (left) and atrial (right) ionic models.

4.4 Chair-shape morphology

Once every I_{K1} formulation had been implemented both in the AL and VL Paci2013 model, some simulations were performed considering new formulations instead of the original ones. Some of the normalized currents allowed the model to reach a stable and hyperpolarized MDP, and the applied current injection enabled the generation of an action potential. Results support experimental observations, generalizing them. *In-vitro* AP recording only highlighted a longer AP plateau in VL CMs and an abnormal AP waveform in AL cells under the injection of a ventricular O'Hara-Rudy I_{ORd} formulation. *In-silico* simulations presented irregular APs uppermost in the previous cases, characterized by a "chair-like" plateau, but every I_{K1} formulation gave rise to a longer AP plateau both for atrial-like and ventricular-like CMs.

4.4.1 Definition

The AP morphology for different atrial and ventricular I_{K1} formulations changes with respect to the density of the injected current. The AP morphology was absolutely non-physiological for low percentages of the injected current, while it became physiological for higher densities.
The stretching of the AP appeared in the repolarization phase (phase 3 in figure 1.3), corresponds to an additional change of the concavity of the AP. This phenomenon disappears for high densities injected currents, where the number of inflections is lower.

This morphology change is shown in Figure 4.7, considering an additional ventricular current formulation (O'Hara-Rudy), and in Figure 4.8, considering an additional atrial current formulation (Koivumäki).

The mathematical description of the morphology allows the definition of a mathematical criterion to classify AP morphologies based on the number n_I of AP inflections between the AP

peak and the resting MDP. More precisely, we have the following

Mathematical criterion 1. *Given $t \in [T_{stim1}, T_{stim2}]$ the time between two consecutive stimuli and $A = \left\{ \bar{t} \in [T_{stim1}, T_{stim2}] : \frac{\partial^2 V}{\partial t^2}(\bar{t}) = 0 \right\}$ the set of inflections we state that:*

- *if $n_I = \operatorname{card} A \geq 7$ the action potential presents a Chair shape morphology*

- *if $n_I = \operatorname{card} A \leq 6 \Rightarrow$ the action potential presents a Non-Chair shape morphology.*

(a) Chair shape   (b) Non-chair shape
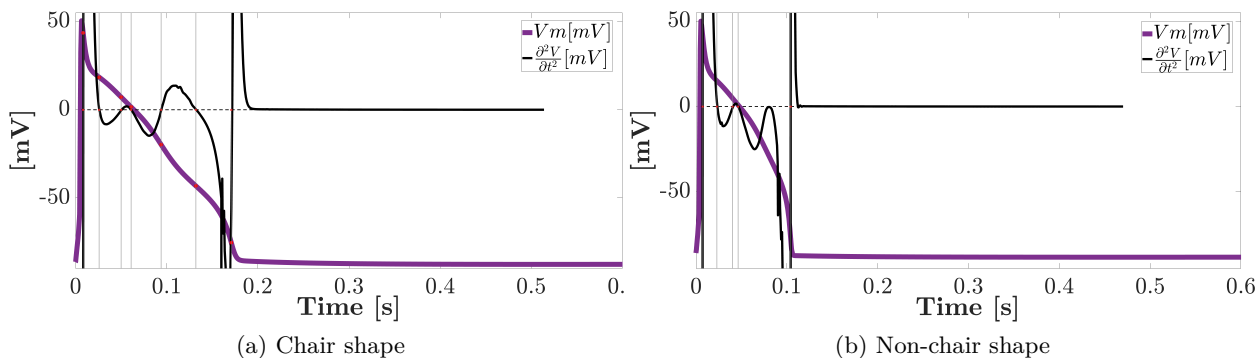
Figure 4.7: Atrial Paci2013 performed with additional O'Hara Rudy I_{K1} formulation

(a) Chair shape   (b) Non-chair shape
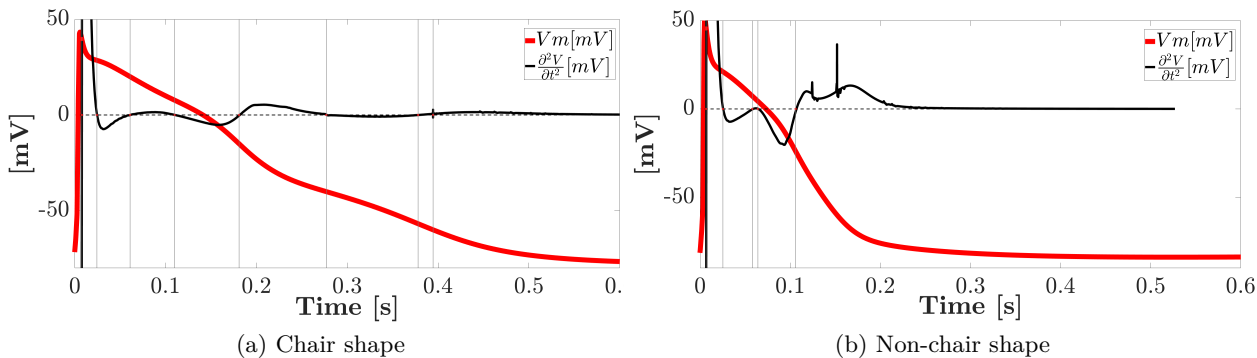
Figure 4.8: Atrial Paci2013 performed with additional Koivumäki I_{K1} formulation

4.4.2 Threshold research

This mathematical description of the phenomenon makes the virtual dynamic clamp a powerful tool to investigate the correlation between the injected quantity and the AP morphology.

Considering that DC injects an external current, it seemed a reasonable desire to add as little current as possible. The aim is now to use the previous criterion to estimate the minimal amount of injected I_{K1} required to obtain a physiological AP. Using the previous AP morphology classification, we defined for every normalized I_{K1} formulation the **threshold conductance** G_{K1}^{th} as the minimal nominal conductance required for obtaining a physiological AP (i.e. to suppress the non-physiological AP morphology). To gain a better understanding, we also considered the **threshold percentage** of the normalized I_{K1} current for each tested I_{K1}.

These threshold parameters rightly could be seen as an estimation of current formulation efficacy inside the DC technique.

In order to reach this target, we inspected percentages of injected current between 100% and 1000% of the normalized formulation, corresponding to different values of the maximal conductance $g_{K1} \in [G_{K1}, 10 \cdot G_{K1}]$, with an accuracy of $0.01 nS/pF$.

Simulations were performed for 700 seconds, reaching the steady state, with pacing at $1 Hz$. The stimulation protocol is the same used in the original paper of Paci2013, [85]: constant pacing rate of 1 Hz with depolarizing current pulses of 5 ms duration and variable amplitude (550 pA for densities lower than 100%, 750 or 950 pA otherwise). After 700 s more of stimulation, one AP is extracted and the number of inflection is computed in that interval. A visual report is presented in Figures 4.9 and 4.10.

Ventricular-like formulations   Some needed preliminary simulations highlighted that the standard stimulation protocol fails for the literature normalized current density. In such cases, the lower bound for these models was set to a higher percentage.

A specific range is then needed for the O'Hara-Rudy formulation in AL hiPSC-CMs. The number of inflections did not decrease in the desired interval and the upper bound of 1000% of the normalized current did not suppress the non-physiological AP morphology. Values were increased up to the threshold percentage, equal to 1377%.
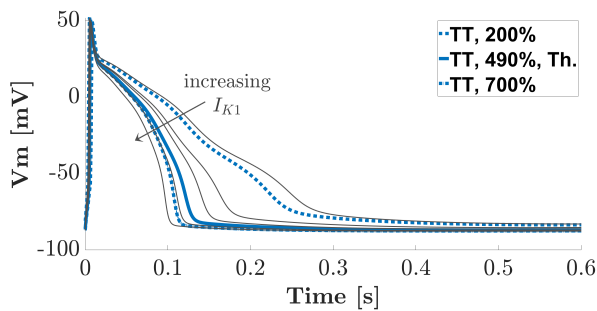
(a) TT I_{K1} in Atrial-like hiPSC-CM
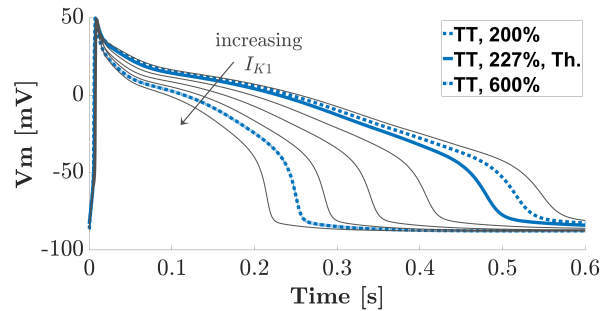
(b) TT I_{K1} in Ventricular-like hiPSC-CM
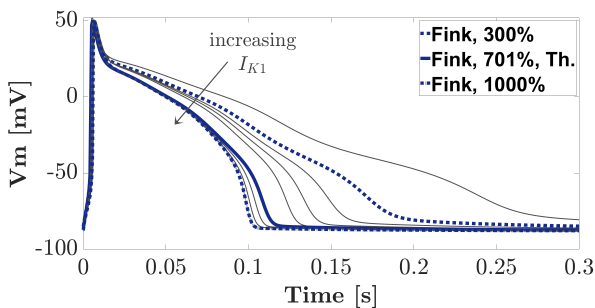
(c) Fink I_{K1} in Atrial-like hiPSC-CM

(d) Fink I_{K1} in Ventricular-like hiPSC-CM

(e) Grandi I_{K1} in Atrial-like hiPSC-CM

(f) Grandi I_{K1} in Ventricular-like hiPSC-CM

(g) ORd I_{K1} in Atrial-like hiPSC-CM
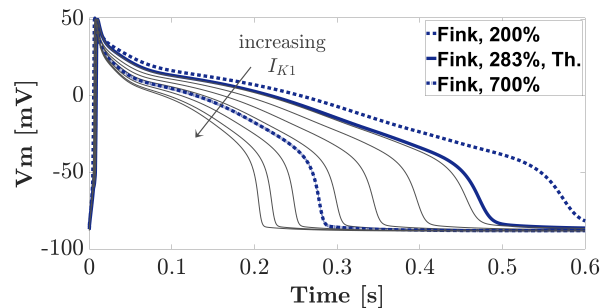
(h) ORd I_{K1} in Ventricular-like hiPSC-CM
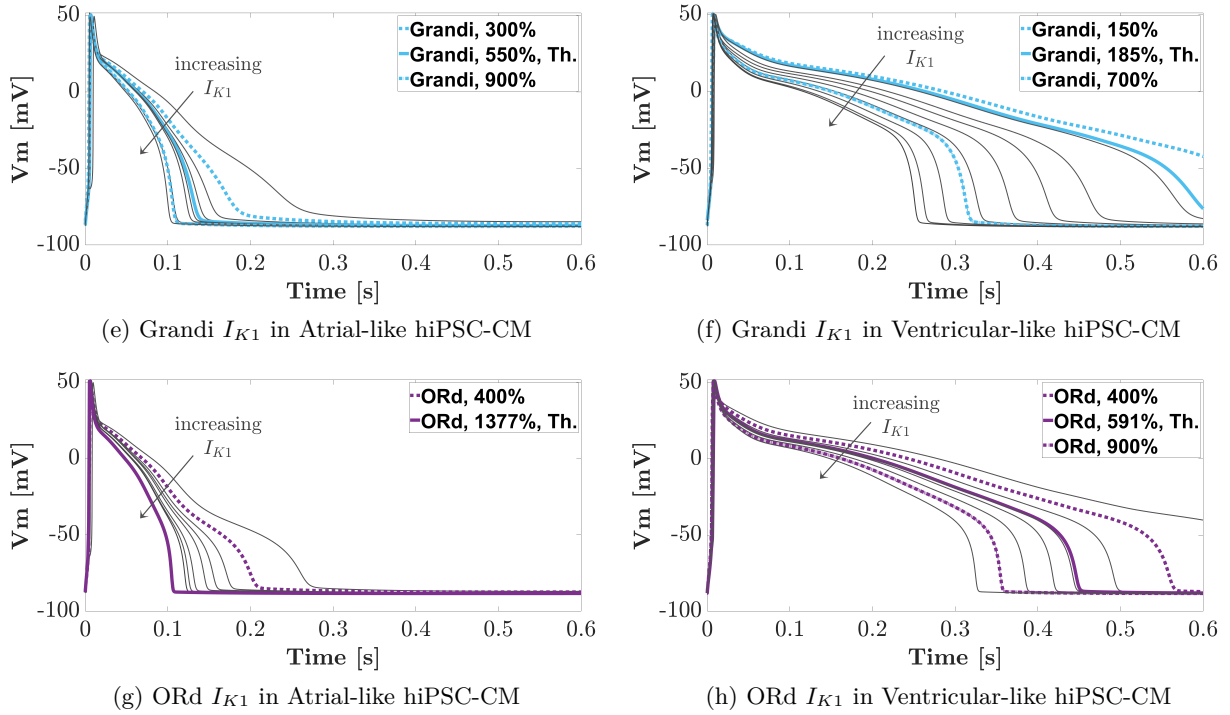
Figure 4.9: Virtual DC performed on Paci2013 considering ventricular I_{K1} formulations. Three different current densities were expressed in each figure, labeled as percentages of the normalized currents.

Atrial-like formulations   Being consistent with Figure 4.6, we consider in this paragraph both the human AL formulations (Koivumäki and Courtemanche) and the mixed Bett one. Preliminary analyses in these cases suggest not to discard any value in the expected range.

(a) Koivumäki I_{K1} in Atrial-like hiPSC-CM

(b) Koivumäki I_{K1} in Ventricular-like hiPSC-CM

(c) CRN I_{K1} in Atrial-like hiPSC-CM

(d) CRN I_{K1} in Ventricular-like hiPSC-CM

(e) Bett I_{K1} in Atrial-like hiPSC-CM   (f) Bett I_{K1} in Ventricular-like hiPSC-CM
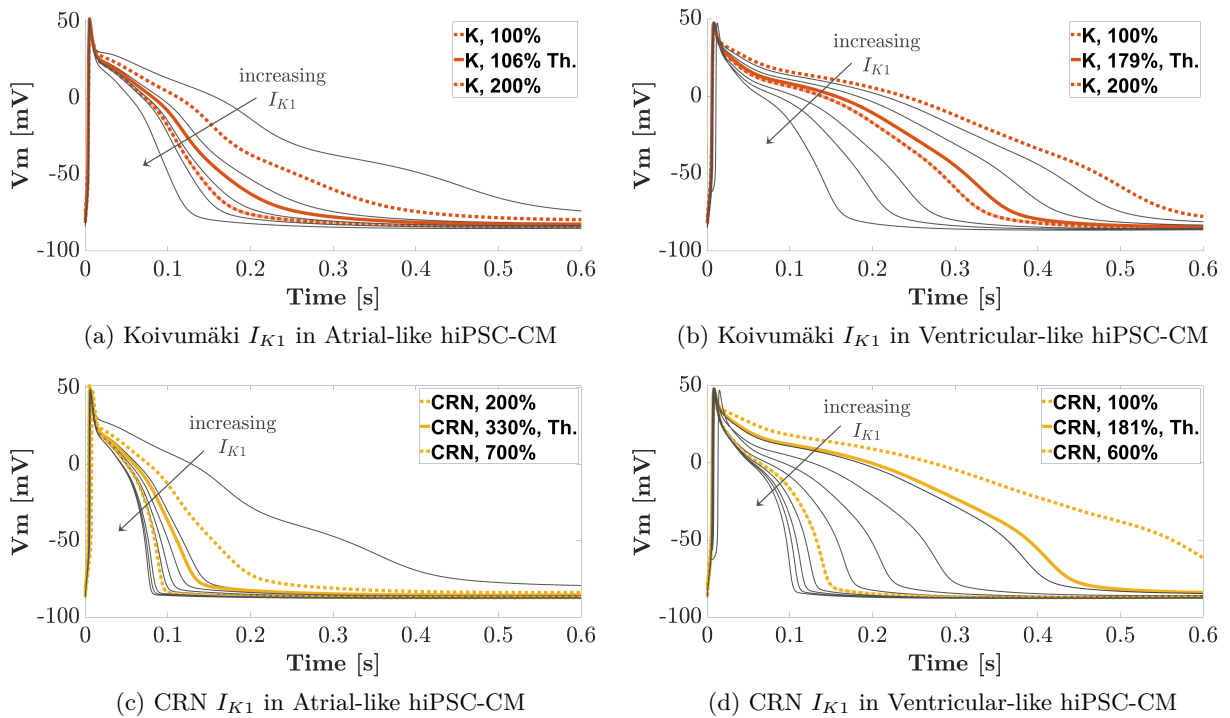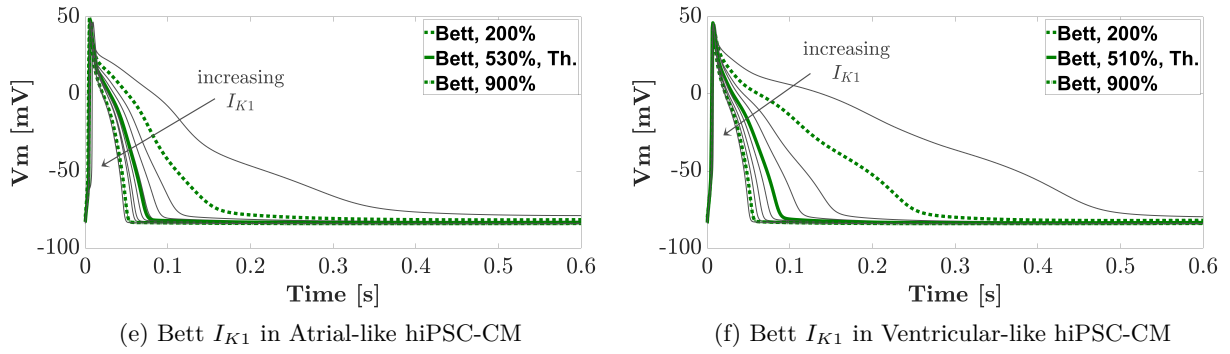
Figure 4.10: Virtual DC performed on Paci2013 considering atrial I_{K1} formulations and Bett I_{K1}. Three different current densities were expressed in each figure, labeled as percentages of the normalized currents.

4.5 Results

Once ran the simulation, we summarized the resulting threshold conductances and percentages in Table 4.1. Comparing the different results between atrial-specific I_{K1} formulations (Koivumäki, CRN) and ventricular ones, we see that for both AL and VL hiPSC-CMs, the Koivumäki and Courtemanche threshold conductances are much lower than the thresholds of the ventricular formulations.

I_{K1} formulation	G_{K1}^{th}		Threshold percentages	
	AL hiPSC-CMs	VL hiPSC-CMs	AL hiPSC-CMs	VL hiPSC-CM
Ten Tusscher	9.0336	4.1855	490	227
Fink	2.3693	0.9410	701	283
Grandi	2.2761	0.7659	550	185
O'Hara-Rudy	1.8066	0.7754	1377	591
Koivumäki	0.0742	0.1253	106	179
Courtemanche	0.3297	0.1738	330	181
Bett	1.9518	1.8782	530	510

Table 4.1: Conductance G_{K1}^{th} threshold nominal values, measured in $[nS/pF]$, and percentages of the injected current required to obtain a physiological AP for each model, for both AL (second and fourth columns) and VL (third and fifth columns) hiPSC-CMs.

In Figure 4.11 we provided a visual report of the threshold percentages of the normalized I_{K1} current in each original model for each tested I_{K1}. Once more, ventricular formulations need higher percentages of injected current than atrial formulations in order to prevent the cell from showing a non-physiological morphology.

A common feature among the different I_{K1} formulations is the increased current density needed by AL cells with respect to VL hiPSC-CMs. Again, the discrepancy decreases when considering the Koivumäki or Courtemanche I_{K1} formulations.

First criterion Since DC injects an external current, it is reasonable to add a current as small as possible. Under this assumption, rightly injected threshold current could be seen as an
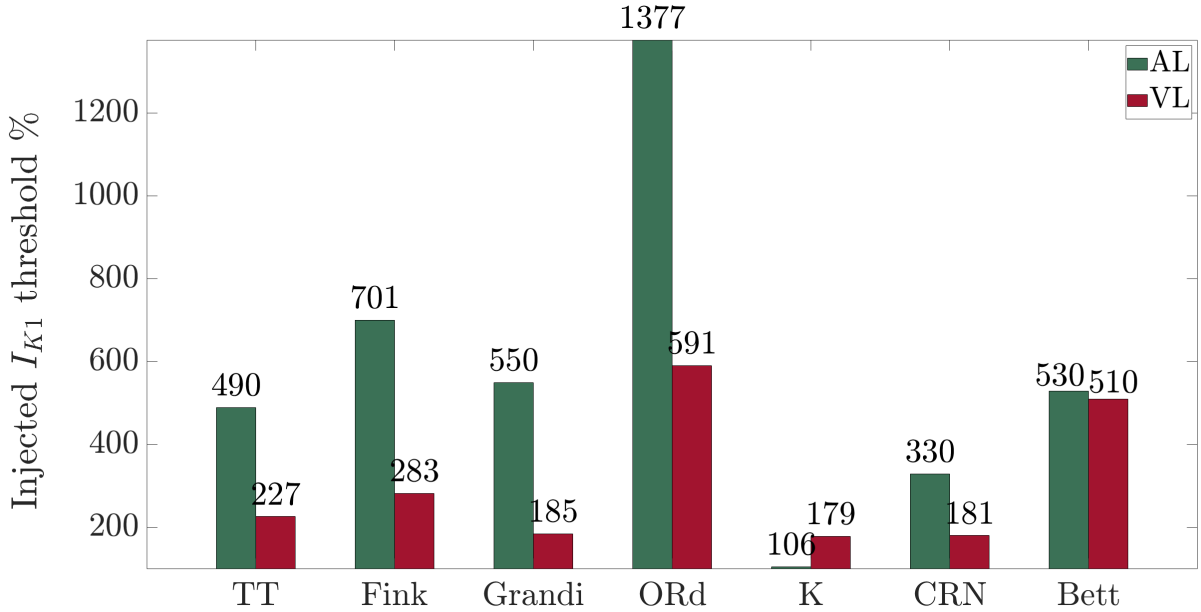
Figure 4.11: Threshold percentages of the normalized I_{K1} current in each original model, for both AL or VL hiPSC-CMs.

estimation of the efficacy of the I_{K1} current formulation inside the DC technique.

When considering VL hiPSC-CMs, almost every I_{K1} formulation needs a current density lower than 3 times the normalized current density in the literature, i.e. the I_{K1} threshold percentage is lower than 300%. On the other hand, for every tested formulation, the AL simulation shows a physiological morphology when the injected current density reaches higher percentages, and almost every I_{K1} formulation needs a current density higher than 3 times the normalized literature value, i.e. the threshold percentage is higher than 300%.

Second criterion   A second possibility is to consider some specific biomarkers as a tool to discriminate between different formulations. In this specific case, the most suitable biomarker seems to be the APD_{90}, as a pointer to the duration and length of the action potential and highly related to the chair-shape morphology definition.

For each model, we have evaluated the AP duration at 90% of repolarization at different percentages of the injected I_{K1} including the threshold percentage (Table 4.2); Figure 4.12 shows the decreasing trend of the curves. These values should be compared with some experimental data, and we referred to the APD_{90} measurements described in Table 2 of the original Paci2013, [85]. For ventricle hiPSC-CMs, the experimental APD_{90}, equal to 414.7 ± 21.8 ms, is a target that both atrial-like (CRN) and ventricular-like (ORd) formulations can reach. On the other hand, this biomarker becomes a discriminant value for AL cells, where the only Koivumäki I_{K1} formulation can reach the target APD_{90} equal to 286.2 ± 21.2 ms. Figure 4.12 shows the distance of different models from the experimental value and the Koivumäki threshold APD_{90} inside the confidence rate.
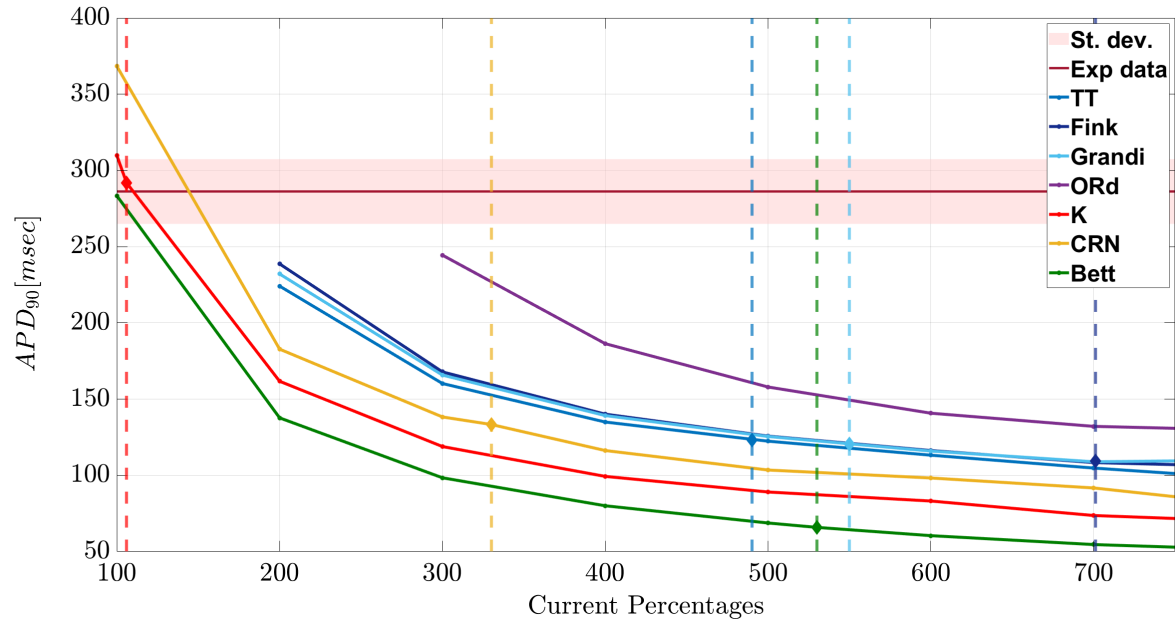
Figure 4.12: APD90 with respect to the injected current percentages in AL hiPSC-CMs. For each I_{K1} formulation, the threshold percentages have been highlighted (dashed line) and the intersection point can be compared with the experimental APD_{90}.

I_{K1} formulation		TT	Fink	Grandi	ORd	K	CRN	Bett
Threshold APD_{90}	AL hiPSC-CM	123.3	109.5	120.6	101.7	291.9	133.4	65.9
	VL hiPSC-CM	480.8	466.3	591.6	430.3	344.6	429.4	80.5

Table 4.2: Threshold AP duration at 90% of repolarization considering each I_{K1} formulation, injected both in AL and in VL hiPSC.CMs.

Conclusions Keeping in mind that the DC technique is used as a tool to improve action potential measurements in AL hiPSC-CMs, we focused on the effects of I_{K1} injection on AL hiPSC-CMs action potential morphology. Previous results and considerations led us to the statement that atrial current formulations, i.e. Koivumäki and Courtemanche, are preferable to the ventricular ones. In agreement with this, Figure 4.11 shows that VL hiPSC-CMs reveal the VL phenotype for low densities independent of the I_{K1} formulation. On the other hand, AL phenotype was easily revealed using only atrial I_{K1} formulations, by using 106% (Koivumäki) and 300% (Courtemanche) of the original normalized literature values, respectively.

In conclusion, in order to characterize atrial-specific hiPSC-CMs using the minimal injection of I_{K1}, virtual dynamic clamp suggests Koivumäki I_{K1} as the more reliable I_{K1} formulation, with the minimum current density equal to 106% and 179% for AL cells and VL cells, respectively.

This work has been presented to the International Conference of Computing in Cardiology and the relative paper *Numerical Simulations Indicate IK1 Dynamic Clamp Can Unveil the Phenotype of Cardiomyocytes Derived from Induced Pluripotent Stem Cells*, [15], is in press.

Chapter 5

Novel *in-silico* model for atrial-like hiPSC-CMs

Atrial fibrillation (AF) is a multifactorial disease, affecting almost 33 million people globally, with prevalence in the European population. It is characterized by an irregular atrial rhythm and available rhythm control strategies are inadequate, showing a limited efficacy and causing undesirables adverse effects (such as ventricular proarrhythmia). Thus, the best current option to treat the disease is the interventional therapy, namely ablation, [24]. The major limitation that hampers the drug development is the critical assessment of human atrial CMs and their proliferation propagation in culture, moreover when antiarrhytmics drugs are injected, acting in the direction of AP shortening in terms of action potential duration. As a result, the development of pharmacological therapies needs a better understanding of the basic aetiology and physiological mechanism of AF.

hiPSC may offer a platform to develop new strategies and evaluate drugs, but cultures enriched in AL CMs are needed. Current protocols for hiPSC differentiation result in pool with small percentages of AL-CMs, but different studies suggest retinoic acid (RA) to drive cells towards an atrial fate displaying electrophysiological properties and gene expression patterns characteristic of early AL myocytes, as describe in the previous chapter and in [55].

The clear importance of AL hiPSC-CMs highlights the relevance of studying the function of these cells also *in-silico*. The only existing AL model was published in 2013 but did not consider any atrial specific current. Furthermore CardioCentro Ticino - EOC focused on cell differentiation and new data and insights are now available. The ultra rapid activating delayed rectifier current, absent in the ventricle, induces a less pronounced plateau phase; I_{K1} density and rectification are lower in human atrial cells, leading to a slow late repolarization in phase 3 and slower AP upstroke.

This is the reason why we started developing a new computational model for atrial-like hiPSC-CMs, reproducing all these features.

Model parameters were calibrated and optimized using different experimental data set. The heterogeneity of phenotypes in the pull of retinoic-acid treated cells prevents electrophysiologists to discriminate *a priori* the AP morphology of the cell. As discussed in the previous chapter, the
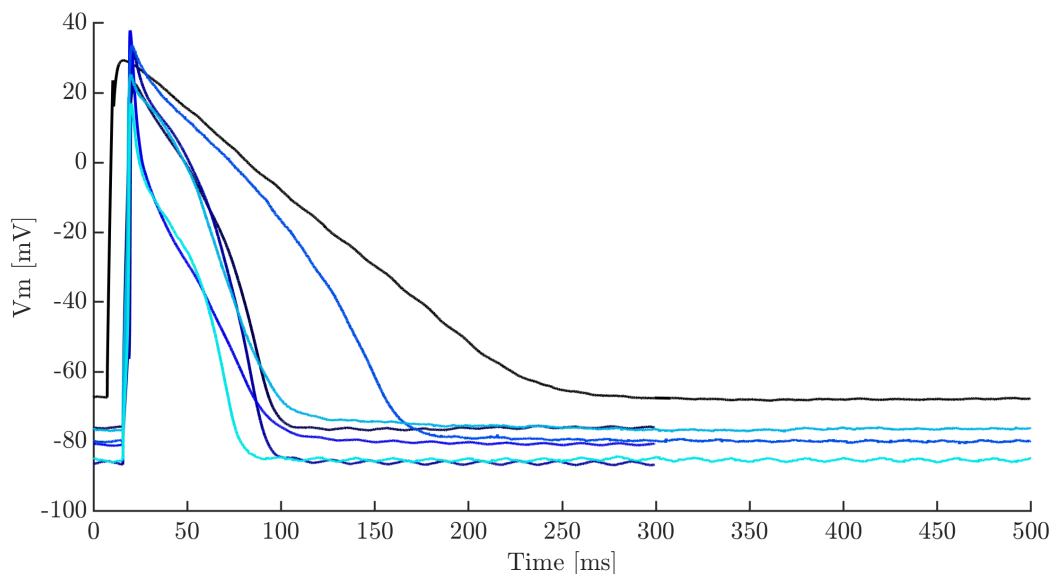
Figure 5.1: Experimental action potentials recorded by the CardioCentrum Ticino Institute.

dynamic clamp technique can unveil the hiPSC-CM phenotype, but experimental conditions and protocols for the treatement of cell hamper subsequent manipulations, leading a lack of voltage clamp data and current specific measurements.

Moreover, the dynamic clamp technique is based on the injection of an external stimulus and any spontaneous beating cell can be classified as AL. Thus, we base on two different datasets.

First of all, with regard to spontaneous beating hiPSC-CMs we referred to the only available data biomarkers of Ma et al., previously used to fit the Paci generation models, [66].

Indeed, considering paced CMs we referred to the recent CCT data, used in their latter published paper [2]. Two partitions of these data are presented: the first one is a set of seven AP traces (see Figure 5.1), measured in current clamp; the second one is a pool of 8 biomarkers per cells, (see Table 5.1). Such data had already been analyzed and used as target in the unsupervised learning algorithm to classify the recorded cells, [2].

Different AP parameters have been presented in Chapter 3, but some additional information have been considered:

$MDP + DC$	is the maximum diastolic potential obtained after the DC injection of additional I_{K1}
$APD_{20/90}$	defined as the ratio between APD_{20} and the $ADPD_{90}$ is the target used to evaluate the triangulation of the AP shape, considering 0.44 as the cut-off value between AL and VL.

Upon these sample a statistical analyses was conducted considering the mean, the standard deviation (Dev. St.) and the standard error of the mean (Sem).

Cell number	Biomarkers							
	MDP	$MDP + DC$	APD_{90}	APD_{20}	APD_{50}	$APD_{20/90}$	V_{max}	APA
1	-24	-75.25	94.84	28.30	53.49	0.298	127.5	83.39
2	-33	-80.18	54.01	5.88	21.811	0.10	156.6	114.12
3	-36	-76.49	91.13	15.3	44.28	0.168	66.280	100.60
4	-30	-77.212	65.08	11.6	33.439	0.179	124.27	105.26
5	-41	-83.99	40.95	7.56	23.817	0.184	88.316	104.91
6	-23	-77.437	87.46	12.29	58.209	0.140	105.32	103.64
7	-20	-84.67	40.388	7.988	24.049	0.197	111.68	112.16
8	-28	-83.25	149.75	40.01	110.84	0.2671	191.87	124.86
9	-31	-83.09	89.06	19.251	60.88	0.216	223.90	127.93
Statistical values								
Mean	-25	-80.91	70.72	12.176	39.544	0.167	154.96	111.24
Dev. St.	16	3.156	33.41	9.036	22.79	0.058	51.49	12.12
Sem	3.79	0.744	7.87	2.12	5.373	0.0138	12.14	2.86

Table 5.1: Recorded experimental biomarkers yielded from electrophysiological recordings of 9 cells. A bigger set of 18 cells has been considered to obtain the statistical values, where Dev.St. is the standard deviation and Sem is the standard error of the mean.

5.1 First parameter switch in Paci2020

Paci2020 model, the latest ventricular-like version, is the ground chosen to start developing the first AL hiPSC-CM model. Firstly, experimental conditions were reformulated to reflect the corresponding laboratory setup. Thus, two different specific datasets were used for unpaced and paced conditions. Indeed, experimental data that refers to Ma et al. recordings were collected considering an external potassium concentration K_o equal to 5.4 mM, while recent CCT data considered an external potassium concentration K_o equal to 4.0 mM. As shown in Figure 5.2, this change leads to a more hyperpolarized resting potential and a higher action potential duration. To sum up, physiological values

Figure 5.2: Changes affecting the AP when considering two different external potassium concentrations: $K_o = 5.4mM$ (dashed line), $K_o = 4.0mM$ (solid line).

for both paced and unpaced configurations are written in Table 5.2.

As a first step towards the atrialization we applied some parameters rescaling, where factors are provided by the literature and summarized in Table 1 of Paci2013, [85]. There, two different sets can be identified. In the first one a specific relation is given between ventricular- and atrial- like phenotype, some derived from human models, some scaled coherently with the membrane capacitance measured in the experiments C_m. The corresponding scaled value in Paci2020 is now the ventricular parameter, [82] used to evaluate the atrial like parameter, [85]. These changes are listed in Table

5.3.

The second set is made up by parameters for which the characterization of atrial and ventricular phenotype values was based in 2013 on the basic fitting parameters scaling, where the latter numbers were obtained by the fitting of heterogeneous experimental data. However, any basic fitting parameter was available and the Paci2020 values can be considered as ventricular-like parameters. Thus, given

Parameter	Unpaced	Paced
T	310 K	310 K
K_o	5.4 mM	4.0 mM
Na_o	151.0 mM	151.0 mM
Ca_o	1.8 mM	1.8 mM
K_i	150.0 mM	150.0 mM
E_K	-88.8 mV	-96.8 mV

Table 5.2: Physiological conditions considering Ma et al. (first column) and Cardiocentro Ticino (second column) laboratories setup.

- α the unknown basic fitting value, α_v and α_a the ventricular and atrial values

- $f : \alpha \mapsto \alpha_v, \quad g : \alpha \mapsto \alpha_a$ the maps between parameters

We obtained α_a by rescaling an hypothetical fitting parameter on a mixed pull of cells. In this case we need to proceed by steps.

$$\alpha = f^{-1}(\alpha_v)$$
$$\alpha_a = g(\alpha)$$

These changes are listed in Table 5.4. One more current (I_f) was taken into account in Paci2013 model, but occurred $G_{f,v} = G_{f,a}$, thus we did not write it down.

AP changes due to the parameters switch can be seen in Figure 5.3: a qualitative comparison between the simulated APs allows us to say that the model still reproduces the main differences between the VL and AL hiPSC-CMs reported in literature. That are, for instance, higher frequency of firing (shorter cycle length) for the AL parameters (see Figure 5.3a); a longer *APD* and greater *APA* for the VL model (see Figure 5.3b); a more triangular shape.

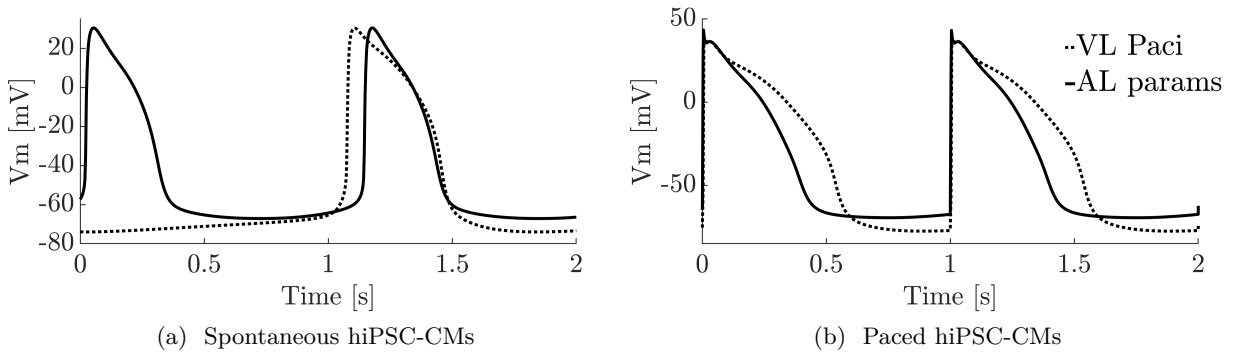(a) Spontaneous hiPSC-CMs

(b) Paced hiPSC-CMs

Figure 5.3: Qualitative differences in the AP morphology considering different sets of parameters: VL parameters (dashed line) are from Paci2020, AL parameters (solid line) were computed in Tables 5.3-5.4.

	Year	VL parameter	AL parameter	Units
I_{NaCa}	2020	$K_{NaCa,v} = 6514.47574$	$K_{NaCa,a} = 0.5 * K_{NaCa,v} = 3257.2$	A/F
I_{NaK}	2020	$PNaK_v = 2.74240$	$PNaK_a = 0.8 * PNaK_v = 2.1939$	A/F
I_{up}	2020	$V_{up,v} = 0.82205$	$V_{up,a} = 0.3924 * V_{up,v} = 0.3226$	mM/s
I_{rel}	2020	$g_{irel,v} = 55.808061$	$g_{irel,a} = 1.1109 * g_{irel,v} = 75.4190$	mM/s
V_c	2013/2020	$V_{c,v} = 8800$	$V_{c,a} = 7200$	μm^3
V_{SR}	2013/2020	$V_{SR,v} = 583.728$	$V_{SR,a} = 465.199$	μm^3

Table 5.3: Comparison of the first set of parameters which are different between the VL and AL models. In the first column we report the parameter affected by the change. In the second column we report the year of the Paci generation model that provided the VL value. In the third and fourth columns we write down the tuning of the parameters to reproduce the heterogeneity between AL and VL cells.

	Year	Param.	Basic fitting	VL parameter	AL parameter	Units
I_{Na}	2020	$\alpha = G_{Na}$	$\alpha = \alpha_v/0.58$	$\alpha_v = 64471.1896$	$\alpha_a = 1.05 * \alpha = 116720$	S/F
I_{CaL}	2013/2020	$\alpha = Vh_d$	$\alpha = -9.1$	$\alpha_v = -9.1$	$\alpha_a = \alpha + 3.114 = -5.986$	mV
	2013/2020	$\alpha = Vh_f$	$\alpha = -26$	$\alpha_v = -26$	$\alpha_a = \alpha + 0.774 = -25.226$	mV
	2013/2020	$\alpha = Vh_{f2}$	$\alpha = -32$	$\alpha_v = -32$	$\alpha_a = \alpha + 0.774 = -31.226$	mV
	2013/2020	$\alpha = \tau_{f2}$	α	$\alpha_v = \tau_{f2}$	$\alpha_a = \alpha$	ms
I_{to}	2020	$\alpha = G_{to}$	$\alpha = \alpha_v/0.5$	$\alpha_v = 29.9038$	$\alpha_a = \alpha = 59.8076$	S/F
I_{K1}	2020	$\alpha = G_{K1}$	$\alpha = \alpha_v/1.1$	$\alpha_v = 28.1492$	$\alpha_a = 0.75 * \alpha = 19.1926$	S/F
C_m	2020	$\alpha = C_m$	$\alpha = \alpha_v/1.113$	$\alpha_v = 98.7109$	$\alpha_a = 0.887 * \alpha = 78.6672$	pF

Table 5.4: Comparison of the first set of parameters which are different between the VL and AL models. In the first column we report the current affected by the parameter changed (see column 3). In the second column we report the year of the Paci generation model that provided the VL value. In the fifth column the ventricular value given by Paci2020, in the fourth, the hypothetical basic fitting parameter. In the last column the final AL tuned parameter.

5.2 Additional atrial-specific currents

In the last decade a multitude of models were published to describe atrial cell electrophysiology. Firstly, two principles atrial-specific lineages where published in 1998 by Courtemanche et al., [22] and Nygren et al., [77]. These models have been extended later, as described in Figure 5 of [133] with the introduction of ion currents not incorporated previously. Among all of them, five models were benchmarked by Wilhelms et al. in [138].

Since we are interested in developing a hiPSC-CMs atrial model, we took into account each ion current that is only expressed in the atria. Such currents are summarized in Table 2 of [133] and they always deal with various potassium channels. They are: I_{Kur}, $I_{K,ACh}$, I_{K2P}, I_{kCa}.

Acetylcholine-sensitive potassium current ($I_{K,ACh}$) is an atrial specific current activated by the neurotransmitter acetylcholine (ACh) after the binding to the specific muscarinic receptor.

For this reason its contribution to the AP in in vitro isolated hiPSC-CMs can be neglected. hiPSC actually never live in a human body, so we consider modeling that current a useful project.

The other current we decided not to take into account is the Two-pore-domain potassium ($K_{2P}3.1K^+$) current. Indeed, I_{K2P} is positively modulated in Schmidt's model, [111], in the paroxysmal atrial fibrillation model and overexspressed in the chronic model. However in basal conditions the current does not concur in the electrical activity of a healthy patient with sinus rhythm.

5.2.1   Ultrarapid delayed rectifier current formulations

The first typical current we want to model is the *ultrarapid outward current*, I_{Kur}, typical of atrial like cardiomyocytes. Two different pedigrees provided a specific formulation: Courtemanche lineage and Nygren one in the upgrade of Maleckar.

Maleckar model

The first formulation we take into account is the one used by Koivumäki in 2011, that corresponds to the Maleckar formulation. We take into account the set of equations proposed in the paper of 2009, [71].

First of all, we compare the compatibility between models in term of unit of measurements. Paci models is tuned using time in *seconds* and voltage in *milliVolt* (V_m stands for *voltage in mV*), while Maleckar (Mal.) is formulated in *second* and *Volt*. In both models capacitance is in *pF*. For the compatibility we need to use

$$V_m = 1000 \times V_{Maleckar}.$$

The other relevant constant in the potassium formulation is the universal gas constant, measured in $mJ/(mol \cdot K)$ in Maleckar and in $J/(mol \cdot K)$ in Paci. Once more, for the exact compatibility we need

$$R_{Mal.} = 1000 \times R \Rightarrow E_{K,Mal.} = 1000 \times E_K.$$

With these notes we can write the following I_{Kur} formulation

$$I_{Kur} = g_{Kur} \cdot a_{ur} \cdot i_{ur} \ (V_m - E_K \cdot 10^3). \tag{5.1}$$

The current dynamic is defined by two specific gating variables, a_{ur}, i_{ur}, with an Hodgkin-Huxley first order dynamic.

$$
\begin{aligned}
a_{ur,\infty} &= \frac{1.0}{1.0 + \exp{-\frac{V_m \cdot 10^3 + 6.0}{8.6}}} & i_{ur,\infty} &= \frac{1.0}{1.0 + \exp{\frac{V_m + 7.5}{10.0}}} \\
\tau_{aur} &= \frac{0.009}{1.0 + \exp{\frac{V_m + 5.0}{12.0}}} + 0.0005 & \tau_{iur} &= \frac{0.59}{1.0 + \exp{\frac{V_m + 60.0}{10.0}}} + 3.5 \\
\frac{da_{ur}}{dt} &= \frac{a_{ur,\infty} - a_{ur}}{\tau_{aur}} & \frac{di_{ur}}{dt} &= \frac{i_{ur,\infty} - i_{ur}}{\tau_{iur}}
\end{aligned}
\tag{5.2}
$$

The conductance in Maleckar formulation is $g_{Kur,Mal} = 2.25nS$, we have to scale in nS/pF. Thus, we find

$$g_{Kur} = \frac{g_{Kur,Mal}}{C_{m,Mal}} = \frac{2.25}{50} = 0,045 \left[\frac{nS}{pF} \right] \tag{5.3}$$

Finally, initial conditions for the new gating variables are

$$a_{ur} = 3,6700 10^{-4} \qquad i_{ur} = 0,9673 \tag{5.4}$$

With this additional I_{Kur} formulation the resulting action potential morphology is described by Figure 5.4.

(a) Unpaced simulation

(b) Paced simulation

Figure 5.4: Steady-state simulation of the model with the additional I_{Kur} Maleckar current, performed in unpaced conditions and under a pacing protocol at 1Hz

Courtemanche model

The second formulation we take into account is the one used by Courtemanche in the primitive model of 1998, [22].

As described in the previous paragraph, we compare the compatibility between models in term of measurements units. Paci models is tuned using time in *seconds* and voltage in *milliVolt*, while Courtemanche (CRN) is formulated in *second* and *Volt*. In both models capacitance is in pF. For the compatibility we need to use

$$V_m = 1000 \times V_{Courtemanche}.$$

The other relevant constant in the potassium formulation is the Faraday constant, measured in

C/mmol in Courtemanche and in *C/mol* in Paci. Once more, for the exact compatibility we need

$$F = 1000 \times F_{CRN} \Rightarrow E_{K,CRN} = 1000 \times E_K.$$

With these notes we can write the following I_{Kur} formulation, where g_{Kur} is the conductance:

$$I_{Kur} = g_{Kur} \cdot u_a^3 \cdot u_i \cdot \left(V_m - E_K \cdot 10^3 \right)$$
$$g_{Kur} = 0.005 + \frac{0.05}{1.0} + \exp\left(-\frac{V_m - 15.0}{13.0} \right) \tag{5.5}$$

The current dynamic is defined by two specific gating variables, u_a, u_i, with an Hodgkin-Huxley first order dynamic described by the following equations, where $K_{Q,10} = 3$:

$$\alpha_{u(a)} = 0.65 \left[e^{-\frac{V_m+10.0}{8.5}} + e^{-\frac{V_m-30.0}{59.0}} \right]^{-1}$$

$$\beta_{u(a)} = 0.65 \cdot \left[2.5 + \exp\left(-\frac{V_m + 82.0}{17.0} \right) \right]^{-1}$$

$$\tau_{u(a)} = \frac{K_{Q,10}}{\alpha_{u(a)} + \beta_{u(a)}}$$

$$\frac{du_a}{dt} = \frac{u_{a(\infty)} - u_a}{\tau_{u(a)}}$$

$$u_{a(\infty)} = \left[1.0 + \exp\left(-\frac{V_m + 30.0}{9.6} \right) \right]^{-1}$$

$$\alpha_{u(i)} = \left[21.0 + e^{-\frac{V_m-185.0}{28.0}} \right]^{-1}$$

$$\beta_{u(i))} = \exp\left(-\frac{V_m + 158.0.0}{16.0} \right)$$

$$\tau_{iur} = \frac{K_{Q,10}}{\alpha_{u(i)} + \beta_{u(i)}}$$

$$\frac{du_i}{dt} = \frac{u_{i(\infty)} - u_i}{\tau_{u(i)}}$$

$$u_{i(\infty)} = \left[1.0 + \exp\left(-\frac{V_m - 99.45}{27.48} \right) \right]^{-1}$$

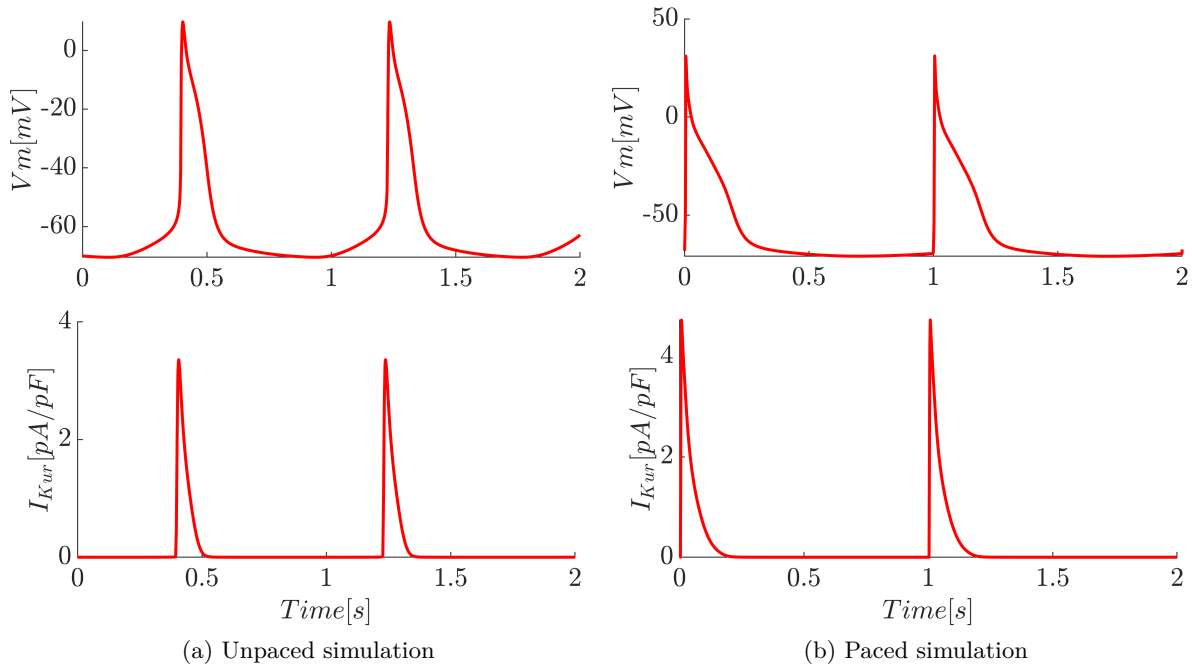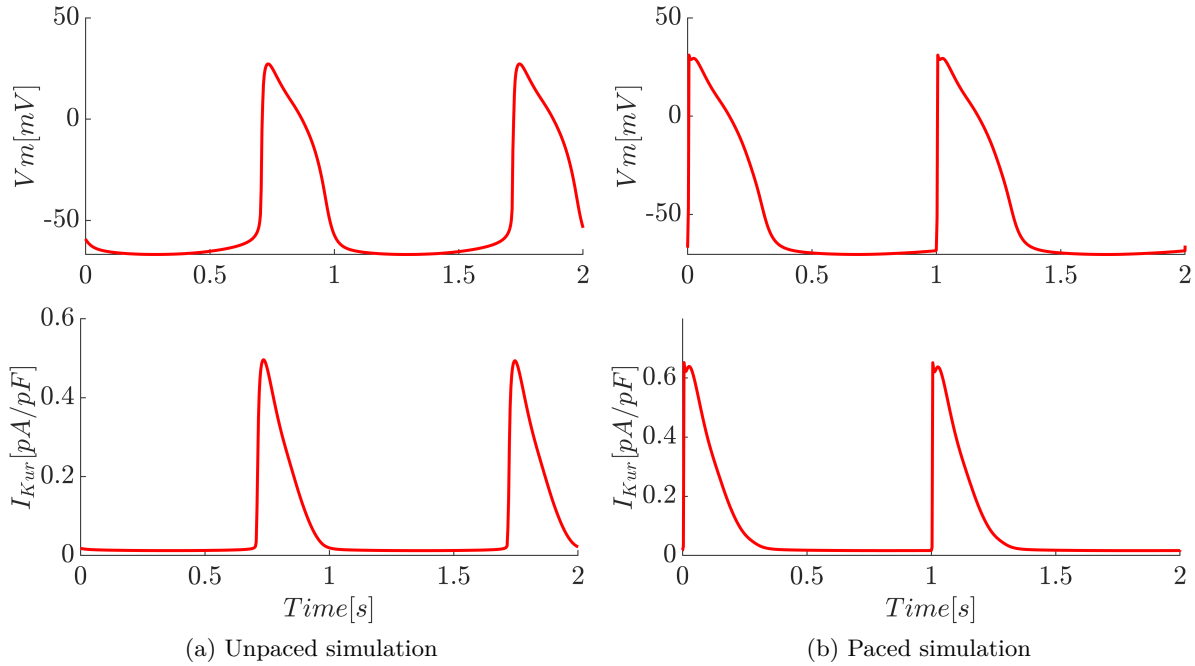(a) Unpaced simulation   (b) Paced simulation

Figure 5.5: Steady-state simulation of the model with the additional I_{Kur} Courtemanche current, performed in unpaced conditions and under a pacing protocol at 1Hz

Finally, initial conditions for the new gating variables are

$$u_a = 9.99 \cdot 10^{-1} \qquad u_i = 4.96 \cdot 10^{-3} \qquad (5.6)$$

With this additional I_{Kur} formulation the resulting AP morphology is described by Figure 5.5.

Comparison

The idea is to compare the different formulations of the new atrial model, in order to analyse differences and effects on the AP. A first comparison is given by the resulting AP waves in Figure 5.6. The main effect of the additional current is the reduction of the AP duration, matched with a reduction of the AP peak considering the I_{Kur} Maleckar formulation.

(a) Unpaced simulation	(b) Paced simulation
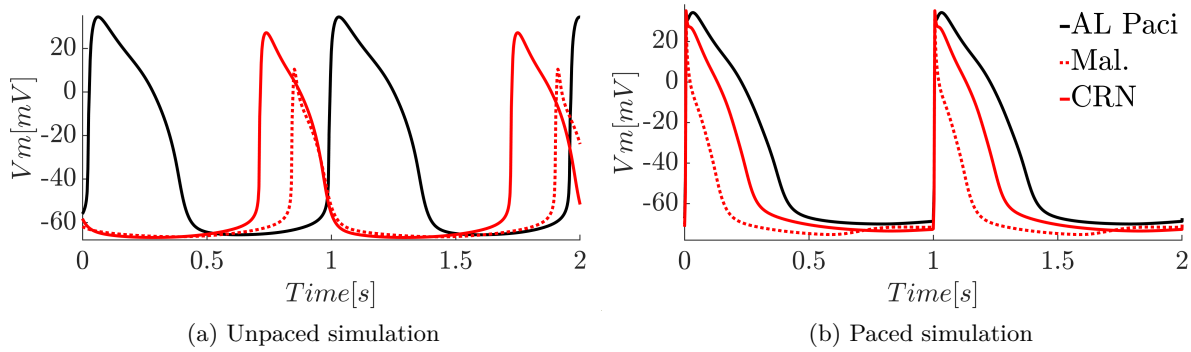
Figure 5.6: Steady-state simulation of the model considering three different formulations: the AL version of Paci2020 (black line), the additional I_{Kur} Maleckar current (dashed red line), the additional I_{Kur} Courtemanche current (solid red line).

Such results are expressed also considering some biomarkers. Actually, we considered only

	Unpaced Exp. data	Atrial Paci2020	Additional I_{Kur} Maleckar	Additional I_{Kur} Courtemanche
MDP $[mV]$	-73.5 ± 1.5	-74.858	-69.9388	-68.5498
APA $[mV]$	100.2 ± 2.1	102.030	79.5101	94.82082
$Peak$ $[mV]$	26.7 ± 1.4	27.1675	9.55838	26.26785
APD_{10} $[ms]$	60.8 ± 5.5	87.1589	14.4785	60.40387
APD_{30} $[ms]$	123.1 ± 10.3	223.993	49.6623	144.2292
APD_{90} $[ms]$	286.9 ± 21.2	390.518	138.714	274.9456
$rappAPD$	1.1 ± 0.1	2.79240	1.6364	2.152
CL $[ms]$	1200 ± 200	1713.14	814.839	1243.820

Table 5.5: Action potential features comparison

experimental data of Ma. et al, [66], because few changes have been made; thus, only unpaced conditions were taken into account. In Table 5.5 the summary of the AP parameters highlights that every biomarker gets better considering an additional atrial specific current, but the Maleckar formulation leads the model to an extreme reduction of the APD percentages, in addition to non consistent values of peak and amplitude.

5.2.2 Small conductance calcium activated potassium channel

The second additional current we take into account is the Small conductance calcium activated potassium (SK) channel I_{KCa}, presented by Skibsbye (Ski) in 2016, [117].

SK channel opening is described as a two-state Markov model. The opening of the channel simply depends on the sub-sarcolemmal calcium concentration, Ca_i^{2+} (squared). The equations proposed to define the opening of the channel are as follows:

$$
\begin{aligned}
KCa_{on} &= 47.0e6 \\
KCa_{off} &= 13.0 \\
\frac{dO}{dt} &= (1 - O) \cdot KCa_{on} \cdot Ca_i^2 - O \cdot KCa_{off}
\end{aligned}
\tag{5.7}
$$

where O is the gating variable. The resulting current equation is

$$
I_{KCa} = g_{KCa} \cdot O \cdot \frac{1}{1 + \exp(\frac{V_m - E_K \cdot 10^3 + 120.0}{45.0})}(V_m - E_K \cdot 10^3).
\tag{5.8}
$$

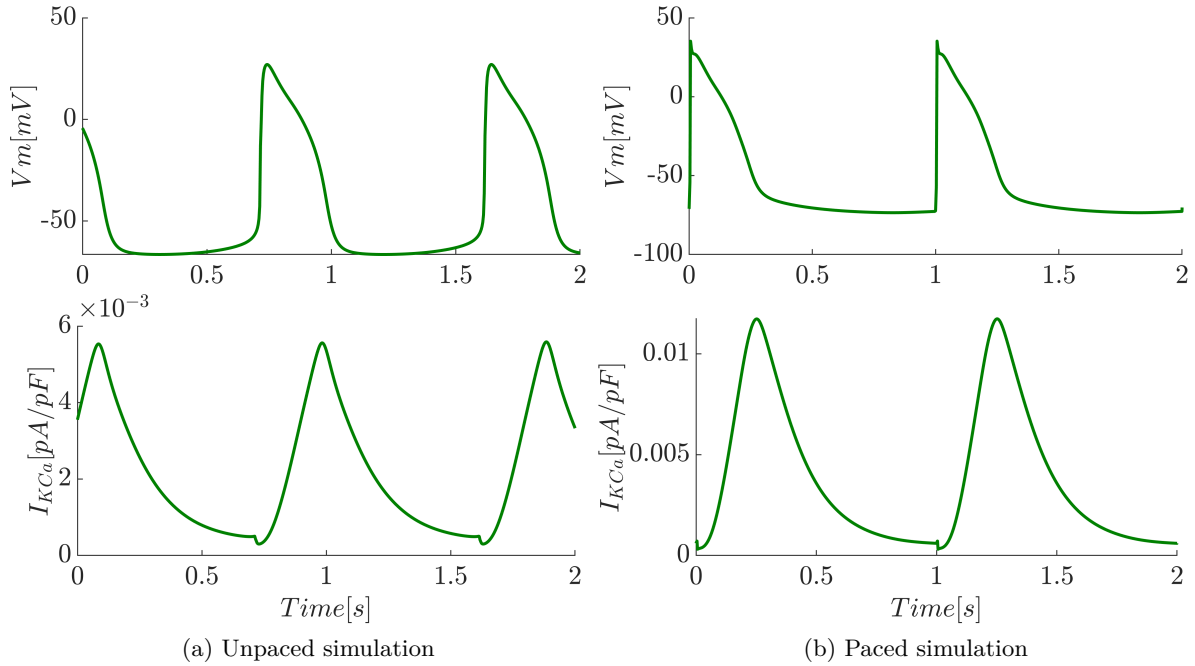(a) Unpaced simulation   (b) Paced simulation

Figure 5.7: Steady-state simulation of the model with the additional I_{KCa} Skibsbye current, performed in unpaced conditions and under a pacing protocol at 1Hz

In the equation 5.8, $g_{KCa,Ski}$ is supposed to be $g_{Kca,Ski} = 3.6nS$, thus

$$g_{KCa} = \frac{g_{KCa,Ski}}{C_{m,Mal}} = \frac{3.6}{50} = 0.072 \left[\frac{nS}{pF}\right] \qquad (5.9)$$

Resulting APs in unpaced and paced configurations are described, respectively, in Figure 5.7a and 5.7b.

5.3 Dynamic Clamp integration

For the final current adjustment we must take into account the different sources of experimental data: Ma et al. [66] for the unpaced spontaneous beating phenotype and Altomare et al. [2] for stimulated hiPSC-CMs. In this second laboratory setup, cells were treated with retinoic acid, then stimulated using the dynamic clamp protocol, as described in Chapter 4.
Untreated cells show a stable depolarized resting state, that we can reach by previously suppressing the native I_{K1} current. Furthermore, the original Paci2013 current aimed to reproduce experimental voltage clamp protocols and this allows us to replace the current formulation as long as the new one keeps the biomarkers fitting.

In order to reproduce a virtual description as much similar as possible to CCT experiments, we replaced the original I_{K1} current formulation with the one used in the laboratory protocol. Indeed, we integrated the Koivumäki (KO) I_{K1} formulation published in 2011, [47], and previously
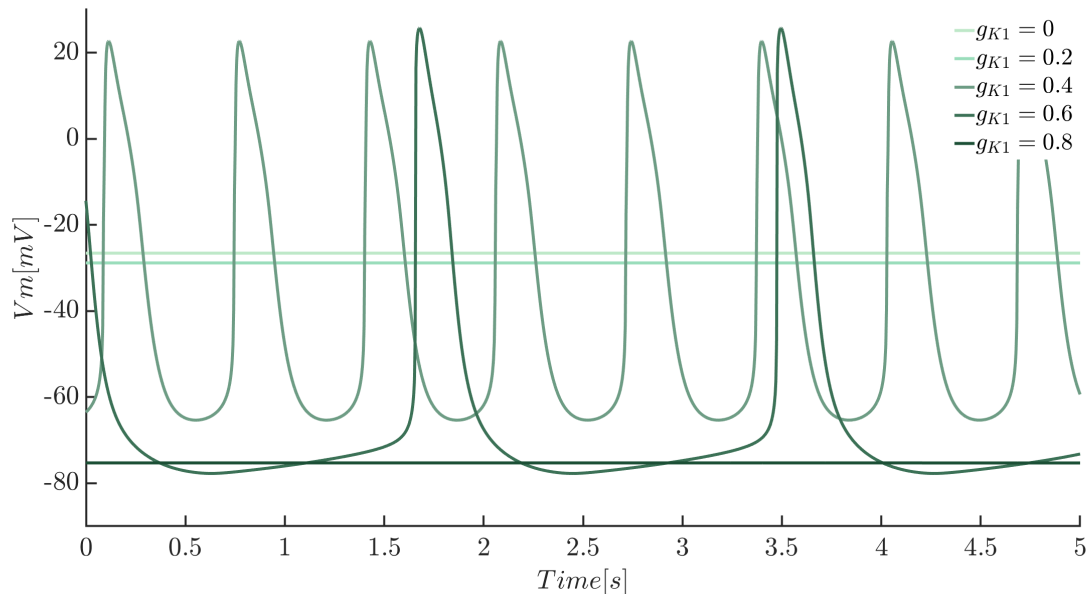

Figure 5.8: AP behaviour considering different values of the nominal g_{K1}, measured in nS/pF. Small percentages of the injected current fix the cell to a depolarized diastolic potential; increasing g_{K1} values from 0.4 to 0.6 corresponds to the increase of the spontaneous firing cycle length; for values higher than $0.07nS/pF$ the current leads the cell to an hyperpolarized MDP.

written by Nygren, [77], this one being human atrial specific, suitable for the unpaced version.

$$V_m = 1000 \times V_{Nygren}$$
$$E_K = 1000 \times E_{Nygren}$$
$$I_{K1} = g_{K1}[K^+]_o^{0.4457} \frac{V_m - E_K}{1.0 + e^{1.5(V_m - E_K + 3.6)F/RT}} \qquad (5.10)$$

where the starting nominal maximal conductance is $g_{KO} = 3.825nS$, thus

$$g_{K1} = \frac{g_{K1,KO}}{C_{m,Mal}} = \frac{3.825}{50} = 0.0765 \left[\frac{nS}{pF}\right]. \qquad (5.11)$$

Once the correct current equation had been integrated, we analysed the behaviour of the membrane voltage with respect to the maximal conductance g_{K1}, in order to replicate both the spontaneous firing for unpaced hiPSC-CMs and the stable and hyperpolarized MDP of DC treated cells. As described in Figure 5.8, we inspected conductance in the interval $[0, 0.1]$ and we can easily point out that a slightly stronger Koivumäki I_{K1} is enough to stop the spontaneous APs at $-80mV$.

Keeping in mind that different physiological conditions were considered for the unpaced and the paced protocol, and summarized in Table 5.2, we decided to consider two different g_{K1} values for the different pacing conditions. At a starting point we fixed $g_{K1} = 0.06nS/pF$ for unpaced hiPSC-CMs and $g_{K1} = 0.08nS/pF$ for paced CMs, changing at once the external potassium concentration and the maximal potassium conductance.

Resulting APs and currents are described, respectively, in Figure 5.9a and 5.9b.

(a) Unpaced simulation   (b) Paced simulation
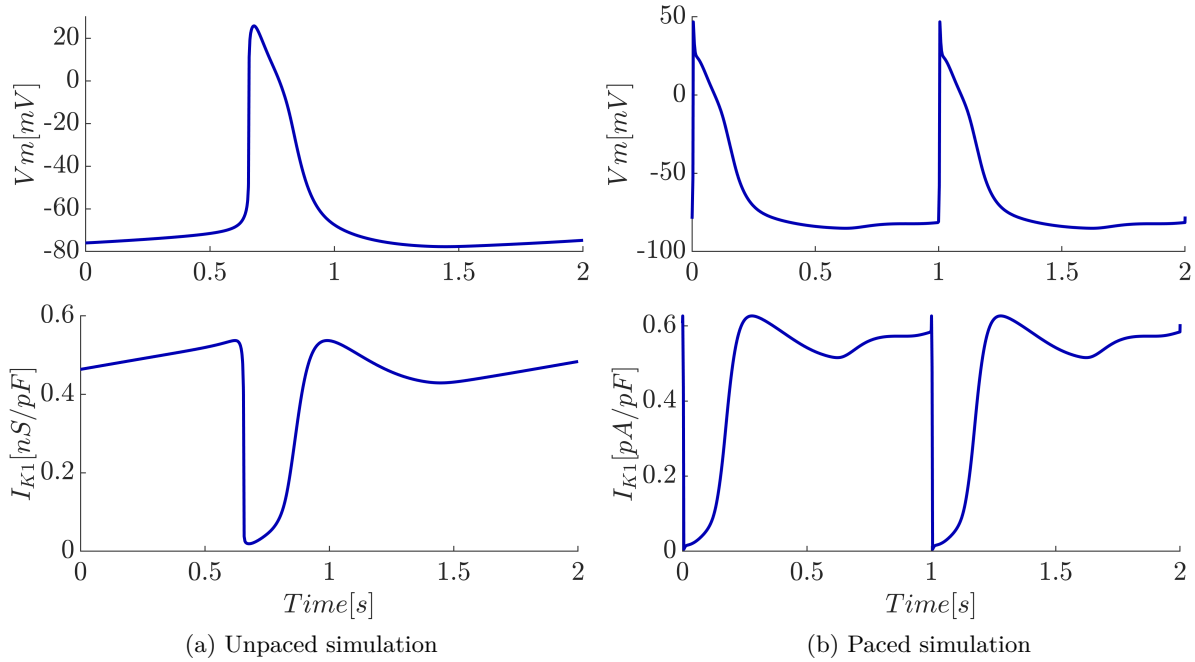
Figure 5.9:   Steady-state simulation of the model with the replaced I_{K1} Koivumäki current, performed in unpaced conditions ($g_{K1} = 0.06nS/pF$) and under a pacing protocol at 1Hz ($g_{K1} = 0.08nS/pF$).

Progress outline

Once every atrial specific current was taken into account, we summarize the major changes affecting the original Paci2020:

1. Parameters switch from VL to AL through given parameters rescaling;

2. Additional I_{Kur} current (Courtemanche formulation);

3. Additional I_{KCa} current (Skibsbye formulation);

4. Update of the I_{K1} current (Koivumäki formulation).

These changes correspond to an additional amount of information concerning the membrane description, leading to a more AL phenotype. As we can see in Figure 5.10, the model presents step by step a more triangular shape, a shorter action potential duration and a more hyperpolarized resting.

To sum up the resulting membrane description, schematically summarized in Figure 5.11, the model consists in a set of 15 currents and 24 variables, differentiated into:

- Action Potential V_m, described by equation the following equation:

$$\frac{dV_m}{dt} = - I_{Na} - I_{NaL} - I_{CaL} - I_f - I_{K1} - I_{Ks} - I_{Kr} - I_{to} - I_{NaCa} - I_{NaK} + \quad (5.12)$$
$$- I_{pCa} - I_{bNa} - I_{bCa} - I_{KCa} - I_{Kur} + I_{stim};$$
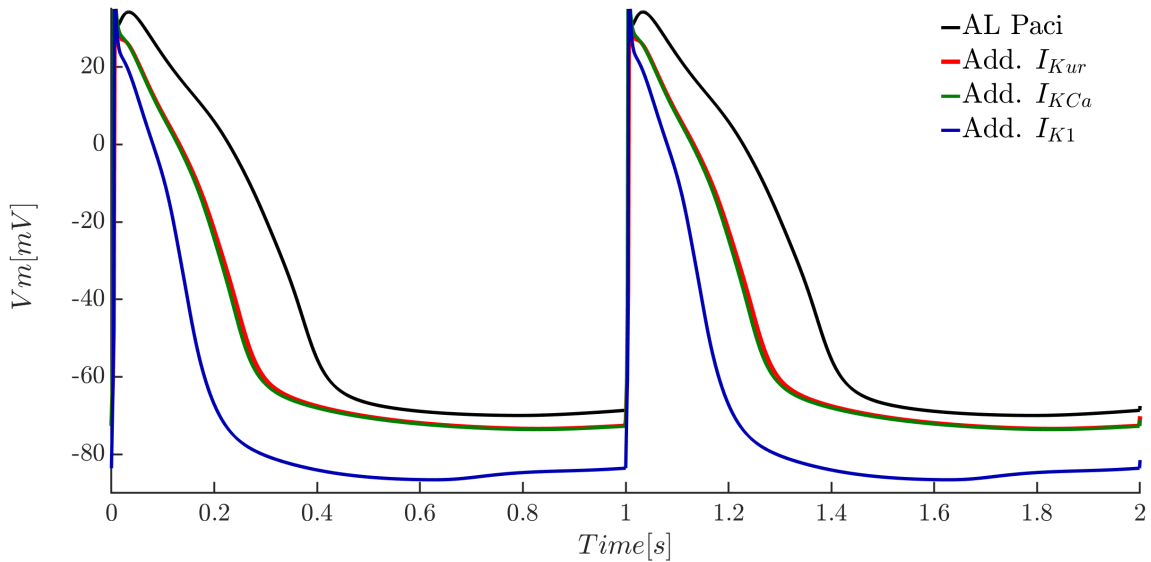
Figure 5.10: Steady-state AP simulation of the model considering four different formulations: the atrial-like version of Paci2020 (black line), the additional I_{Kur} Courtemanche current (red line), the additional I_{KCa} Skibsbye current (green line) and the finally replaced I_{K1} Koivumäki current (blue line).
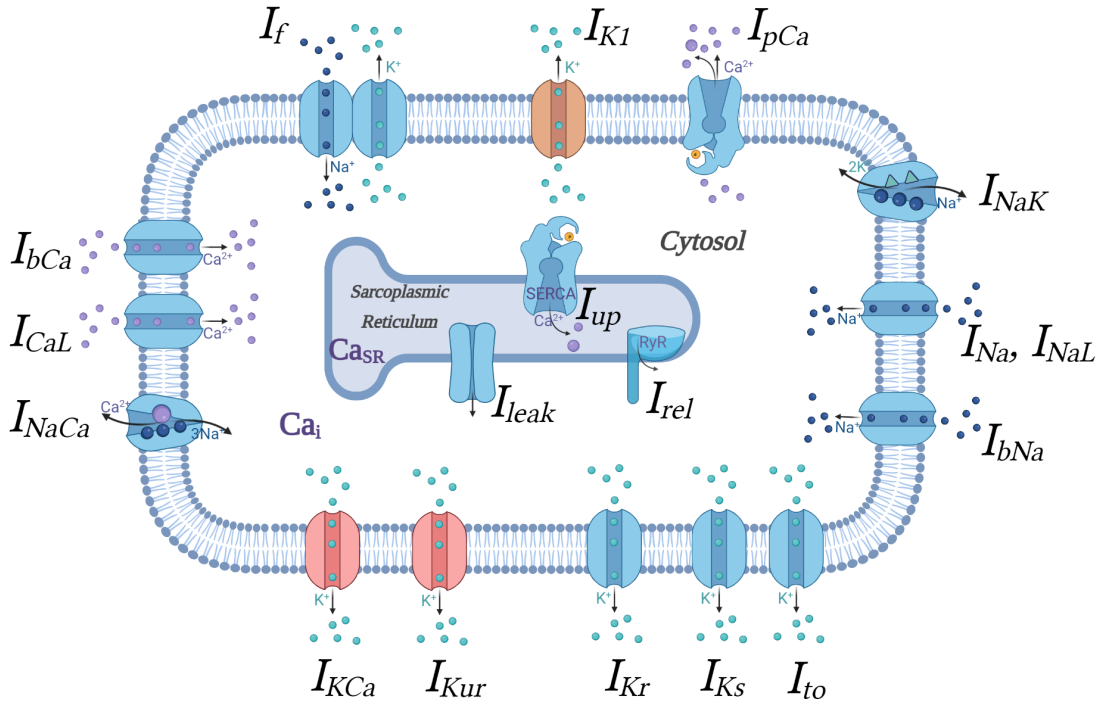
Figure 5.11: Schematic diagram of the model depicting the major functional components and the 13 membrane currents. Ca^{2+}-handling is described by: I_{up} uptaking Ca^{2+} by SR, I_{rel} releasing Ca^{2+} by ryanodine receptors (RyR) and I_{leak}.

- 3 ionic concentrations, described by 3.3, 3.1, 3.2;

- 18 gating variables, involved in 9 different membrane currents

- 3 gating variables RyR_o, RyR_c, RyR_a standing for the Ryanodine Receptors' probabilities of activation, inactivation and adaptation, needed for the novel characterization of calcium dynamic.

The generalized Cauchy (1.17), where $\boldsymbol{c} = (Na_i, Ca_i, Ca_{SR})$ and $\boldsymbol{w} = (w_1, \cdots w_{21})$, can be numerically solved using the ODE solver *ode15s* with a maximum step size of $1ms$.

5.4   Sensitivity analysis

In the previous section we took into account different AL currents, in order to define a novel *in-silico* model able to describe qualitatively an AL hiPSC-CMs. We should now test the model and quantitatively analyze different values, in order to fit the given experimental data.

5.4.1   Ryanodine Receptors

The first test concerns the steady-state condition, that a typical ionic model reaches after 700 second of simulation given generic initial conditions. Even though it is not possible to prove that a limit cycle for the whole system exists, we can check that every transient concentration is

bounded in physiological conditions.

What actually happens is that the Sodium concentration reaches the steady state, but the paced model presents the disappearance of the intracellular calcium ($Ca_i = 0mM$ at steady state) and a first order increase of the Sarcoplasmic Ca^{2+} concentration (see Figure 5.12). The unpaced model prevents this accumulation because of a self regulation of the dynamic. On the other hand the external current applied to the cell leads to an extreme calcium storage inside the Sarcoplasmic Reticulum.

Figure 5.12: $[Ca^{2+}]_{SR}$ dynamic performing both the unpaced and the paced formulations.

The Calcium concentration inside the SR is highly linked to the CICR dynamic, governed by $I_{leak}, I_{up}, I_{rel}$ (equations 3.14-3.16).

Specifically, the release current is directly proportional to the Ca_{SR} concentrations, while the uptake is inversely proportional to the calcium concentration.

Gating variables underlying the whole dynamic are the opening and closing probabilities of the Ryanodine Receptor, RyR_o and RyR_c respectively. In this initial model version the closing probability is bounded and forced to a null steady state. Indeed, the channel is always opened and any of this variable presents a proper dynamic, spanning the whole interval $[0, 1]$ (red lines in Figure 5.13). Changes of the $RyRa1$ parameter improve the gating variables waves and the resulting scaling factor ($RyRa1 \times 2$) leads the Ryanodine Receptor to a physiological dynamic, as described by the green lines (both dash and solid ones) of Figure 5.13.

After a final check on the transient concentrations we can state that, considering the updated parameter, the model reaches the steady state and both intracellular and sarcoplasmic calcium concentrations are bounded in physiological values (see Figure 5.14).

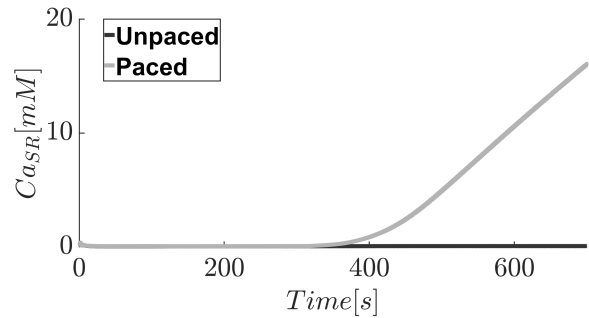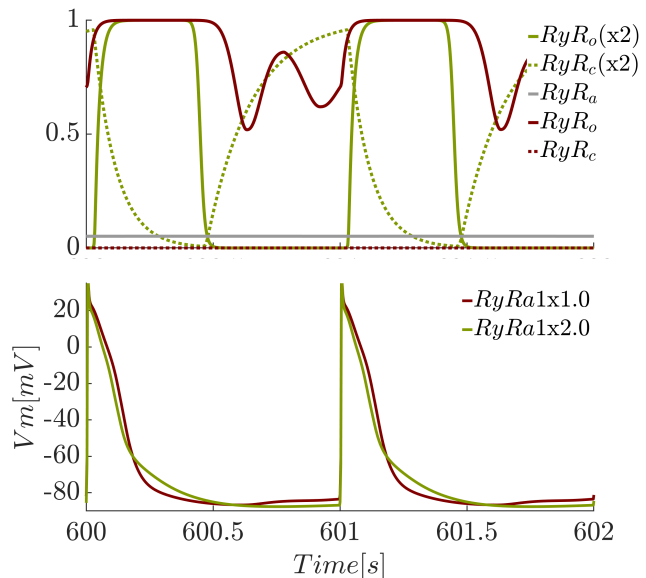Figure 5.13: AP and simultaneous gating variables dynamic considering the original (red line) formulation and the modified (green line) $RyRa1$ parameter.
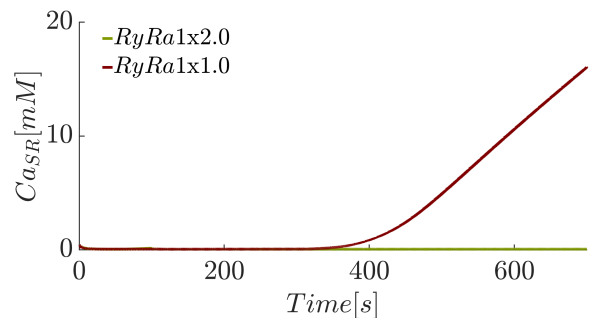

Figure 5.14: $[Ca^{2+}]_{SR}$ dynamic considering the original formulation and the modified $RyRa1$ parameter.

5.4.2   Maximal potassium conductance

A second parameter playing a key role in the resulting AP wave form is the maximal potassium conductance. We have already underlined the discriminating role between the paced and the unpaced formulation, allowing the spontaneous beating for a small range of values (see Figure 5.8). Therefore, the sensitivity analysis will be carried out considering separately the different lines.

Unpaced formulation   Firstly, we will focus on the unpaced model. The spontaneous firing activity is enabled for $g_{K1} \in [0.04, \quad 0.07]$, thus we manually tuned the conductance minimizing the discrepancy between experimental data of Ma et al. [66] and simulated model in terms of biomarkers. We tested three different nominal conductances and results are reported in the following Table 5.6.

The first biomarker to be checked is the $rappAPD$, that we have already described as the discriminant between AL and VL phenotype. According to the literature, this value should be lower than 1.5 for AL hiPSC-CMs and this happens for every tested conductance.
Another relevant parameter is the cicle length, that is the only biomarker characterizing the spontaneous beating. This value increases with the conductance and reveals that the AP frequency decreases until it stops for the threshold conductance.
According to these remarks and observing the bold values in Table 5.6, we can state that the nominal g_{K1} that minimized the error for most of the parameters is $g_{K1} = 0.05 \quad nS/pF$.

| | Unpaced | g_{K1} **nominal values** $[nS/pF]$ | | |
	Exp. data	0.04	0.05	0.06
MDP $[mV]$	-73.5 ± 1.5	-66.59	$\mathbf{-73.504}$	-77.86
APA $[mV]$	100.2 ± 2.1	91.287	$\mathbf{101.160}$	$\mathbf{102.142}$
$Peak$ $[mV]$	26.7 ± 1.4	24.688	$\mathbf{27.652}$	24.236
APD_{10} $[ms]$	60.8 ± 5.5	$\mathbf{58.172}$	66.089	$\mathbf{56.342}$
APD_{30} $[ms]$	123.1 ± 10.3	135.31	149.017	$\mathbf{125.86}$
APD_{90} $[ms]$	286.9 ± 21.2	332.22	367.981	341.17
$rappAPD$	1.1 ± 0.1	0.914	0.805	0.623
CL $[ms]$	1200 ± 200	883.6	$\mathbf{1386.97}$	2388.80

Table 5.6: AP biomarkers comparison considering the unpaced Ma et al. experimental data and different g_{K1} nominal values expressed in nS/pF.

Paced formulation   The second line to be optimized is the paced formulation, that we want to compare with the specific Altomare et al. experimental set of biomarkers. These cells are qualitatively characterized by a triangular shape, corresponding to a short ADP_{90}.

We started analysing different conductances, starting from $0.08 nS/pF$ and we can see in Figure 5.15 that higher I_{K1} current densities correspond to shorter AP.

We performed a quantitative comparison, increasing the g_{K1} parameter up to two times the starting value. For each biomarker the relative error gradually decreased, except for the MDP, that gradually moves toward more negative and non physiological values.

Figure 5.15: AP dynamic considering different g_{K1} values.

For $g_{K1} = 0.15 nS/pF$ and $g_{K1} = 0.16 nS/pF$ three biomarkers concerning the action potential duration reached the experimental bound (Mean $\pm$ Dev. St.) and $g_{K1} = 0.16 nS/pF$ is the eligible value, this one providing smaller errors than the others (see Table 5.7).

	Paced Exp. data	g_{K1} nominal values					
		0.09	**0.11**	**0.13**	**0.14**	**0.15**	**0.16**
MDP $[mV]$	-80.91 ± 3.16	-87.80	-90.17	-91.61	-92.14	-92.58	-92.97
APD_{90} $[mV]$	70.72 ± 33.41	288.22	200.61	140.45	117.21	**99.33**	**86.76**
APD_{20} $[mV]$	12.17 ± 9.04	22.08	**13.13**	**9.25**	**8.50**	7.96	7.88
APD_{50} $[ms]$	39.5 ± 22.7	94.57	63.91	**48.81**	**44.03**	40.05	37.03
$APD_{20/90}$	0.17 ± 0.056	0.08	0.07	0.07	0.07	0.08	0.09
V_{max} $[mV/ms]$	154.96 ± 51.49	247.17	234.12	228.61	**110.85**	71.48	68.38
APA	111.2 ± 12.12	130.02	128.70	127.92	127.16	126.29	125.25

Table 5.7: AP features comparison considering the paced Altomare et al. experimental data and different g_{K1} nominal values expressed in nS/pF.

A final qualitative comparison with the experimental traces is performed using $g_{K1} = 0.09 nS/pF$ (on the left) and $g_{K1} = 0.16 nS/pF$ (on the right). As we can see in Figure 5.16, the suggested value better fits the given data with a most suitable morphology.
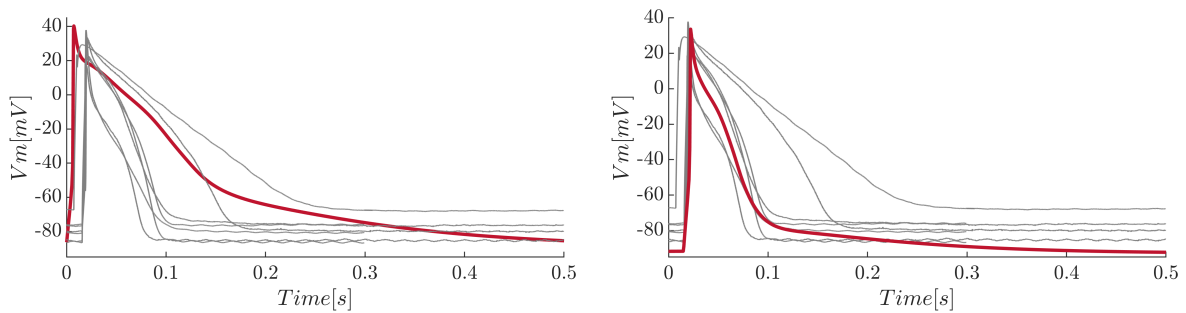
Figure 5.16: Experimental data (grey lines) overlapped with the simulated model (red line), performed with the pacing at 1Hz, considering $g_{K1} = 0.09 nS/pF$ (on the left) and $g_{K1} = 0.16 nS/pF$ (on the right).

5.5   Future advances

We have presented in the previous section the manually tuned baseline model for AL hiPSC-CMs, but still different biomarkers are out of experimental bound.

To reach the expected fitting we are planning to process an automatically parameter optimization. The hybrid optimization approach combines a genetic optimization and a simplex optimization, as described in [11]. The first step is usually done using the Matlab function *ga*, while the second step corresponds to the Matlab implementation of the Nelder-Mead Simplex Method, namely *fminsearchbnd* function. This implemented method minimized the cost function, built on the experimental biomarkers we took into account. Specifically, we manage to minimize the following cost

$$Cost = \sum_{1}^{N} w_i \cdot Cost_i \tag{5.13}$$

$$Cost_i = \frac{(b_{i,exp} < LB_i)(b_{i,exp} - LB_i)^2 + (b_{i,exp} > UB_i)(b_{i,exp} - UB_i)^2}{0.5(LB_i + UB_i)} \tag{5.14}$$

where $b_{i,exp}$ is the ith biomarker, N the number of biomarkers used, w_i the weight for each biomarker's cost and LB_i, UB_i the lower and the upper bound respectively for the considered biomarker i. Each bound depend on the experimental standard deviation of the single biomarker.

The final phase deals with the model validation, we are managing to perform considering (i) the rate dependence on the applied pacing rate (testing 1, 2, and 5 Hz); (ii) the effect of the I_{Kur} block, then compared with the experimental effect of the non-selective blocker 4-Aminopyridine.

Chapter 6

Isogeometric modeling of an engineered ventricle

In the previous chapters, we have widely approached the electrophysiological modeling of a single hiPSC-CM, that is the first step to deal with preclinical drugs tests and disease modeling. On the other hand, as we presented in Chapter 2, hiPSC-CMs technology evolves in the promising field of regenerative medicine in terms of tissue transplants and organoids building. The final aim is to use stem cells derived from patients with heart disease to create *in-vitro* ventricles, so that the models capture the exact genetic background and mutations of the patients.

Many of the heart disease models that researchers actually use are cells that are grown in flat layers. But the contractions and electrical signals in these cell layers are far removed from three-dimensional heart chambers, which pump blood with different volumes and pressures. Furthermore, it has been proved that culturing hiPSC-CM as 3-dimensional engineered heart tissue improves cardiomyocytes maturity and anisotropy. By *Engineered heart tissues* we mean three-dimensional, muscle strips, or muscular thin films, that can be generated from isolated heart cells or hiPSC-CMs, through a method introduced in 1997. Such technique requires (i) heart cells, (ii) a liquid hydrogel that solidifies and promotes tissue formation, (iii) a support structure, or a scaffold, to which the cell-containing hydrogel attaches [26, 32, 132].

Using these insights Kevin Kit Parker and William Pu (Harvard Stem Cell Institute) created an improved tissue-engineered scale model of the human heart. In their latest study, published in Nature Biomedical Engineering, they built a three-dimensional model of a heart ventricle, combining engineered nanofibers with stem cell technology, [67, 68].

First,the scaffold was designed taking inspiration from the human myocardial tissue architecture and recreated using a nanofiber production system. The strategy developed for the production of a nanofiber ventricle based on pull-spinning fibers on a rotating ellipsoidal collector. Pull spinning uses a high-speed rotating bristle that dips into a polymer reservoir and pulls a droplet from the solution into a jet. The fiber travels in a spiral trajectory and solidifies before detaching from the bristle and moving toward a collector. Because the collector is spinning, all of the fibers align in the same direction.

Next, they added heart muscle cells obtained from rats or differentiated from human induced

pluripotent stem cells. The resulted fabricated thin-wall chambers were then sutured to tubing or bioreactor components, and it contracted to move fluid in and out of the chamber successfully. Catheter sensors were then introduced and stable contraction of hiPSC-CM ventricles permitted time-dependent pressure and volume measurements.

To create a proof-of-concept disease model, the researchers injured the engineered ventricle to mimic structural arrhythmia (a disease where abnormalities in heart structure result in irregular heartbeats). For example, they poked holes in the ventricle to mimic a myocardial infarction, and studied the effect of the heart attack.

Starting from a mathematical point of view, we purposed to create a virtual framework of the experiment, in order to reproduce the same results. Thus, we started a new project, joint with Professor Alessandro Reali, the PhD student Michele Torre, [127] and Professor Francesco Pasqualini,head of the Synthetic Physiology Lab. The idea was to merge respectively knowledge and scientific interest creating an electrophysiological model approximated using Isogeometric Analysis.

Figure 6.1: CAD drawings of the left ventricle collector, presented in [68], supplementary material, Figure 1
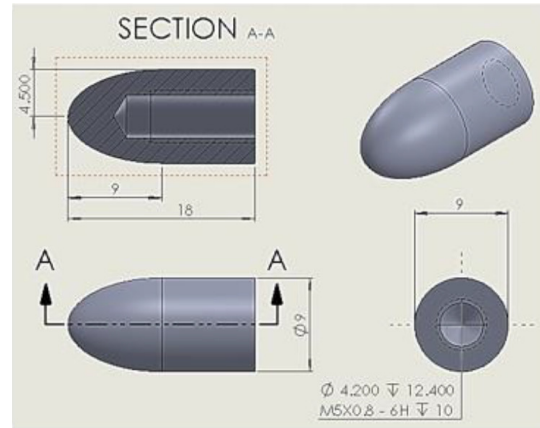
In order to model this engineered ventricular chamber, we stared from the scaffold geometry depicted in Figure 6.1, described as a half ellipsoid with radii $a = b = 4.5$ and $c = 9$ mm [68]. From literature, we know the diameter of a hiPSC-CM fiber is roughly $1 \mu m$, thus, considering the overlap between fibers, the chamber diameter is supposed to be almost equal to $2 \mu m$.

6.1   Mathematical formulation of the problem

In order to create a mathematical description of the problem, we need to derive the canonical set of equations for the propagation of the electrical stimulus in the cardiac tissue, schematized through a reaction-diffusion system. This macroscopic representation corresponds to the Bidomain model.

The canonical description of the cardiac electrophysiology models the behaviour of the tissue in space $\boldsymbol{x} \in \Omega$ and time $t \in (0, T)$ by means of two superimposed continua, that represent the intra-cellular and the extra-cellular spaces. These compartments exchange the charge via the ionic current per unit area of the membrane surface, I^{ion}, that is carried by the flow of ions across the membrane, described for this specific problem by the Paci2018 ventricular-like ionic model, [83]. The intensity of this current across the cellular membrane depends in a point-wise manner on:

- the difference between the intra-cellular potential u_i and the extra-cellular potential u_e

$$v\left(\boldsymbol{x}, t\right) = u_i\left(\boldsymbol{x}, t\right) - u_e\left(\boldsymbol{x}, t\right), \tag{6.1}$$

- the cellular state via the ion concentrations c^s and gate variables w^r, in the number of $s = 1, \ldots, 3$ and $r = 1, \ldots, 18$ respectively, according to Paci2018 model.

Moreover, inside a single compartment, the charge moves accordingly to the linear diffusion law governed by the conductivity tensor $\mathbf{D}$ or $\mathbf{D}_e$, for the intra-cellular and extra-cellular spaces respectively, linking the local cellular state to the one of the neighbouring cells.

These phenomena, jointly to the ability of the cellular membrane in separating the charge and the charge conservation law (taking into account both the intra-cellular and extra-cellular applied currents I_i^{app} and I_e^{app}), lead to the Bidomain formulation [19, 43, 121]. It embed the single cell model, described by a system of ordinary differential equations (ODEs) (eq. (6.2c), (6.2d), and (6.2e)), into a system of partial differential equations (PDEs) (eq. (6.2a) and (6.2b)):

$$
\begin{cases}
\chi C_m \dfrac{\partial v}{\partial t} - \nabla \cdot (\mathbf{D}\nabla v) - \nabla \cdot (\mathbf{D}\nabla u_e) + \chi I^{ion} = I_i^{app} & \text{in } \Omega - \partial\Omega \times (0,T) & (6.2a) \\[2mm]
-\nabla \cdot (\mathbf{D}\nabla v) - \nabla \cdot ((\mathbf{D} + \mathbf{D}_e)\nabla u_e) = I_e^{app} + I_i^{app} & \text{in } \Omega - \partial\Omega \times (0,T) & (6.2b) \\[2mm]
I^{ion} = I^{ion}\left(v, w^1, \ldots, w^k, c^1, \ldots, c^q\right) & \text{in } \Omega \times (0,T) & (6.2c) \\[2mm]
\dfrac{\partial w^r(\boldsymbol{x},t)}{\partial t} = m_w^r\left(v, w^1, \ldots, w^k\right) \ \forall r = 1, \ldots, 18 & \text{in } \Omega \times (0,T) & (6.2d) \\[2mm]
\dfrac{\partial c^s(\boldsymbol{x},t)}{\partial t} = m_c^s\left(v, w^1, \ldots, w^k, c^1, \ldots, c^q\right) \ \forall s = 1, \ldots, 3 & \text{in } \Omega \times (0,T), & (6.2e)
\end{cases}
$$

where C_m is the membrane capacitance per unit area of the membrane surface and χ is the membrane surface area per unit volume of the tissue. The two PDEs describe the potential field evolution, considering the reaction and the diffusion phenomena. The system of equations is then supplied with the no-flux conditions through the external surface $\partial\Omega$, characterized by the outward pointing normal $\mathbf{n}$,

$$
\begin{cases}
\mathbf{n} \cdot \mathbf{D}\nabla(v + u_e) = 0 & \text{on } \partial\Omega \times (0,T) & (6.3a) \\[2mm]
\mathbf{n} \cdot (\mathbf{D} + \mathbf{D}_e)\nabla u_e + \mathbf{n} \cdot \mathbf{D}\nabla v = 0 & \text{on } \partial\Omega \times (0,T) & (6.3b)
\end{cases}
$$

and completed by appropriate initial conditions

$$
\begin{cases}
v(\boldsymbol{x}, 0) = v_0 & (6.4a) \\[2mm]
w^r(\boldsymbol{x}, 0) = w_0^s & \forall r = 1, \ldots, 18 & (6.4b) \\[2mm]
c^s(\boldsymbol{x}, 0) = c_0^s & \forall s = 1, \ldots, 3. & (6.4c)
\end{cases}
$$

Moreover, as the charge has to be conserved, the applied currents have to obey to the compatibility condition

$$
\int_\Omega I_i^{app} + I_e^{app} \, d\boldsymbol{x} = 0. \tag{6.5}
$$

6.1.1 Monodomain approximation

The conductivity of an engineered tissue built on a scaffold depends on (i) the spatial organization and geometrical orientation of the cells [58], and (ii) on the gap junctions expression and other biological factors related to the cell maturation [67, 68].

The engineered ventricle manufacturing process guarantees an high cell alignment, quantified by the Oriental Order Parameter, in the circumferential direction. Coherently, we assume an anisotropic, transversally isotropic, intercellular conductivity tensor with a greater eigenvalue in the fiber direction. The cell maturation affects the conductivity in an involved fashion leading to complex parameter quantifications. To tackle this issue, we simplify the mathematical formulation by assuming that the extracellular conductivity is proportional to the intercellular one

$$\mathbf{D}_e = \lambda \mathbf{D}, \tag{6.6}$$

as already done in various studies regarding the human heart [60, 91]. With these assumptions, we reduce the number of unknown parameters to two. In comprehensive studies [7–9, 139], the authors compute the conductivity by means of the solution of an inverse problem. However, this technique requires complete informations in space and time of the electrical signal propagation. We believe that such a refined procedure is out of the scope the present work and a simplified procedure, adopted in [60], for approximatively constant conductivity is sufficient. In [58], an experimental investigation of the electrical-signal propagation velocity in *in-vitro* assay was conducted. The researchers determinate the ratio between the velocity in the fiber and in the orthogonal direction as a function of the cell alignment. In our simulations, we set the velocity in the transversal direction equal to the value reported in [68], while for the value in the fiber direction we enforce the ratio [58] that most closely represents the fiber organization of the ventricle. Consequently, we perform *ad hoc* simulations, described in sec. 6.3.2, to calibrate the conductivity parameters. In our opinion, this approximation is a good compromise between a meaningful modelling and the effort needed to obtain additional experimental data for a comparison between numerical approaches.

The equal anisotropy hypothesis (6.6) greatly simplifies the Bidomain formulation (equations (6.2a), (6.2b), and (6.3)). Indeed, after some algebraic manipulations, presented in [121], we recover the Monodomain formulation

$$\begin{cases} \chi C_m \dfrac{\partial v}{\partial t} - \dfrac{1}{\lambda + 1} \nabla \cdot (\mathbf{D}\nabla v) + \chi I^{ion} = I^{app} & \text{in } \Omega - \partial\Omega \times (0, T) \tag{6.7a} \\ \mathbf{n} \cdot \mathbf{D}\nabla v = 0 & \text{on } \partial\Omega \times (0, T), \tag{6.7b} \end{cases}$$

that describes the electrophysiology of the tissue with a single PDE, instead of two, in terms of the unknown transmembrane potential v, where the applied current I^{app} is given by the difference between the internally and externally applied currents:

$$I^{app} = \frac{1}{1 + \lambda} \left(\lambda I_i^{app} - I_e^{app} \right) \tag{6.8}$$

6.1.2 Splitting operator applied to the Monodomain formulation

To solve the Monodomain equation we employ a splitting operator to separate the reactive and diffusive terms [91, 108]. More precisely, we adopt the symmetric, second order accurate, Strang splitting operator, as successfully done in [121].

As we schematically summarized in Figure 6.2, the splitting operator subdivides the time in intervals, whose size is Δt, and employs three different solution steps, schematically represented in figure 6.2, for the analysis of each time interval:

- given the variables v, w^r, and c^s at time $t = t_n$, in the first step we integrate the reactive term

$$
\begin{cases}
\dfrac{\partial v}{\partial t} = -\dfrac{1}{C_m} I^{ion} & \text{(6.9a)} \\[2mm]
\dfrac{\partial w^r}{\partial t} = m_w^r \left(v, w^1, \ldots, w^k \right) & \forall r = 1, \ldots, 18 & \text{(6.9b)} \\[2mm]
\dfrac{\partial c^s}{\partial t} = m_c^s \left(v, w^1, \ldots, w^k, c^1, \ldots, c^q \right) & \forall s = 1, \ldots, 3 & \text{(6.9c)}
\end{cases}
$$

  for $t \in (t_n, t_n + \Delta t/2 = \theta/2)$ to compute $v_{\theta/2} = v\left(\boldsymbol{x}, \theta/2\right)$, $w_{\theta/2}^r = w^r\left(\boldsymbol{x}, \theta/2\right)$, and $c_{\theta/2}^s = c^s\left(\boldsymbol{x}, \theta/2\right)$.

- Given $v_{\theta/2}$ as initial condition for v, in the second step we integrate the diffusive term

$$
\begin{cases}
\dfrac{\partial v}{\partial t} = \dfrac{1}{\chi C_m \left(\lambda + 1 \right)} \left[\lambda \nabla \cdot \left(\mathbf{D} \nabla v \right) + \left(\lambda I_i^{app} - I_e^{app} \right) \right] & \text{(6.10a)} \\[2mm]
\mathbf{n} \cdot \mathbf{D} \nabla v = 0 & \text{(6.10b)}
\end{cases}
$$

  for $t \in (t_n, t_n + \Delta t = \theta)$ to compute $v_\theta = v\left(\boldsymbol{x}, \theta\right)$.

- In the third step, we integrate the reactive term using v_θ, $w_{\theta/2}^r$, and $c_{\theta/2}^s$ as initial conditions, for $t \in (t_n + \Delta t/2, t_n + \Delta t)$ to obtain the variables $v_{n+1} = v\left(\boldsymbol{x}, t_{n+1}\right)$, $w_{n+1}^r = w^r\left(\boldsymbol{x}, t_{n+1}\right)$, and $c_{n+1}^s = c^s\left(\boldsymbol{x}, t_{n+1}\right)$ at the beginning of the next time interval.

We note that, the solution scheme does not discretize in time the equations, as highlighted in [121]. Indeed, the time integration schemes will be introduced in section 6.2.2.
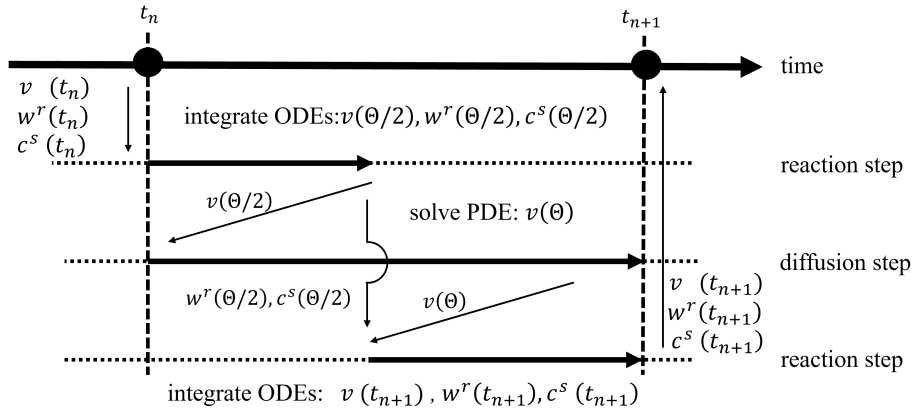

Figure 6.2: Schematic representation of the Strang splitting operator.

6.2   Isogeometric numerical schemes for simulations

Finite Element Method is nowadays a well-established numerical technique for the space discretization of the mathematical formulation of the cardiac electrophysiology. Indeed, various software, notably [95] and [6], employ this Galerkin approach.

In the last two decades, the Isogeometric Analysis turns out to be an effective alternative to the Finite Element Method thanks to its higher accuracy per degree of freedom [21, 38]: its effectiveness was demonstrated in a number of fields, ranging from simulations of cardiovascular stents [5] and studies of the aortic valve dynamics [74] to investigations on the cancer growth [61]. Recently, isogeometric analysis has became a promising technique for electro-mechanical simulations because a novel formulation [75] for thin shell structures activated by the propagating action potential has been proposed, [18].

In linking the electrophysiology and the mechanics of the cardiac tissue, the ion concentrations play a central role in biologically detailed models, because they take part in the tissue activation [41].
Consequently, we compare the ability of isogeometric analysis, with respect to finite element method, in approximating the ion concentrations, because these information are instructive for future electro-mechanical simulations that involves biologically detailed activation models.

6.2.1   Bubnov-Galerkin approach for space discretization

In the spirit of a standard Bubnov-Galerkin method, the weak form of the split Monodomain formulation reads as follows [19]: find $v \in \mathcal{V}$, $w^r \in \mathcal{WC} \ \forall r = 1, \dots, 18$, and $c^s \in \mathcal{WC} \ \forall s = 1, \dots, 3$ such as $\forall \delta v \in \delta \mathcal{V}$, $\forall \delta w \in \mathcal{WC}$, and $\forall \delta c \in \mathcal{WC}$ the following relations hold for the first and the third steps of the Strang operator

$$
\begin{cases}
\int_{\Omega} \delta v \frac{\partial v}{\partial t}\, d\boldsymbol{x} = -\frac{1}{C_m} \int_{\Omega} \delta v\, I^{ion}\, d\boldsymbol{x} & \text{(6.11a)} \\[2ex]
\int_{\Omega} \delta w \frac{\partial w^r}{\partial t}\, d\boldsymbol{x} = \int_{\Omega} \delta w\, m_w^r\, d\boldsymbol{x} & \forall r = 1, \dots, 18 \quad \text{(6.11b)} \\[2ex]
\int_{\Omega} \delta c \frac{\partial c^s}{\partial t}\, d\boldsymbol{x} = \int_{\Omega} \delta c\, m_c^s\, d\boldsymbol{x} & \forall s = 1, \dots, 3 \quad \text{(6.11c)}
\end{cases}
$$

and

$$
\int_{\Omega} \delta v \frac{\partial v}{\partial t}\, d\boldsymbol{x} = -\frac{1}{\chi C_m\,(\lambda + 1)} \left(\int_{\Omega} \lambda \nabla \delta v \cdot \mathbf{D} \nabla v\, d\boldsymbol{x} + \int_{\Omega} \delta v\, (\lambda I_i^{app} - I_e^{app})\, d\boldsymbol{x} \right) \tag{6.12}
$$

for the second one, where:

$$
\mathcal{V} = \left\{ v | v \in H^1\,(\Omega; t)\, \forall t \in (0, T)\ \wedge\ v = v_D\, on\, \partial\Omega_D \right\}, \tag{6.13}
$$

$$
\delta\mathcal{V} = \left\{ \delta v | \delta v \in H^1\,(\Omega; t)\, \forall t \in (0, T)\ \wedge\ v = 0\, on\, \partial\Omega_D \right\}, \tag{6.14}
$$

$$
\mathcal{WC} = \left\{ f | f \in L^2\,(\Omega; t)\, \forall t \in (0, T) \right\}, \tag{6.15}
$$

$H^1\left(\Omega;t\right)$ is the Sobolev space of functions with square integrable first derivatives in Ω at time t and $L^2\left(\Omega;t\right)$ is the space of square integrable functions in Ω at time t.

If we replace the functional spaces with finite dimensional approximations, the transmembrane potential v and the test function δv can be written as linear combination of shape functions $\mathbf{N}$ and nodal variables $\hat{\mathbf{v}}$ and $\boldsymbol{\delta}\hat{\mathbf{v}}$ as

$$v\left(\boldsymbol{x},t\right) = \mathbf{N}\left(\boldsymbol{x}\right)\hat{\mathbf{v}}\left(t\right) \tag{6.16}$$

and

$$\delta v\left(\boldsymbol{x},t\right) = \mathbf{N}\left(\boldsymbol{x}\right)\boldsymbol{\delta}\hat{\mathbf{v}}\left(t\right). \tag{6.17}$$

In the present work, as in [128], we employ two different kind of shape functions that depend on the adopted discretization approach, as explained in the following.

By replacing (6.16) and (6.17) in (6.12) we obtain the following semi-discrete formulation

$$\mathbf{M}\dot{\hat{\mathbf{v}}} = -\mathbf{K}\hat{\mathbf{v}} + \hat{\mathbf{I}}^{app}, \tag{6.18}$$

where the components of the mass matrix $\mathbf{M}$ are given by

$$\mathrm{M}_{ab} = \int_{\Omega}\mathrm{N}_a\mathrm{N}_b\,d\boldsymbol{x}, \tag{6.19}$$

the stiffness matrix $\mathbf{K}$ – introducing the notation for derivatives $\dfrac{\partial}{\partial x_i}\left(\bullet\right) = \bullet_{,i}$ – is given by

$$\mathrm{K}_{ab} = \frac{\lambda}{\chi C_m\left(\lambda+1\right)}\int_{\Omega}\mathrm{N}_{a,i}\mathrm{D}_{ij}\mathrm{N}_{b,j}\,d\boldsymbol{x}, \tag{6.20}$$

and the entries of the vector $\hat{\mathbf{I}}^{app}$ are

$$\hat{\mathrm{I}}_a^{app} = \frac{1}{\chi C_m\left(\lambda+1\right)}\int_{\Omega}\mathrm{N}_a\left(\lambda I_i^{app} - I_e^{app}\right)\,d\boldsymbol{x}. \tag{6.21}$$

In the numerical computation of these integrals, we employ the standard Gauss quadrature rule with $p+1$ Gauss points in each direction, where p is the basis functions degree, although it is not the optimal choice for Isogeometric Analysis [39].

Electrophysiological simulations with detailed cellular models may be computationally demanding [121]. To reduce this effort, we adopt the so called Ionic Current Interpolation (ICI) approach, as in [91], because it is more computationally efficient than the State Variable Interpolation and the Gauss Integration approaches, although it has a reduced accuracy, especially near to the wave front [53, 92].

The ICI approach interpolates the ionic current using the basis functions

$$I^{ion} = \mathbf{N}\left(\boldsymbol{x}\right)\hat{\mathbf{I}}^{ion}\left(t\right). \tag{6.22}$$

Substituting (6.22) in (6.11) and adopting the already presented discretization method for

the cellular state variables

$$
\begin{cases}
w^r\left(\boldsymbol{x},t\right) = \mathbf{N}\left(\boldsymbol{x}\right)\hat{\mathbf{w}}\left(t\right)^r & \forall r = 1,\dots,18 \\[6pt]
c^s\left(\boldsymbol{x},t\right) = \mathbf{N}\left(\boldsymbol{x}\right)\hat{\mathbf{c}}\left(t\right)^s & \forall s = 1,\dots,3
\end{cases}
$$

$$(6.23a)$$
$$(6.23b)$$

and their test functions

$$
\begin{cases}
\delta w\left(\boldsymbol{x},t\right) = \mathbf{N}\left(\boldsymbol{x}\right)\boldsymbol{\delta}\hat{\mathbf{w}}\left(t\right) \\[6pt]
\delta c\left(\boldsymbol{x},t\right) = \mathbf{N}\left(\boldsymbol{x}\right)\boldsymbol{\delta}\hat{\mathbf{c}}\left(t\right),
\end{cases}
$$

$$(6.24a)$$
$$(6.24b)$$

we end up with nodal variable relations

$$
\begin{cases}
\dot{\hat{\mathbf{v}}} = -\dfrac{1}{C_m}\hat{\mathbf{I}}^{ion} \\[10pt]
\dot{\hat{\mathbf{w}}}^r = \hat{\mathbf{m}}_w^r & \forall r = 1,\dots,18 \\[10pt]
\dot{\hat{\mathbf{c}}}^s = \hat{\mathbf{m}}_c^s & \forall s = 1,\dots,3,
\end{cases}
$$

$$(6.25a)$$
$$(6.25b)$$
$$(6.25c)$$

where each entry in the vectors at the right hand side correspond to the functions evaluated at a given node.

Shape functions for finite element and isogeometric approaches

The basis functions have to fulfil the requirements presented in (6.13), (6.14), and (6.15). Therefore, in the finite element framework, we employ isoparametric, trilinear, lagrangian shape functions defined on hexahedral elements [37].

On the other hand, we use trivariate B-spline as basis functions in the isogeometric framework. Univariate B-spline of order p, defined on a mono-dimensional parametric space subdivided in $n\xi$ spans, are fully described by the knot vector $\Xi = \{\xi_1,\xi_2,\dots,\xi_{n\xi+p+1}\}$ and the Cox-de Boor recursive formula

$$
\begin{aligned}
&\text{for p} = 0 \quad \mathrm{H}_{a;0}\left(\xi\right) =
\begin{cases}
1 & \text{if } \xi_a \le \xi < \xi_{a+1} \\
0 & \text{otherwise}
\end{cases} \\[10pt]
&\text{for p} = 1,2,3,\dots \quad \mathrm{H}_{a;p}\left(\xi\right) = \frac{\xi - \xi_a}{\xi_{a+p} - \xi_a}\mathrm{H}_{a;p-1}\left(\xi\right) + \frac{\xi_{a+p+1} - \xi}{\xi_{a+p+1} - \xi_{a+1}}\mathrm{H}_{a+1;p-1}\left(\xi\right),
\end{aligned}
$$

$$(6.26)$$

presented in [21]. Moreover, in the following we assume open knot vectors, i.e. the first and the last knots have multiplicity equal to p.

A trivariate B-spline N_a is given by the tensor product of three monovariate B-splines H, L, and K, that we suppose of the same degree p. Assuming a bijective relation between the index a and the ordered list of index $\{b,c,d\}$, we identify the shape function defined on a cubic parametric space (given by the tensor product of the mono-dimensional parametric spaces) as

$$
\mathrm{N}_a = \mathrm{H}_b\left(\xi\right)\mathrm{L}_c\left(\eta\right)\mathrm{K}_d\left(\zeta\right).
$$

$$(6.27)$$

The Isogeometric analysis employs the same shape functions for the analysis and for the geo-

metrical description. Coherently, the parametric space defines a patch of the geometry in the physical space via control points coordinates. In the present work, we employ a single patch, thus a single parametric space, to describe the geometry in our numerical experiments. Consequently, the control point coordinates are computed as shown in [21, 94] for simple geometry, while a mapping procedure, presented in sec. 6.3.1, is employed for the engineered ventricle.

6.2.2 Time discretization

For the discretization in time of equations (6.18) and (6.25) we employ two different schemes. The non-linear system of ODE of the first and third Strang steps is integrated using the Explicit Euler method, with a reduced step size in order to guarantee a sufficient accuracy.

Therefore, the adopted time step size for the m sub-steps is $\Delta\tilde{t} = \Delta t/(2m)$ and the discrete expression for $\hat{\mathbf{v}}_{m+1} = \hat{\mathbf{v}}(t_m + \Delta\tilde{t})$, $\hat{\mathbf{w}}^r_{m+1} = \hat{\mathbf{w}}^r(t_m + \Delta\tilde{t})$ and $\hat{\mathbf{c}}^s_{m+1} = \hat{\mathbf{c}}^s(t_m + \Delta\tilde{t})$, used to compute $\hat{\mathbf{v}}_{\theta/2}$, $\hat{\mathbf{w}}^r_{\theta/2}$, and $\hat{\mathbf{c}}^s_{\theta/2}$ or $\hat{\mathbf{v}}_{n+1}$, $\hat{\mathbf{w}}^r_{n+1}$, and $\hat{\mathbf{c}}^s_{n+1}$, is

$$
\begin{cases}
\hat{\mathbf{v}}_{m+1} = \hat{\mathbf{v}}_m - \dfrac{\Delta\tilde{t}}{C_m}\hat{\mathbf{I}}^{ion}(t_m) & \text{(6.28a)} \\[2mm]
\hat{\mathbf{w}}^r_{m+1} = \hat{\mathbf{w}}^r_m + \Delta\tilde{t}\,\hat{\mathbf{m}}^r_w(t_m) & \forall r = 1,\dots,18 \quad \text{(6.28b)} \\[2mm]
\hat{\mathbf{c}}^s_{m+1} = \hat{\mathbf{c}}^s_m + \Delta\tilde{t}\,\hat{\mathbf{m}}^s_c(t_m) & \forall s = 1,\dots,3. \quad \text{(6.28c)}
\end{cases}
$$

In the diffusion step, we employ the implicit, second order accurate, Crank-Nicolson method, with time step size equal to Δt, to increase the overall scheme stability. The resulting discrete formulation is

$$
\left(\mathbf{M} + \frac{\Delta t}{2}\mathbf{K}\right)\hat{\mathbf{v}}_\theta = \mathbf{M}\hat{\mathbf{v}}_{\theta/2} + \frac{\Delta t}{2}\left(-\mathbf{K}\,\hat{\mathbf{v}}_{\theta/2} + \hat{\mathbf{I}}^{app}_n + \hat{\mathbf{I}}^{app}_{n+1}\right). \tag{6.29}
$$

6.3 *In-silico* model of the engineered ventricle

6.3.1 Geometrical modelling

The engineered ventricle manufacturing process consists on seeding and growing hiPSC-CMs on a scaffold previously formed on a collector. In the present work, we simplify the actual irregular shape of the ventricle assuming that it is a constant-thickness extrusion of the scaffold moulding surface. Coherently, we model the ventricle as the space between the idealized internal surface of the scaffold and the idealized external one.

The mesh generation is nowadays a standard procedure for hexahedral linear finite elements and is implemented in many open-source software, such as Gmsh, [31]. Moreover, we refer the reader to [143] for a review on meshing techniques. On the other hand, isogeometric analysis requires a different procedure.

The geometrical mapping of the isogeometric parametric space into the physical geometry, i.e. the computation of the control point coordinates, involves three steps: (i) the mapping of a parametric plane surface into the internal 3D manifold, (ii) the mapping of a parametric surface into the external manifold adopting a the same discretization of the previous surface, and (iii)
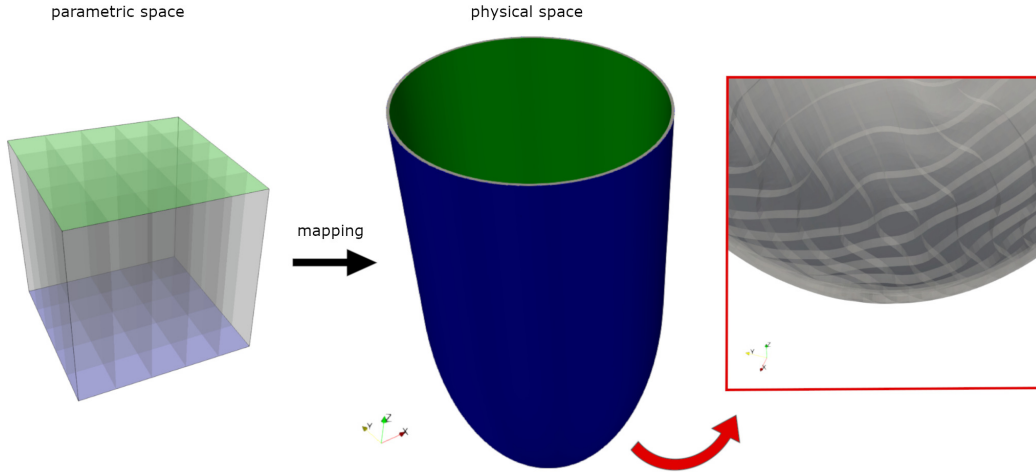
Figure 6.3: Schematic representation of the geometrical mapping procedure from the isogeometric parametric space to the physical geometry. Zoom in the red frame: the Bézier mesh at the apex does not present any singularity. For better visualization, not all the elements are depicted.

the interpolation of the corresponding couples of control point coordinates of the two manifolds to create the volume. After that, the ventricle geometry $\boldsymbol{x}$ is reconstructed by means of of a linear combination of control point coordinate and shape functions

$$\boldsymbol{x}\left(\xi,\eta,\zeta\right) = \sum_{a=1}^{ncp} \mathrm{N}_a\left(\xi,\eta,\zeta\right)\mathbf{B}_a, \tag{6.30}$$

where *ncp* is the number of control points.

As described in [68], half ellipsoid, linked to a cylinder, constitutes the idealized internal surface of the ventricle. In order to reproduce it using a B-spline surface, we compute the control point coordinates by means of minimization of a functional, because we employ a single patch to construct the geometry and therefore we can not describe it exactly. Indeed, the shape obtained linking two conic sections is no more a conic section.

As we are mostly interested in the simulation results at the region near to the ventricle apex, we employ the procedure, presented in [46], with the aim of move the geometrical singularities inherited by the construction of the circle near to the ventricle base. From a geometrical point of view, we construct the surface by stretching the square parametric surface, in green in Figure 6.3, in a circle and pushing down the center to create the apex.

From a mathematical point of view, we compute the vector $\mathbf{B}^{\mathrm{CP}}$, that collects all the control point coordinates, minimizing the square of the L^2 norm of distance between the idealized surface $\boldsymbol{x}^{ide}$ and the mapped one $\boldsymbol{x}\left(\mathbf{B}^{\mathrm{CP}}\right)$ as

$$\mathbf{B}^{\mathrm{CP}} = \arg\min_{\mathbf{B}^{\mathrm{CP}}}\left\{\left\|\boldsymbol{x}^{ide}-\boldsymbol{x}\left(\mathbf{B}^{\mathrm{CP}}\right)\right\|_{\mathrm{L}^2}^2\right\} \tag{6.31}$$

by means of least square method.

The external surface is treated in a similar way. Indeed, it is obtained from the internal

one increasing the dimensions of the conic sections. As the parametric space is given by a tensor product, we must employ the same discretization for both the surfaces because the external surface, in blue in Figure 6.3, correspond to parametric face opposite to internal surface. Coherently, for each control point of the internal surface, we have a corresponding point for the external surface.

Once the two surfaces are mapped, we define a single linear knot span in the third parametric direction that links the surfaces originating a volume. Having done so, the geometrical mapping procedure is complete but for accuracy purposes a basis function refinement may be needed. As explained in [21], isogeometric analysis enables three different types of refinements, namely $h-$, $p-$, and $k-$refinement. In particular, we always apply a degree elevation in the third parametric direction to obtain the same basis function degree in all the parametric directions.

As described in [68] and as previously discussed, the engineered tissue is organized in fibers. In the *in-silico* model of the engineered ventricle, we assume that the fibers are oriented in the circumferential direction and slightly inclined toward the apex, with an angle equal to 5^{deg}.

An interesting source for future developments is the extension of the presented mapping procedure to the reconstruction of the actual ventricle geometry. In particular, a direct computation of the B-spline volume from a set of diagnostic images would be useful, as already presented in [102, 119] for finite element discretization.

6.3.2   Framework for cardiac tissue properties assessment

In many practical applications the tissue conductivity is unknown [58, 68] but the speed of propagation of the electrical stimulus can be measured. We develop a computational framework to reconstruct the conductivity of the tissue using the information on the conduction velocity, as delineated in [60].

The authors [68] measure the speed of propagation of the calcium signal in the engineered ventricle using the calcium propagation imaging technique. Mean calcium wavefront propagation velocity from apex to base was 5.2 cm/s for hiPSC-CMs ventricles. Coherently, we compute the simulated speed of propagation analyzing the calcium concentration in two points of the *in-silico* tissue aligned in the direction of the wave propagation. The average speed is given by the ratio of the distance and the time taken by the signal to cover that distance. Furthermore, we define the interval as the time elapsed in between the calcium concentration reaches the maximum in the two points in a spontaneous action potential. Indeed, as in the Paci2018 cellular model the cells beat spontaneously, we apply a single stimulus to trigger a propagating action potential and then the tissue autonomously keeps the activity accordingly to its natural frequency.

We perform the analysis on an elongated parallelepiped with the fibers oriented accordingly to one of the principal directions and we measure the calcium concentration in two points 1cm apart in the internal part of the body. By setting appropriate boundary conditions and stimulation protocol that triggers a planar wave, the simulation results are governed by the

diffusion coefficient σ_i in the elongated direction

$$\sigma_i = \frac{\lambda}{\chi C_m (\lambda + 1)} \mathrm{d}_i \quad \left[\frac{\mathrm{m}^2}{\mathrm{s}} \right].$$
(6.32)

In the previous equation d_i is the eigenvalue of the matrix $\mathbf{D}$ in the direction i, that, depending on how we orient the fibers, represents either the longitudinal fiber direction or the orthogonal one.

Fixed the diffusion coefficient, we compute the speed of propagation of the calcium signal: the research is an iterative process and we automatize it by means of the bisection method. Indeed, we look for the diffusion coefficient that make vanish the difference between the simulated and the measured velocity.

For the hiPSC-CMs tissue we investigate values for the conductivity coefficient ranging approximately from 0.005 to 0.03 [mm^2/ms], as shown in Figure 6.4. The adopted simulation protocol reproduces the experimental procedure considering a simulation time ten times greater than experimental duration to obtain average properties.
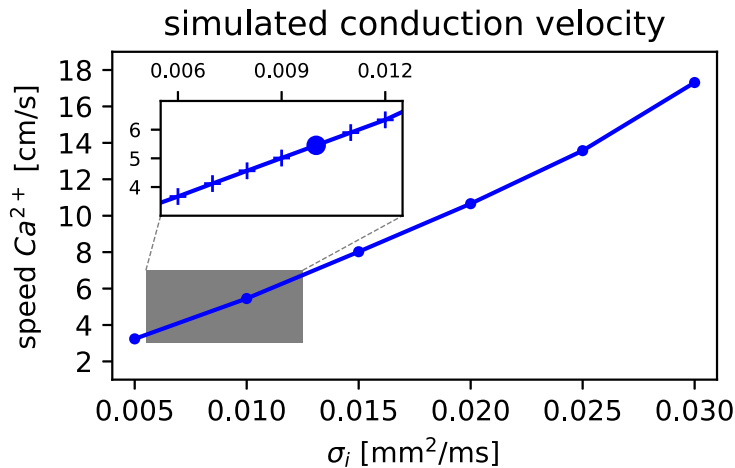

Figure 6.4: Simulated speed of propagation of the calcium signal for different values of the diffusivity coefficient. A more refined investigation was conducted for the velocity value reported in [68], as shown in the zoom.

For the set of parameters investigated, the conduction velocity depends almost linearly on the diffusion coefficient reflecting the linear-diffusion assumption, although the overall monodomain formulation is non-linear. Consequently, we interpolate the simulation results to set the coefficient for the analysis.

6.3.3   Comparison between finite element method and isogeometric analysis

In order to perform the simulation on the prescribed geometry using the best isogeometric set of parameters, we investigated the dependence of the framework accuracy on the conduction velocity. Thus, we analyzed the convergence under $h-$refinement, where h is the mesh element

size, considering $\sigma_i = 0.01, 0.1, 1.0 \quad [mm^2/ms]$.

First af all we considered a reduced slab geometry for a fiber, built as a parallelepiped of length $L = 3.2$ mm, width 0.25 mm, thickness 0.25 mm. In this geometry, we fixed a point on the fiber automatically located at $\boldsymbol{x}^\star = \{x_1, x_2, x_3\}$ such that $x_1 = 2.7933 mm$.

On this slab the relative error is calculated considering $T_{end} = 1.250 s$ and it is defined as

$$err = \frac{\int_0^{T_{end}} \left| V(\boldsymbol{x}^\star, t) - V^{ref}(\boldsymbol{x}^\star, t) \right|^2 dt}{\int_0^{T_{end}} \left| V^{ref}(\boldsymbol{x}^\star, t) \right|^2 dt} \tag{6.33}$$

where V^{ref} is the reference solution obtained considering $h = 0.005 mm$. Indeed, the generic V is the resulting solution for $h = 0.16, 0.08, 0.04, 0.02, 0.01$.

Univariate B-splice of orders $p = 1, 2, 3$ and continuity $c = p - 1$ are taken into account and results are presented in Figure 6.5, where the number of control points is
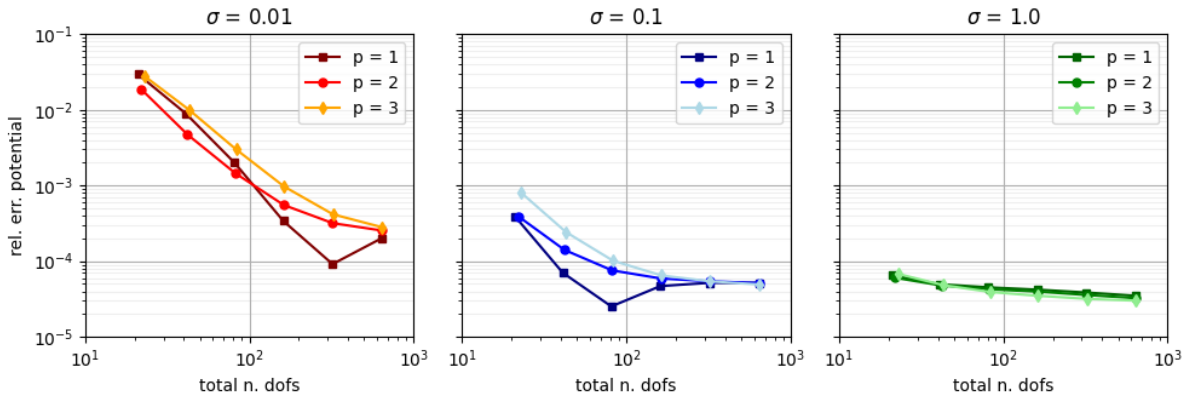
$$ncp = \frac{L}{h} + p.$$

Figure 6.5: Action potential relative errors considering three different conduction velocities and three different polynomial degrees.

The global error decreases for higher valuer of the conduction velocity, and for $\sigma = 1.0$ the higher degree $p = 3$ seems to be the best choice. Indeed, considering reduced conduction velocity, the accuracy does not present any improvement considering different polynomial degrees.

Despite these considerations, the resulting conduction velocity value that should be used to model the experimental engineered ventricle is $\sigma = 0.01$, see Figure 6.4. Focusing on this value, the generic solution can be split into two different contributions. The first term is closely related to the reaction term of the PDE and can be represented by the relative error of the wave shapes in $\boldsymbol{x}^\star$. Considered waves are both the action potential and each ionic concentrations, namely

$$err_V = \frac{\int_0^{T_{end}} \left(V(\boldsymbol{x}^\star, t) - V^{ref}(\boldsymbol{x}^\star, t) \right)^2 dt}{\int_0^{T_{end}} \left| V^{ref}(\boldsymbol{x}^\star, t) \right|^2 dt}$$
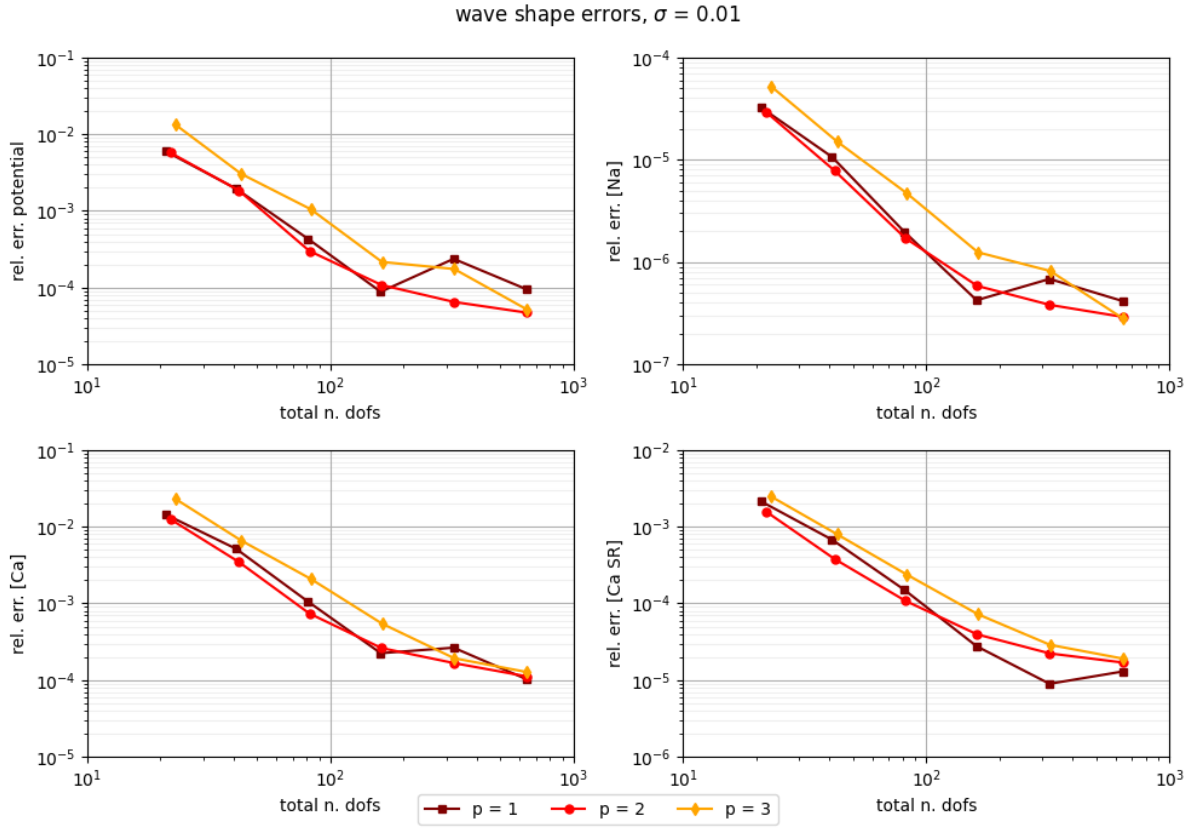
Figure 6.6:   Reaction relative errors resulting from the wave shapes of action potential, Sodium and Intercellular Calcium concentrations; $p = 1$ e $p = 2$ have the same accuracy on reaction.

$$err_{[Na^+]} = \frac{\int_0^{T_{end}} \left([Na^+](\boldsymbol{x}^\star, t) - [Na^+]^{ref}(\boldsymbol{x}^\star, t) \right)^2 dt}{\int_0^{T_{end}} |[Na^+]^{ref}(\boldsymbol{x}^\star, t)|^2 dt}$$

$$err_{[Ca^{2+}]_i} = \frac{\int_0^{T_{end}} \left([Ca^{2+}]_i(\boldsymbol{x}^\star, t) - [Ca^{2+}]_i^{ref}(\boldsymbol{x}^\star, t) \right)^2 dt}{\int_0^{T_{end}} \left| [Ca^{2+}]_i^{ref}(\boldsymbol{x}^\star, t) \right|^2 dt}$$

$$err_{[Ca^{2+}]_{SR}} = \frac{\int_0^{T_{end}} \left([Ca^{2+}]_{SR}(\boldsymbol{x}^\star, t) - [Ca^{2+}]_{SR}^{ref}(\boldsymbol{x}^\star, t) \right)^2 dt}{\int_0^{T_{end}} \left| [Ca^{2+}]_{SR}^{ref}(\boldsymbol{x}^\star, t) \right|^2 dt}$$

Such errors are summarized in Figure 6.6 and we can state that $p = 1$ e $p = 2$ have the same accuracy on reaction.

The second contribution deals with the diffusion problem. Thus, we analysed the relative error of the wave arrival time, this one defined as the time that maximizes the first derivative. Thus, given the time $\bar{t}$ as the arrival at the point $x^\star$, we define the signed relative error as:

$$err_{rel} = \frac{\bar{t} - \bar{t}^\star}{\bar{t}^\star}, \tag{6.34}$$

where $\bar{t}^\star$ is the arrival time of the reference solution.

Results in Figure 6.7 suggests that considering $p = 1$ the action potential wave arrives earlier
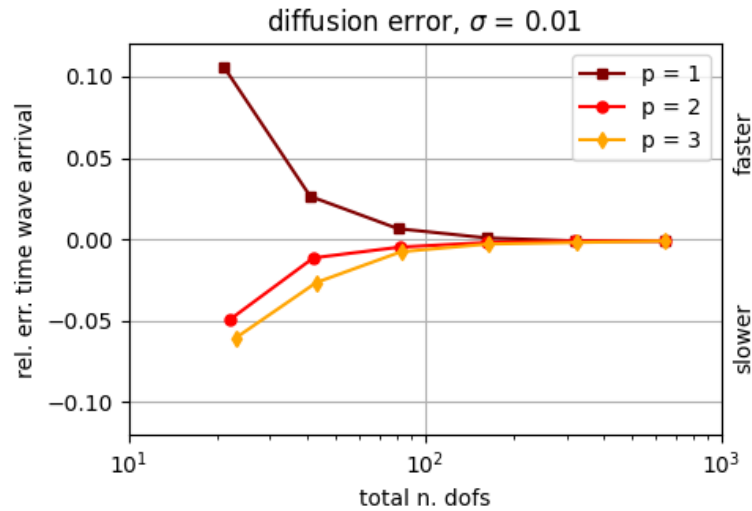
Figure 6.7: Diffusion relative error considering the time wave arrival; $p = 2$ increases accuracy of the diffusion term.

than the reference solution, while for higher values of the polynomial degree, the front of the wave is slower than the reference one.

Considering the absolute value of the error, $p = 2$ realizes the minimum and it is the best choice, able to increase the accuracy of the diffusion term of the system.

6.4 Work in progress and future advances

In the previous sections we have defined the computational framework to mimic the electrophysiological activity of the engineered ventricle. The last step is to carry out the final simulation on the whole geometry.

The simulation was performed considering an external stimulus equal to 20 pA spatially distributed as a sinus function in the squared application box, centred in (0, 4.5, 2). Initial conditions set the membrane to the repolarized potential $V = -74.9mV$, in the refractory phase, and the stimulus was applied for 100 milliseconds, allowing the plane wave electrical propagation before the spontaneous firing activity of every cell. As reported in Figure 6.8, only one external stimulus was applied and the wave front could span the whole geometry in less then one second; then cells in the stimulus box reached the threshold valued and autonomously depolarized restoring the spontaneous activity only for this group of cells. The new action potential wave propagate in the whole ventricle, showing a similar activity as alluded in the last snapshot of Figure 6.8.

The simulation reveals a continuous excitation propagation on the ventricle surface, confirming electrical continuity throughout the ventricle constructs.

The same description can be applied to the Intercellular Calcium dynamic. Next steps properly deal with the spontaneous calcium activity experimentally measured as a surrogate of the action potential. A first comparison could be taken considering a healthy heart, that was
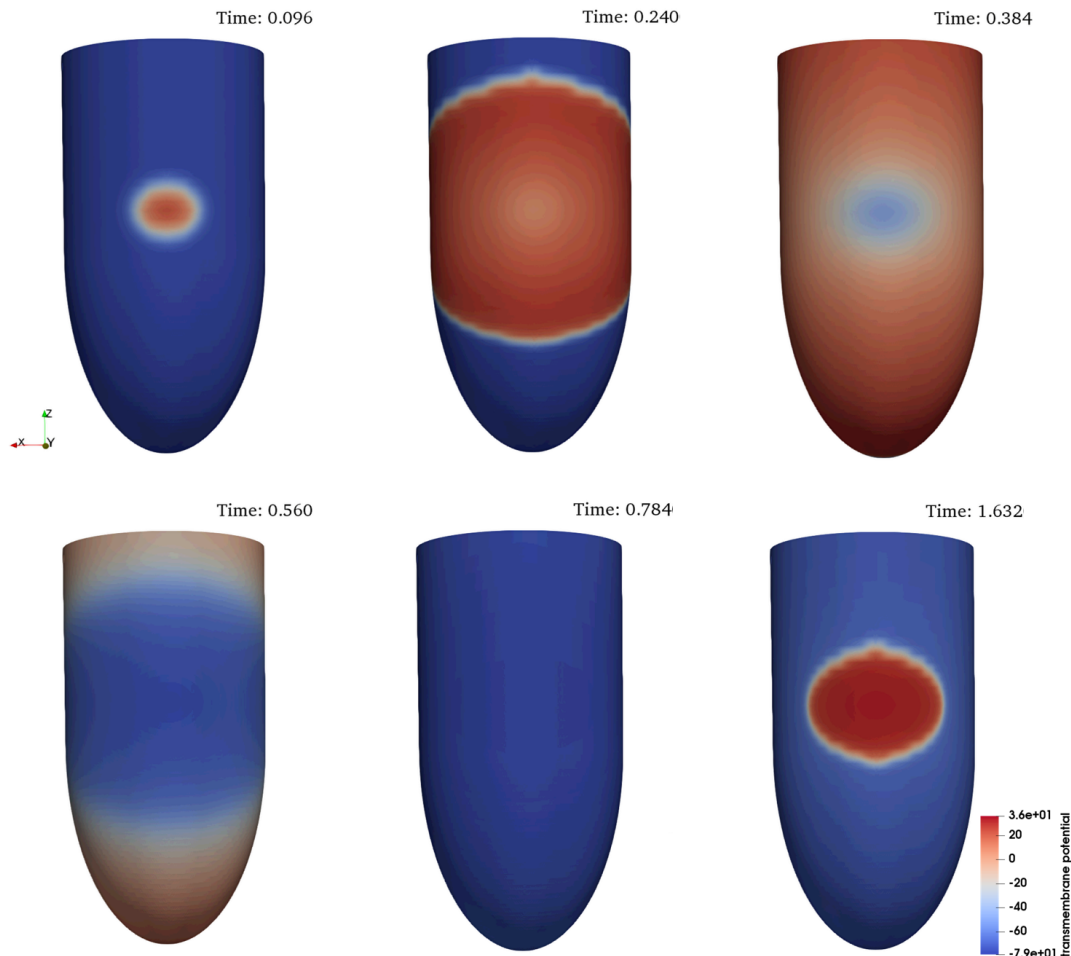
Figure 6.8: Final simulation snapshots, obtained performing the isogeometric implementation of the electrophysiological problem. The result is a continuous excitation propagation on the ventricle surface of the applied stimulus.

experimentally stressed to obtain some initial validation responses to gross alteration in the composition of the extracellular bath solution. For example, an expected reduction in beat rate was observed when decreasing the temperature from physiological 37°C to less than 30°C.

Furthermore, our future efforts will aim to model a hole in the virtual geometry, in order to reproduce the injury inflicted under geometrical control. Once again results can be compared to measured calcium activity, both considering a single-hole injury or a hole pair one, these latter generating spiral waves.

Finally, mechanical properties can be simulated and a new framework for electromechanical simulations can be built in order to complete the virtual modeling of the engineered ventricle replication. *In-vitro* experiments also measured tissue coverage and alignment and pressure–volume loops in the presence or absence of test compounds using catheter-based PV measuring systems. Such quantities are the results of simulations in the novel mechanical setup, and results can be compared.

Conclusions

The development of mathematical models is a huge field that developed in the last decade in different areas. In this thesis we presented some studies dealing with some specialized topics, in particular we have been focusing on the mathematical modeling and numerical simulation, applied to the cardiac electrophysiology analysis at a single cell level, dealing both with adult cardiomycytes and human induced pluripotent stem cells.

Indeed, after a presentation of some milestone models, we presented our contributions. First of all, we implemented two ionic models for human adult ventricular cardiomyocytes, namely the first generation model of Hodgkin-Huxley and the second generation model of O'Hara-Rudy. Such models were implemented in a C++ code and embedded in the $Life^X$ library.

My research activity has been focusing on the mathematical modeling and numerical simulation, applied to the cardiac electrophysiology analysis at a single cell level and on the Dynamic clamp technique application with the aim of gaining a clearer insight into the origin of the dynamics of electrophysiological models.

As a second contribution we presented the virtual dynamic clamp with the aim of gaining clearer insights into the phenotype detection when considering human induced pluripotent stem cells-derived cardiomyocytes. Our result can assert that dynamic clamp is a promising approach as it allows to unveil the chamber phenotype when considering a suitable injected I_{K1} current. Furthermore a virtual mathematical approach is suitable to provide new insides into the hiPSC-CMs AP reaction to the current injection.

Finally, a novel atrial specific computational model for AL hiPSC-CMs was also developed, in order to fill the gap and perform the behaviour of some specific currents, such as the *Ultrarapid Delayed Rectifier Current* and the *Small Conductance Calcium Activated Potassium Channel.*

A further contribution in the field of 3D modeling has also been described presenting a new tool to model an engineered ventricle. A innovative framework was created to this aim, integrating the well-established Monodomain formulation with the innovative isogeometric approach for the spatial discretization and mesh generation.

In the next months, the idea is to improve the described techniques, starting from the scheduled parameter optimization of the AL hiSPC-CM model if considering the single cell level. As described in the last chapter also we are also managing to investigate the Calcium dynamic when considering a three-dimensional description of the engineered ventricle. In the experimental validation perspective, a single hole or a hole-pair will be modeled in order to virtually replicate the spiral wave generation.

In the future, we are also going to explore different fields of the cardiac modeling area. Mechanical properties of hiPSC-CMs can be investigated in a double prospect. First, considering existing electromechanical tools for the whole ventricle can be used to complete the virtual modeling of the engineered ventricle replication. Second, creating a framework to analyze the mechanical activity of a single cell.

The other topic we are interested in is the one of personalized medicine, and developing specific models we could provide new insights into the cardiac AP mechanisms in physiological and pathological conditions. For example, different cardiac pathologies could be modeled for hiPSC-CMs merging one of the existing Paci generation model with the relative set of equations existing in literature to describe a specific disease.

A powerful potentiality of hiPSCs we also would like to exploit is that cell lines arising from the patient themselves have the same gene expression of the specific disease we want to treat. Thus, collaborating with different hospital is could be possible to develop patient-specific models, in order to test drugs with limited costs, leading to a faster and cheaper patient-specific therapy.

Finally, in term of regenerative medicine, we would like to merge the single cell model for hiPSC-CMs in the existing libraries and frameworks of the whole heart (both atria and ventricles), modeling the transplantation of hiPSC-CMs tissue into an ischemic region. Different responses could be expected: the transplanted tissue could work as a pacemaker center thank to the spontaneous activity of hiPSC-CMs, or these cells could propagate the original impulse also in these injured tissue, preventing the formation of spiral waves.

The answers to such questions are still unknown, and only research could help.

Bibliography

[1]   P. AFRICA. *Lifex: a flexible, high performance library for the numerical solution of complex finite element problems.* July 2022.

[2]   C. ALTOMARE, C. BARTOLUCCI, L. SALA, et al. «A dynamic clamping approach using *in silico* IK1 current for discrimination of chamber-specific hiPSC-derived cardiomyocytes». (2022). Manuscript submitted for publication.

[3]   C. ANTZELEVITCH. «M Cells in the Human Heart». *Circulation Research* 106.5 (2010), pp. 815–817.

[4]   H. J. AREVALO, K-JAEGER, and S. WALL. «Investigating the pro- and anti- arrhythmic properties of human induced pluripotent stem cell-derived cardiomyocytes in post-infarction patient hearts: a modeling study». *International conference on computational and mathematical Biomedical Engeneering* (2019).

[5]   F. AURICCHIO et al. «Innovative and efficient stent flexibility simulations based on isogeometric analysis». *Computer Methods in Applied Mechanics and Engineering* 295 (2015), pp. 347–361. ISSN: 0045-7825.

[6]   B. BAILLARGEON et al. «The Living Heart Project: A robust and integrative simulator for human heart function». *European Journal of Mechanics - A/Solids* 48 (2014). Frontiers in Finite-Deformation Electromechanics, pp. 38–47. ISSN: 0997-7538.

[7]   A. BARONE, F. FENTON, and A. VENEZIANI. «Numerical sensitivity analysis of a variational data assimilation procedure for cardiac conductivities». *Chaos: An Interdisciplinary Journal of Nonlinear Science* 27.9 (2017), p. 093930.

[8]   A. BARONE et al. «Efficient estimation of cardiac conductivities: A proper generalized decomposition approach». *Journal of Computational Physics* 423 (2020), p. 109810. ISSN: 0021-9991.

[9]   A. BARONE et al. «Experimental validation of a variational data assimilation procedure for estimating space-dependent cardiac conductivities». *Computer Methods in Applied Mechanics and Engineering* 358 (2020), p. 112615. ISSN: 0045-7825.

[10] V. BARONE et al. «Organization of junctional sarcoplasmic reticulum proteins in skeletal muscle fibers». *Journal of Muscle Research and Cell Motility* 36.6 (2015), pp. 501–515.

[11] C. Bartolucci, M. Forouzandehmehr, S. Severi, et al. «A Novel In Silico Electrome-
      chanical Model of Human Ventricular Cardiomyocyte». *Frontiers in Physiology* 13 (2022).
      ISSN: 1664-042X.

[12] F. B. Bedada, M. Wheelwright, and J. M. Metzger. «Maturation status of sarcomere
      structure and function in human iPSC-derived cardiac myocytes». *Biochimica et Biophysica
      Acta (BBA) - Molecular Cell Research* 1863.7 (2016), pp. 1829–1838.

[13] W. Beeler and H. Reuter. «Reconstruction of the action potential of ventricular
      myocardial fibres». *The Journal of physiology* 268.1 (1977), pp. 177–210.

[14] G. C.L. Bett et al. «Electronic "expression" of the inward rectifier in cardiocytes derived
      from human-induced pluripotent stem cells». *Heart Rhythm* 10.12 (2013), pp. 1903–1910.

[15] S. Botti, C. Bartolucci, C. Altomare, et al. «Numerical Simulations Indicate IK1
      Dynamic Clamp Can Unveil the Phenotype of Cardiomyocytes Derived from Induced
      Pluripotent Stem Cells». *2022 Computing in Cardiology*. in press. 2022.

[16] S. Bouchard, V. Jacquemet, and A. Vinet. «Automaticity in acute ischemia: Bifurca-
      tion analysis of a human ventricular model». *Physical Review E* 83.1 (2011).

[17] P. W. Burridge and E. T. Zambidis. «Highly Efficient Directed Differentiation of Human
      Induced Pluripotent Stem Cells into Cardiomyocytes». (2013), pp. 149–161.

[18] L. A. Charawi. «Isogeometric overlapping Schwarz preconditioners for the Bidomain
      reaction–diffusion system». *Computer Methods in Applied Mechanics and Engineering* 319
      (2017), pp. 472–490.

[19] P. Colli Franzone, L. F. Pavarino, and S. Scacchi. *Mathematical cardiac electro-
      physiology*. Vol. 13. Springer, 2014. ISBN: 978-3-319-04801-7.

[20] F. Conti and A. Battaglia-Mayer. «Fisiologia medica». Italian. Milano: Edi-Ermes,
      2010. Chap. 44, pp. 103–163.

[21] J. A. Cottrell, T. J.R. Hughes, and Y. Bazilevs. *Isogeometric analysis: toward
      integration of CAD and FEA*. John Wiley & Sons, 2009.

[22] M. Courtemanche, R. J. Ramirez, and S. Nattel. «Ionic mechanisms underlying
      human atrial action potential properties: insights from a mathematical model». *American
      Journal of Physiology-Heart and Circulatory Physiology* 275.1 (1998), H301–H321.

[23] E. D'Angelo, A. Peres, and A. Angioy. *Fisiologia: molecole, cellule e sistemi*. Italian.
      Milano: EdiErmes, 2006.

[24] H. D. Devalla et al. «Atrial-like cardiomyocytes from human pluripotent stem cells are
      a robust preclinical model for assessing atrial-selective pharmacology». *EMBO Mol Med.*
      7.4 (2015), pp. 394–410.

[25] S. Doi, J. Inoue, and Z. Pan. *Computational Electrophysiology*. Springer Japan, 2010.

[26] A. Eder et al. «Human engineered heart tissue as a model system for drug testing».
      Advanced Drug Delivery Reviews 96 (2016). Tissue engineering of the heart: from in vitro
      models to regenerative solutions, pp. 214–224. ISSN: 0169-409X.

[27] A. Fabbri et al. «Computational analysis of the human sinus node action potential: model development and effects of mutations». *The Journal of Physiology* 595.7 (2017), pp. 2365–2396.

[28] A. Fabiato. «Calcium-induced release of calcium from the cardiac sarcoplasmic reticulum». *American Journal of Physiology-Cell Physiology* 245.1 (1983), pp. C1–C14.

[29] F. H. Fenton et al. «Modeling wave propagation in realistic heart geometries using the phase-field method». *Chaos: An Interdisciplinary Journal of Nonlinear Science* 15.1 (2005), p. 013502.

[30] M. Fink et al. «Contributions of HERG K+ current to repolarization of the human ventricular action potential». *Prog. Biophys. Mol. Biol.* 96.1 (2008), pp. 357–376.

[31] C. Geuzaine and J.F. Remacle. «Gmsh: A 3-D finite element mesh generator with built-in pre-and post-processing facilities». *International journal for numerical methods in engineering* 79.11 (2009), pp. 1309–1331.

[32] I. Goldfracht et al. «Engineered heart tissue models from hiPSC-derived cardiomyocytes and cardiac ECM for disease modeling and drug testing applications». *Acta Biomaterialia* 92 (2019), pp. 145–159. issn: 1742-7061.

[33] E. Grandi, F. S. Pasqualini, and D. M. Bers. «A novel computational model of the human ventricular action potential and Ca transient». *J. Molec. Cell. Cardiol.* 48.1 (2010), pp. 112–121.

[34] M. Grunnet. «Repolarization of the cardiac action potential. Does an increase in repolarization capacity constitute a new anti-arrhythmic principle?». *Acta Physiologica* 198 (2010), pp. 1–48.

[35] B. Hille. *Ionic Channels of Excitable Membranes.* Sinauer Associates Inc, 1992. isbn: 0-87893-323-9.

[36] A. L. Hodgkin and A. F. Huxley. «A quantitative description of membrane current and its application to conduction and excitation in nerve». eng. *The Journal of physiology* 117.4 (Aug. 1952), pp. 500–544. issn: 1469-7793.

[37] T. JR Hughes. *The finite element method: linear static and dynamic finite element analysis.* Courier Corporation, 2012.

[38] T. JR Hughes, J. A. Cottrell, and Y. Bazilevs. «Isogeometric analysis: CAD, finite elements, NURBS, exact geometry and mesh refinement». *Computer methods in applied mechanics and engineering* 194.39-41 (2005), pp. 4135–4195.

[39] T.J.R. Hughes, A. Reali, and G. Sangalli. «Efficient quadrature for NURBS-based isogeometric analysis». *Computer Methods in Applied Mechanics and Engineering* 199.5 (2010). Computational Geometry and Analysis, pp. 301–313. issn: 0045-7825.

[40] T. Kamakura et al. «Ultrastructural Maturation of Human-Induced Pluripotent Stem Cell-Derived Cardiomyocytes in a Long-Term Culture». *Circulation Journal* 77.5 (2013), pp. 1307–1314.

[41]   A. M. KATZ. *Physiology of the Heart*. Lippincott Williams & Wilkins, 2010.

[42]   J. KEENER and J. SNEYD, eds. *Mathematical Physiology*. Springer New York, 2009.

[43]   J. P. KEENER and J. SNEYD. *Mathematical physiology*. Vol. 1. Springer, 1998.

[44]   J. KEIZER and L. LEVINE. «Ryanodine receptor adaptation and Ca2+ Induced Ca2+ release- dependent Ca2+ oscillations». (1996).

[45]   D. C. KERNIK et al. «A computational model of induced pluripotent stem-cell derived cardiomyocytes incorporating experimental variability from multiple data sources». *The Journal of Physiology* 597.17 (2019), pp. 4533–4564.

[46]   J. KIENDL. «Isogeometric analysis and shape optimal design of shell structures». PhD thesis. Technische Universität München, 2011.

[47]   J. T. KOIVUMÄKI, T. KORHONEN, and P. TAVI. «Impact of Sarcoplasmic Reticulum Calcium Release on Calcium Dynamics and Action Potential Morphology in Human Atrial Myocytes: A Computational Study». *PLOS Comp. Biol.* 7 (Jan. 2011), pp. 1–14.

[48]   J. T. KOIVUMÄKI, T. KORHONEN, and P. TAVI. «Impact of Sarcoplasmic Reticulum Calcium Release on Calcium Dynamics and Action Potential Morphology in Human Atrial Myocytes: A Computational Study». *PLoS Computational Biology* 7.1 (2011). Ed. by Andrew D. MCCULLOCH, e1001067.

[49]   J. T. KOIVUMÄKI et al. «In Silico Screening of the Key Cellular Remodeling Targets in Chronic Atrial Fibrillation». *PLOS Computational Biology* 10.5 (May 2014), pp. 1–15.

[50]   J. T. KOIVUMÄKI et al. «Structural Immaturity of Human iPSC-Derived Cardiomyocytes: In Silico Investigation of Effects on Function and Disease Modeling». *Frontiers in Physiology* 9 (2018). ISSN: 1664-042X.

[51]   T. KORHONEN et al. «Local Ca2+ releases enable rapid heart rates in developing cardiomyocytes». *The Journal of Physiology* 588.9 (), pp. 1407–1417.

[52]   S. KOUMI, C. L. BACKER, and C. E. ARENTZEN. «Characterization of Inwardly Rectifying K+ Channel in Human Cardiac Myocytes». *Circulation* 92.2 (1995), pp. 164–174.

[53]   S. KRISHNAMOORTHI, M. SARKAR, and W. S. KLUG. «Numerical quadrature and operator splitting in finite element methods for cardiac electrophysiology». *International journal for numerical methods in biomedical engineering* 29.11 (2013), pp. 1243–1266.

[54]   Y. KURATA et al. «Dynamical Mechanisms of Pacemaker Generation in IK1-Downregulated Human Ventricular Myocytes: Insights from Bifurcation Analyses of a Mathematical Model». *Biophysical Journal* 89.4 (2005), pp. 2865–2887.

[55]   M. LEMME et al. «Atrial-like Engineered Heart Tissue: An In Vitro Model of the Human Atrium». *Stem Cell Reports* 11.6 (2018), pp. 1378–1390. ISSN: 2213-6711.

[56]   R. A. LI et al. «Bioengineering an electro-mechanically functional miniature ventricular heart chamber from human pluripotent stem cells». *Biomaterials* 163 (2018), pp. 116–127. ISSN: 0142-9612.

[57] P. LIANG et al. «Drug Screening Using a Library of Human Induced Pluripotent Stem Cell-Derived Cardiomyocytes Reveals Disease-Specific Patterns of Cardiotoxicity». *Circulation* 127 (Mar. 2013).

[58] J. U. LIND et al. «Instrumented cardiac microphysiological devices via multimaterial three-dimensional printing». *Nature materials* 16.3 (2017), pp. 303–308.

[59] A. M. LODRINI et al. «Human Induced Pluripotent Stem Cells Derived from a Cardiac Somatic Source: Insights for an In-Vitro Cardiomyocyte Platform». *International Journal of Molecular Sciences* 21.2 (2020). ISSN: 1422-0067.

[60] A. LOPEZ-PEREZ et al. «Personalized cardiac computational models: from clinical data to simulation of infarct-related ventricular tachycardia». *Frontiers in physiology* 10 (2019), p. 580.

[61] G. LORENZO, M. A. SCOTT, K. TEW, et al. «Tissue-scale, personalized modeling and simulation of prostate cancer growth». *Proceedings of the National Academy of Sciences* 113.48 (2016), E7663–E7671. ISSN: 0027-8424.

[62] S. D. LUNDY et al. «Structural and Functional Maturation of Cardiomyocytes Derived from Human Pluripotent Stem Cells». *Stem Cells and Development* 22.14 (2013), pp. 1991–2002.

[63] C. H. LUO and Y. RUDY. «A dynamic model of the cardiac ventricular action potential. I. Simulations of ionic currents and concentration changes.». *Circulation Research* 74.6 (1994), pp. 1071–1096.

[64] C. H. LUO and Y. RUDY. «A dynamic model of the cardiac ventricular action potential. II. Afterdepolarizations, triggered activity, and potentiation.». *Circulation Research* 74.6 (1994), pp. 1097–1113.

[65] C. H. LUO and Y. RUDY. «A model of the ventricular cardiac action potential. Depolarization, repolarization, and their interaction.». *Circulation Research* 68.6 (1991), pp. 1501–1526.

[66] Y. MA et al. «High purity human-induced pluripotent stem cell-derived cardiomyocytes: electrophysiological properties of action potentials and ionic currents». *American Journal of Physiology-Heart and Circulatory Physiology* 301.5 (2011), H2006–H2017.

[67] L. MACQUEEN et al. «Addendum: A tissue-engineered scale model of the heart ventricle». *Nature Biomedical Engineering* (Mar. 2022), pp. 1–1.

[68] L. A MACQUEEN et al. «A tissue-engineered scale model of the heart ventricle». *Nature biomedical engineering* 2.12 (2018), pp. 930–941.

[69] N. MAHERALI et al. «Directly Reprogrammed Fibroblasts Show Global Epigenetic Remodeling and Widespread Tissue Contribution». *Cell Stem Cell* 1.1 (2007), pp. 55–70.

[70] R. S. MAHLA. «Stem Cells Applications in Regenerative Medicine and Disease Therapeutics». *International Journal of Cell Biology* 2016 (2016), pp. 1–24.

[71] M. M. MALECKAR et al. «K+ current changes account for the rate dependence of the action potential in the human atrial myocyte». *American Journal of Physiology-Heart and Circulatory Physiology* 297.4 (2009), H1398–H1410.

[72] J. MALMIVUO and R. PLONSEY. *Bioelectromagnetism: Principles and Applications of Bioelectric and Biomagnetic Fields.* Oxford University Press, 1995. ISBN: 978-0195058239.

[73] A. V. MALTSEV et al. «Functional Heterogeneity of Cell Populations Increases Robustness of Pacemaker Function in a Numerical Model of the Sinoatrial Node Tissue». *Frontiers in Physiology* 13 (2022). ISSN: 1664-042X.

[74] S. MORGANTI et al. «Patient-specific isogeometric structural analysis of aortic valve closure». *Computer methods in applied mechanics and engineering* 284 (2015), pp. 508–520.

[75] A. NITTI et al. «A curvilinear isogeometric framework for the electromechanical activation of thin muscular tissues». *Computer Methods in Applied Mechanics and Engineering* 382 (2021), p. 113877. ISSN: 0045-7825.

[76] D. NOBLE. «Late sodium current in the pathophysiology of cardiovascular disease: consequences of sodium-calcium overload». *Heart* 92.suppl_4 (2006), pp. iv1–iv5.

[77] A. NYGREN et al. «Mathematical model of an adult human atrial cell: the role of K+ currents in repolarization.». *Circulation research* 82 1 (1998), pp. 63–81.

[78] D. OGDEN and P. STANFIELD. «Patch clamp techniques for single channel and whole-cell recording». (Jan. 1994).

[79] T. O'HARA et al. «Simulation of the Undiseased Human Cardiac Ventricular Action Potential: Model Formulation and Experimental Validation». *PLoS Computational Biology* 7.5 (2011). Ed. by Andrew D. MCCULLOCH, e1002061.

[80] T. O'HARA et al. «Simulation of the Undiseased Human Cardiac Ventricular Action Potential: Model Formulation and Experimental Validation». *PLoS Comput. Biol.* 7 (May 2011), e1002061.

[81] K. OKITA, T. ICHISAKA, and S. YAMANAKA. «Generation of germline-competent induced pluripotent stem cells». *Nature* 448.7151 (2007), pp. 313–317.

[82] M. PACI et al. «All-Optical Electrophysiology Refines Populations of In Silico Human iPSC-CMs for Drug Evaluation». *Biophysical Journal* 118.10 (2020), pp. 2596–2611. ISSN: 0006-3495.

[83] M. PACI et al. «Automatic Optimization of an in Silico Model of Human iPSC Derived Cardiomyocytes Recapitulating Calcium Handling Abnormalities». *Frontiers in Physiology* 9 (2018).

[84] M. PACI et al. «Comparison of the Simulated Response of Three in Silico Human Stem Cell-Derived Cardiomyocytes Models and in Vitro Data Under 15 Drug Actions». *Frontiers in Pharmacology* 12 (2021). ISSN: 1663-9812.

[85] M. Paci et al. «Computational Models of Ventricular- and Atrial-Like Human Induced Pluripotent Stem Cell Derived Cardiomyocytes». *Annals of biomedical engineering* 41 (May 2013).

[86] M. Paci et al. «Human induced pluripotent stem cell-derived versus adult cardiomyocytes: an in silico electrophysiological study on ionic current block effects». English. *British Journal of Pharmacology* (2015), pp. 5147 –5160. issn: 0007-1188.

[87] M. Paci et al. «Mathematical modelling of the action potential of human embryonic stem cell derived cardiomyocytes». *BioMedical Engineering OnLine* 11.1 (2012), p. 61.

[88] M. Paci et al. «Phenotypic variability in LQT3 human induced pluripotent stem cell-derived cardiomyocytes and their response to antiarrhythmic pharmacologic therapy: An in silico approach». *Heart Rhythm* 14.11 (2017), pp. 1704–1712.

[89] I. Park et al. «Generation of human-induced pluripotent stem cells». *Nature Protocols* 3.7 (2008), pp. 1180–1186.

[90] Y. A. Patel et al. «Hard real-time closed-loop electrophysiology with the Real-Time eXperiment Interface (RTXI)». *PLOS Computational Biology* 13.5 (May 2017), pp. 1–22.

[91] A. S. Patelli et al. «Isogeometric approximation of cardiac electrophysiology models on surfaces: An accuracy study with application to the human left atrium». *Computer Methods in Applied Mechanics and Engineering* 317 (2017), pp. 248–273. issn: 0045-7825.

[92] P. Pathmanathan et al. «The significant effect of the choice of ionic current integration method in cardiac electro-physiological simulations». *International Journal for Numerical Methods in Biomedical Engineering* 27.11 (2011), pp. 1751–1770.

[93] L. Pegolotti, L. Dedè, and A. Quarteroni. «Isogeometric Analysis of the electrophysiology in the human heart: Numerical simulation of the bidomain equations on the atria». *Computer Methods in Applied Mechanics and Engineering* 343 (2019), pp. 52–73.

[94] L. Piegl and W. Tiller. *The NURBS book*. Springer Science & Business Media, 1996.

[95] J. Pitt-Francis et al. «Chaste: a test-driven approach to software development for biological modelling». *Computer Physics Communications* 180.12 (2009), pp. 2452–2471.

[96] R. M. E. Meijer van Putten et al. «Ion channelopathies in human induced pluripotent stem cell derived cardiomyocytes: a dynamic clamp study with virtual IK1». *Frontiers in Physiol* 6 (2015). issn: 1664-042X.

[97] T. Quail, A. Shrier, and L. Glass. «Predicting the onset of period-doubling bifurcations in noisy cardiac systems». *Proceedings of the National Academy of Sciences* 112.30 (2015), pp. 9358–9363.

[98] A. Quarteroni. *Modellistica Numerica per Problemi Differenziali*. Springer Milan, 2012.

[99] A. Quarteroni and A. Valli. *Numerical Approximation of Partial Differential Equations*. Springer Berlin Heidelberg, 1994.

[100] C. ROBERTSON, . D. TRAN, and S. C. GEORGE. «Concise Review: Maturation Phases of Human Pluripotent Stem Cell-Derived Cardiomyocytes». *Stem Cells* 31.5 (Apr. 2013), pp. 829–837. ISSN: 1066-5099.

[101] H. P. C. ROBINSON. «Dynamic Clamp: Synthetic Conductances and Their Influence on Membrane Potential». (2013). Ed. by Gordon C. K. ROBERTS, pp. 527–533.

[102] C. RODERO et al. «Linking statistical shape models and simulated function in the healthy adult human heart». *PLoS computational biology* 17.4 (2021), e1008851.

[103] D. S. ROSENBAUM and C. CABO. *Quantitative Cardiac Electrophysiology.* Informa Healthcare, 2002. ISBN: 0-8247-0774-5.

[104] Y. RUDY. «Molecular Basis of Cardiac Action Potential Repolarization». *Annals of the New York Academy of Sciences* 1123.1 (2008), pp. 113–118.

[105] C. SACCHETTO, L. VITIELLO, L. J. DE WINDT, et al. «Modeling Cardiovascular Diseases with hiPSC-Derived Cardiomyocytes in 2D and 3D Cultures». *International Journal of Molecular Sciences* 21.9 (2020). ISSN: 1422-0067.

[106] F. B. SACHSE. *Computational cardiology.* eng. Frank B. Sachse., Includes bibliographical references (p. [299]-322). New York, 2004.

[107] L. F. SANTANA, E. P. CHENG, and W. J. LEDERER. «How does the shape of the cardiac action potential control calcium signaling and contraction in the heart?». *Journal of Molecular and Cellular Cardiology* 49.6 (2010), pp. 901–903.

[108] A. SANTIAGO et al. «Fully coupled fluid-electro-mechanical model of the human heart for supercomputers». *International journal for numerical methods in biomedical engineering* 34.12 (2018), e3140.

[109] L. SARTIANI et al. «Developmental Changes in Cardiomyocytes Differentiated from Human Embryonic Stem Cells: A Molecular and Electrophysiological Approach». *Stem Cells* 25.5 (Jan. 2007), pp. 1136–1144.

[110] D. SCHIPANSKI and N. KNOEPFFLER. *Humanbiotechnology as Social Challenge: An Interdisciplinary Introduction to Bioethics (Ashgate Studies in Applied Ethics).* Routledge, 2007. ISBN: 978-0-7546-5755-2.

[111] C. SCHMIDT, F. WIEDMANN, N. VOIGT, et al. «Upregulation of K(2P)3.1 K+ Current Causes Action Potential Shortening in Patients With Chronic Atrial Fibrillation». *Circulation* 132 (May 2015).

[112] S. W. SCOTT. *Stimulation simulations of young yet cultured beating hearts.* State University of New York at Buffalo, 1979.

[113] T. R. SHANNON et al. «A Mathematical Treatment of Integrated Ca Dynamics within the Ventricular Myocyte». *Biophysical Journal* 87.5 (2004), pp. 3351–3371.

[114] Y. SHI et al. «Induced pluripotent stem cell technology: a decade of progress». *Nature Reviews Drug Discovery* 16.2 (2016), pp. 115–130.

[115] H. T. Shih. «Anatomy of the action potential in the heart». *Texas Heart Institute journal* 21.1 (1994), pp. 30–41. ISSN: 0730-2347.

[116] D. C. Sigg et al., eds. *Cardiac Electrophysiology Methods and Models.* Springer US, 2010.

[117] L. Skibsbye et al. «Refractoriness in human atria: Time and voltage dependence of sodium channel availability». *Journal of Molecular and Cellular Cardiology* 101 (2016), pp. 26–34. ISSN: 0022-2828.

[118] J. Sneyd and J.F. Dufour. «A dynamic model of the type-2 inositol trisphosphate receptor». *Proceedings of the National Academy of Sciences* 99.4 (2002), pp. 2398–2403.

[119] M. Strocchi et al. «A publicly available virtual cohort of four-chamber heart meshes for cardiac electro-mechanics simulations». *PloS one* 15.6 (2020), e0235145.

[120] L. Studer, E. Vera, and D. Cornacchia. «Programming and Reprogramming Cellular Age in the Era of Induced Pluripotency». *Cell Stem Cell* 16.6 (2015), pp. 591–600.

[121] J. Sundnes et al. *Computing the electrical activity in the heart.* Vol. 1. Springer Science & Business Media, 2007. ISBN: 978-3-540-33437-8.

[122] K. Takahashi and S. Yamanaka. «Induction of Pluripotent Stem Cells from Mouse Embryonic and Adult Fibroblast Cultures by Defined Factors». *Cell* 126.4 (2006), pp. 663–676.

[123] K. Takahashi et al. «Induction of Pluripotent Stem Cells from Adult Human Fibroblasts by Defined Factors». *Cell* 131.5 (2007), pp. 861–872.

[124] K. Ten Tusscher et al. «A model of human ventricular tissue». *Americ. J. Physiol. HC Physiol.* 286 (May 2004), H1573–89.

[125] M. Tiburcy et al. «Defined Engineered Human Myocardium With Advanced Maturation for Applications in Heart Failure Modeling and Repair». *Circulation* 135.19 (2017), pp. 1832–1847.

[126] J. Tomek et al. «Development, calibration, and validation of a novel human ventricular myocyte model in health, disease, and drug block». *eLife* 8 (2019). ISSN: 2050-084X.

[127] M. Torre. «Advanced IsoGeometric methods for active tissue simulations (in preparation)». PhD thesis. University of Pavia, 2023.

[128] M. Torre et al. «An efficient isogeometric collocation approach to cardiac electrophysiology». *Computer Methods in Applied Mechanics and Engineering* 393 (Apr. 2022), p. 114782.

[129] K. Tsumoto et al. «Hysteretic Dynamics of Multi-Stable Early Afterdepolarisations with Repolarisation Reserve Attenuation: A Potential Dynamical Mechanism for Cardiac Arrhythmias». *Scientific Reports* 7.1 (2017).

[130] K. H. W. J. ten Tusscher and A. V. Panfilov. «Alternans and spiral breakup in a human ventricular tissue model». *American Journal of Physiology-Heart and Circulatory Physiology* 291.3 (2006), H1088–H1100.

[131] K. H. W. J. TEN TUSSCHER et al. «A model for human ventricular tissue». *American Journal of Physiology-Heart and Circulatory Physiology* 286.4 (2004), H1573–H1589.

[132] E. TZATZALOS et al. «Engineered heart tissues and induced pluripotent stem cells: Macro- and microstructures for disease modeling, drug screening, and translational studies». *Advanced Drug Delivery Reviews* 96 (2016). Tissue engineering of the heart: from in vitro models to regenerative solutions, pp. 234–244. ISSN: 0169-409X.

[133] M. VAGOS et al. «Computational Modeling of Electrophysiology and Pharmacotherapy of Atrial Fibrillation: Recent Advances and Future Challenges». *Frontiers in Physiology* 9 (2018). ISSN: 1664-042X.

[134] A. L. VEGA et al. «Dynamic Changes in Sarcoplasmic Reticulum Structure in Ventricular Myocytes». *Journal of Biomedicine and Biotechnology* 2011 (2011), pp. 1–14.

[135] A. O. VERKERK et al. «Patch-Clamp Recording from Human Induced Pluripotent Stem Cell-Derived Cardiomyocytes: Improving Action Potential Characteristics through Dynamic Clamp». *Journal of Molec. Sc.* 18.9 (2017). ISSN: 1422-0067.

[136] M. WERNIG et al. «In vitro reprogramming of fibroblasts into a pluripotent ES-cell-like state». *Nature* 448.7151 (2007), pp. 318–324.

[137] R. WILDERS. «Dynamic clamp: a powerful tool in cardiac electrophysiology». *The Journal of Physiology* 576.2 (2006), pp. 349–359.

[138] M. WILHELMS et al. «Benchmarking electrophysiological models of human atrial myocytes». *Frontiers in Physiology* 3 (2013). ISSN: 1664-042X.

[139] H. YANG and A. VENEZIANI. «Efficient estimation of cardiac conductivities via POD-DEIM model order reduction». *Applied Numerical Mathematics* 115 (2017), pp. 180–199. ISSN: 0168-9274.

[140] X. YANG, L. PABON, and C. E. MURRY. «Engineering Adolescence». *Circulation Research* 114.3 (2014), pp. 511–523.

[141] R. J. YOUNG and A. V. PANFILOV. «Anisotropy of wave propagation in the heart can be modeled by a Riemannian electrophysiological metric». *Proceedings of the National Academy of Sciences* 107.34 (2010), pp. 15063–15068.

[142] X.-H. ZHANG et al. «Ca2+ signaling in human induced pluripotent stem cell-derived cardiomyocytes (iPS-CM) from normal and catecholaminergic polymorphic ventricular tachycardia (CPVT)-afflicted subjects». *Cell Calcium* 54.2 (2013), pp. 57–70. ISSN: 0143-4160.

[143] O. C ZIENKIEWICZ, R. L. TAYLOR, and J. Z. ZHU. *The finite element method: its basis and fundamentals.* Elsevier, 2005.

[144] L. ZWI et al. «Cardiomyocyte Differentiation of Human Induced Pluripotent Stem Cells». *Circulation* 120.15 (2009), pp. 1513–1523.